III-V semiconductor nanowire array avalanche photodiodes

by

Burak Tekcan

A thesis
presented to the University of Waterloo
in fulfillment of the
thesis requirement for the degree of
Doctor of Philosophy
in
Electrical and Computer Engineering

Waterloo, Ontario, Canada, 2022

© Burak Tekcan 2022

Examining Committee Membership

The following served on the Examining Committee for this thesis. The decision of the Examining Committee is by majority vote.

External Examiner:	Ray LaPierre Professor, Dept. of Engineering Physics McMaster University
Supervisors:	Michael E. Reimer Associate Professor, Dept. of Electrical and Computer Engineering University of Waterloo
	Dayan Ban Professor, Dept. of Electrical and Computer Engineering University of Waterloo
Internal Member:	Karim Karim Professor, Dept. of Electrical and Computer Engineering University of Waterloo
Internal Member:	Michal Bajcsy Associate Professor, Dept. of of Electrical and Computer Engineering University of Waterloo
Internal-External Member:	Jonathan Baugh Professor, Dept. of Chemistry University of Waterloo

Author's Declaration

This thesis consists of material all of which I authored or co-authored: see Statement of Contributions included in the thesis. This is a true copy of the thesis, including any required final revisions, as accepted by my examiners.

I understand that my thesis may be made electronically available to the public.

Statement of contributions

This thesis presents a body of work that includes contributions from several people. Dr. Lin Tian helped with building Ti:Sapphire external quantum efficiency setup, running the spectral responsivity measurements and preparation of the Attocube cryostat setup. Dr. Sasan Vosoogh-Grayli and Brad van Kasteren performed simulations for the optimization of InGaAs nanowire arrays using FDTD simulations. I have designed the stack layers of InGaAs p-i-n and InGaAs SACM avalanche diodes, simulated the electrical current and electric field profiles. I have developed and optimized the complete nanowire and device fabrication recipes. I characterized the fabricated devices with the external quantum efficiency setup I designed and built. Dr. Tarun Patel and Dr. Daozhi Shen helped running FTIR measurements by customizing the setup for spectral photocurrent and optical transmission and reflection measurements, respectively. Dr. Sasan Vosoogh-Grayli prepared the first draft of the manuscript published in Scientific Reports. I designed the photoluminenscence setup and Dr. Mohd Zeeshan helped me to build and measure InGaAs nanowire arrays samples. Dr. Francois Sfigakis has contributed several times with his valuable suggestions and directions for nanofabrication and troubleshooting for noise problem in the cryostat setup. Man Chun Tam performed the moleculer beam epitaxy thin film growth with guidance from Prof. Zbig Wasilewski. Dr. Jonathan Baugh, Dr. Adam Wei Tsen and Dr. Michal Bajcsy allowed me to use their labs and equipment. Dr. Michael Reimer supervised the whole project, offered insight and guidance at every decision making and scientific analysis step. Prof. Dayan Ban also supervised the project and offered scientific guidance throughout the project.

- Chapter 2 includes partial information and analysis from our publication:

  Gibson S.J., van Kasteren B., **Tekcan, B.**, Cui Y., van Dam D., Haverkort, J.E.M., Bakkers E.P.A.M, and Reimer M.E. (2019) Tapered InP nanowire arrays for efficient broadband high speed single-photon detection. *Nature Nanotechnology*, 14(5):473–479.

- Chapter 3 is adapted from our publication:

  Tekcan, B., van Kasteren, B., Grayli, S.V., Shen, D. Tam, M.C., Ban, D., Wasilewski, Z., Tsen, A.W., and Reimer, M.E. (2022). Semiconductor nanowire metamaterial for broadband near-unity absorption. *Scientific Reports*, 12, 9663.

Abstract

Detecting single photons with high efficiency and timing resolution opens up new possibilities for various technologies such as light detection and ranging (LIDAR), long-distance secure communication, singlet oxygen detection for dose monitoring in cancer treatment, optical coherence tomography (OCT) for eye imaging and quantum computing. For instance, the image quality for analysis of biological tissue or precision of LIDAR systems can be significantly improved with quantum sensing technologies. OCT imaging systems can be improved for higher resolution mapping of human retina leading to early detection of blinding diseases. Detecting single photons at a high bandwidth can also enable high speed quantum communication technologies by improving the detection speed.

Currently, the two leading technologies for single-photon detection are superconducting nanowires and semiconductor-based avalanche photodiodes. Superconducting nanowires have excellent detection efficiencies (>90%) and precise timing resolution (<50 ps); however, they require cryogenic temperatures, bulky compressors and pumps to operate (typically <4K), which results in a serious limitation for practical and portable applications. In contrast, semiconductor-based single-photon avalanche diode (SPAD) technology exists for portable applications, nonetheless, the high efficiency is achieved for a small wavelength range and at the cost of timing resolution (200-500 ps).

This work offers a novel approach to improve the quantum efficiency of semiconductor-based avalanche photodiodes by taking advantage of the remarkable optical and electrical properties of semiconductor nanowires. Embedding a photodiode architecture in nanowire arrays shows great promise for improving device performance, leading the way towards next generation quantum detectors. In this work, we designed a near-unity absorber from arrays of InGaAs nanowires with a truncated cone shape using finite-difference time-domain (FDTD) simulations. We optimized the nanowire taper angle and geometry of the array to achieve an average absorptance of 97% from 400 nm to 1650 nm. Next, we developed and optimized a nanofabrication recipe to realize highly ordered truncated cone shaped InGaAs nanowire arrays. Fabricated InGaAs nanowire arrays exhibited near-unity absorption (average of 93%) for an unprecedented wavelength range from 900 nm to 1500 nm when the nanowire shape and geometry is optimized. Fabricated nanowire arrays with a 350 nm top diameter, 880 nm bottom diameter and 900 nm pitch resulted in the best absorptance spectrum.

Previously developed InP based nanowire quantum sensors exhibited single photon sensitivity and a fast response with 0.6 ns rise time and only 17 ps timing jitter at room temperature. In this thesis, our aim was to extend the single photon sensitivity towards the

near infrared and short-wave infrared wavelengths by using InGaAs as an active material. Our novel nanowire pin photodiodes based on InGaAs displayed remarkable improvement in quantum efficiency (from a typical value of 40% to 287% at 900 nm), including the wavelength band called the "valley of death" (800-1000 nm) where OCT imaging systems operate for enhanced sensitivity and axial resolution for eye imaging. Near-unity absorption combined with a gain mechanism in the nanowires was found to be the driving factor behind this high performance. We also built nanowire-based avalanche photodiodes to introduce a high gain mechanism that is able to detect single photons efficiently in the short-wave infrared. A separate absorption, charge and multiplication avalanche photodiode design based on InGaAs and InAlAs in individual nanowires to avoid band-to-band tunneling in devices made with low bandgap semiconductors only. The devices exhibited an avalanche gain of 40 showing promise towards detecting single photons.

The thesis describes the approach to design nanowire arrays to achieve near-unity absorption, optimization and creation of process recipes to realize nanowire arrays and devices and electrical and optical characterization of fabricated nanowire arrays demonstrating high quantum efficiency with avalanche gain.

Acknowledgements

This work would not have been possible without the help of several people I had the pleasure to work with. First of all, I would like to thank my supervisor Dr. Michael Reimer who had shown trust in my abilities and hired me (just a little late) for this challenging project. I couldn't survive without his constant support at the darkest times, guidance and understanding. I couldn't wish for a better PhD advisor. I would like to also thank my co-supervisor Dr. Dayan Ban for his valuable guidance and suggestions throughout my PhD studies. I should also thank Dr. Jonathan Baugh, Dr. Michal Bajcsy and Dr. Adam Wei Tsen for allowing me use their lab space and equipment for device characterizations that we didn't have in our labs and for their valuable feedback and suggestions for my research. I would like to also thank Prof. Karim Karim for his valuable insight and feedback on this project.

During this challenging project, I had the chance to work with some amazing people and learned a lot from them. Special thanks belongs Dr. Lin Tian for helping me build the photocurrent measurement setup, staying late for measurements and I would like to thank Dr. Francois Sfigakis who was always available for discussion and gave me a different perspective on challenging problems. I would like to also thank Sasan Vosoogh-Grayli for his help with optical measurements, analysis and his recommendations for PhD life. I would like to thank Brad van Kasteren for his help and contributions to our project.

I am grateful to the valuable members of QNFCF Dr. Nathan Nelson-Fitzpatrick, Dr. Sandra Gibson, Dr. Lino Eugene, Dr. Greg Holloway for their help developing and optimizing nanofabrication recipes, which was a crucial part of my work.

I am very grateful to my lab mates Dr. Arash Ahmadi, Dr. Mohd Zeeshan, Nachiket Sherlekar, Matteo Pennacchietti, Brady Cunard, Sonell Malik, Sayan Gangopadhyay for helping me in the lab and for always fun chats and laughs.

I would like to thank my close friends Dr. Levent Aygun, Baris Saydere, Dr. Alican Noyan, Dr. Inci Noyan for their caring friendship and suggestions about PhD life in general.

I would like thank my lovely parents for their sacrifice, love and patience with me and my dear brother Goktug for his love and support. I would like to thank my parents-in-love Mehmet and Esin, and my brother-in-law Berke for their warmth and support. I would like to say many thanks to Toros, who was a big part of my life and gave me love. Finally my wife, Merve, has been with me during all the good and bad, throughout this journey. I couldn't have done it without her.

Dedication

In loving memory of my father, Cemalettin Tekcan, who has always been an inspiration and a hero to me.

Table of Contents

Author's Declaration iii

List of Tables xiii

List of Figures xiv

1 Introduction 1

1.1 Broad range of applications . . . 2
1.2 III-V photodiodes at NIR and SWIR . . . 4
1.3 State-of-the-art single photon detectors . . . 5
1.4 Semiconductor nanowire photodetectors: Path to near-unity absorption . . . 6
1.5 Motivation . . . 8
1.6 Organization of the thesis . . . 9

2 Design of p-i-n and avalanche photodiodes for nanowire arrays 11

2.1 Photodetector evaluation metrics . . . 12
2.1.1 Responsivity/External Quantum Efficiency . . . 12
2.1.2 Noise/dark current . . . 12
2.1.3 Temporal response . . . 15
2.2 P-I-N photodiodes . . . 16
2.2.1 Avalanche multiplication . . . 20

2.2.2 Single photon avalanche diodes . . . 24
2.2.3 Material selection and growth . . . 25
2.3 Nanowire p-i-n diode design . . . 28
2.3.1 Optical design considerations . . . 28
2.3.2 Electrical design considerations . . . 29
2.3.3 Avalanche photodiode based on p-i-n structure . . . 31
2.3.4 Surface states of nanowires . . . 33
2.4 SACM avalanche diode design for nanowire arrays . . . 35
2.5 Experimental methods and optical characterization setups . . . 39
2.5.1 Dark current-voltage characteristics . . . 39
2.5.2 Optical setups for characterization . . . 40

3 Near-unity absorptance nanowire arrays 42
3.1 Nanowires for near-unity absorption . . . 42
3.2 Enhanced absorption by nanowire arrays . . . 43
3.3 Narrowband absorber . . . 45
3.4 Route to broadband absorption . . . 47
3.5 Device measurements . . . 49
3.6 Conclusion . . . 52

4 Fabrication of Nanowire arrays 53
4.1 Process Flow . . . 53
4.2 MBE growth of semiconductor layer stack . . . 54
4.3 Preparation of hard masks for nanowire creation . . . 56
4.4 Top-down nanowire etching . . . 59
4.5 Surface passivation . . . 65
4.6 Planarization and contact formation . . . 67

5 InGaAs p-i-n nanowire array photodiodes **70**
5.1 Device fabrication and packaging 70
5.2 Current-voltage characteristics 71
5.2.1 Dark current improvement after cleaving the edges 77
5.2.2 Nanowire diameter 77
5.3 Photocurrent of InGaAs nanowire photodiodes 80
5.4 Spectral responsivity of InGaAs nanowire photodiodes 83

6 Nanowire array avalanche photodiodes **89**
6.1 Device fabrication 89
6.2 Optical properties of InGaAs-InAlAs nanowires 90
6.3 Device structure and dark current characteristics 90
6.4 Avalanche gain 93
6.5 Zener breakdown and microplasmas 96

7 Conclusion and future outlook **98**
7.1 Summary of the results 98
7.2 Future outlook 99

References **101**

APPENDICES **117**

A Appendix A **118**
A.1 Band-to-band current calculation of InGaAs and InAlAs 118

B Appendix B **120**
B.1 Improved Model Accuracy of the Metamaterial with Tapered Nanowire Metaatoms 120
B.2 Effect of Tapered Nanowire Height on the Metamaterial Absorption Efficiency 121

B.3 Growth and Characterization of the Indium Gallium Arsenide Film 121
B.4 FTIR Measurement 123
B.5 FTIR Data Processing 123
B.6 Optical Properties of the Tapered Nanowire Metamaterials with Varying Metaatom Unit Cells 124

List of Tables

2.1 Material properties of semiconductors that were considered in this study . 26

4.1 Investigated Inductive Coupled Plasma - Reactive Ion Etching recipes to etch InGaAs and InAlAs 61

5.1 Device identification (ID) numbers corresponding to configurations with nanowire top diameter and pitch values. 73

List of Figures

2.1 Schematic of noise sources of a photodetector 13
2.2 Principle operation of a pin photodiode 16
2.3 Dark current sources of a p-i-n photodiode shown within the energy band diagram 18
2.4 Avalanche multiplication 21
2.5 Electrical simulations of band-to-band tunneling and SACM device energy band diagram 23
2.6 Energy gaps and lattice constants of commonly used III-V semiconductors 27
2.7 Simulated cross-sectional absorption profile in an InGaAs nanowire array . 30
2.8 Designed InGaAs photodiode structure 32
2.9 Simulated band bending due to the nanowire surface states. The energy band diagram of the cross section for the simulated InGaAs nanowire with diameters 34
2.10 Reverse bias current and electric field profile simulations of separate absorption, charge, and multiplication layers of an avalanche photodiode for different charge layer doping densities and punch-through voltages 37
2.11 Designed SACM avalanche photodiode parameters and the corresponding electric field profile at the breakdown voltage of -44V 38
2.12 The optical characterization setup used to measure the single photon detection characteristics of the fabricated nanowire array avalanche photodiodes 40

3.1 Enhanced light absorption with nanowire arrays 45
3.2 Narrowband near-unity absorptance of cylindrical 1400 nm tall InGaAs nanowire arrays 46

3.3 Finite-difference time-domain simulations of the broadband absorption efficiency for tapered InGaAs nanowires. 48
3.4 Near-unity nanowire metamaterial absorption. 50

4.1 Process flow of InGaAs nanowire array photodiode fabrication 54
4.2 Device layer stacks of InGaAs pin and InGaAs-InAlAs separate absorption, charge and multiplication avalanche photodiodes layer stack deposited by molecular beam epitaxy 55
4.3 X-ray diffraction measurements and Nomarski microscope images for InGaAs p-i-n and InGaAs-InAlAs SACM avalanche photodiode thin films . . 57
4.4 Nanowire array pattering with e-beam lithography and metal mask deposition 58
4.5 Scanning electron microscopy images of etched SiN_x using inductive plasma coupled - reactive ion etching system 59
4.6 Scanning electron microscope images of InGaAs nanowire array etched with varying recipes Cl_2/CH_4 ratio 62
4.7 InGaAs nanowire array fabrication 63
4.8 InGaAs inductively coupled plasma reactive ion etching nanowire array fabrication with varying RF power 64
4.9 InGaAs nanowire sidewall smoothening 65
4.10 Etching BCB layer to expose nanowire tops and depotision of ITO contacts 68
4.11 Microscope and scanning electron microscope images of the final fabricated device structure 68

5.1 Device fabrication and packaging of InGaAs p-i-n nanowire array photodiodes 72
5.2 Current voltage characteristics of a fabricated InGaAs p-i-n mesa device and simulated current voltage curve fitted with the measurements 73
5.3 Current-voltage characteristics of fabricated nanowire array photodiodes based on InGaAs p-i-n structure 75
5.4 Forward bias characteristics of InGaAs nanowire array p-i-n photodiode . . 76
5.5 The effect of cleaving the sidewalls of the chips on the diode performance . 78
5.6 Comparison of diode dark current and capacitance of devices with different nanowire top diameter 79

5.7 Photo and dark current measurements of InGaAs p-i-n photodiodes 81
5.8 Gain mechanism in InGaAs p-i-n photodiodes 82
5.9 Measured spectral responsivity and external quantum efficiency of the InGaAs nanowire p-i-n photodiodes with a Ti:Sapphire laser 84
5.10 Measured photocurrent spectra with FTIR system 85
5.11 Calibrated InGaAs nanowire array p-i-n photodiode spectral responsivity using Ti:Sapphire laser and FTIR system and comparison of external quantum efficiency with commercially available sensors 86
5.12 Internal quantum efficiency of InGaAs nanowire array p-i-n photodiodes . . 87

6.1 SEM images of fabricated InGaAs/InAlAs nanowire array 90
6.2 Optical properties of InGaAs-InAlAs nanowire array photodiodes 91
6.3 Designed SACM device architecture incorporating InGaAs as the absorption region and InAlAs as the multiplication and charge layers 92
6.4 Dark current voltage characteristics of nanowire based SACM avalanche photodiodes at different temperatures 93
6.5 Dark current characteristics of separate absorption multiplication and change layers device architecture nanowire array device 94
6.6 Dark and photo current characteristics of nanowire array SACM avalanche photodiodes 95
6.7 Dark and photocurrent voltage characteristics of an nanowire array SACM avalanche photodiode at 100 K excited with increasing optical powers . . . 96
6.8 Dark current voltage sweeps faulty devices 97

B.1 The effect of height on the absorption response of the InGaAs tapered nanowire metamaterial 122
B.2 Complex refractive index and calculated absorption coefficient of MBE grown InGaAs 122
B.3 The calculated absorption efficiency of the fabricated nanowire metamaterial before and after the thin film interference background correction 124
B.4 The tilted angle scanning electron micrographs of the fabricated metamaterials 125
B.5 The numerical and FTIR experimental absorption efficiency of four different broadband nanowire metamaterial absorbers 126

Chapter 1

Introduction

The cluster of devices and systems that include many consumer electronics from lamps to fiber-optic networks, from cameras to displays and solar cells is called optoelectronics due to the fact that they can make conversions between optical and electrical energy. Being the second most abundant element on earth, Silicon (Si) is the biggest driver behind all consumer electronics ever since scientists and engineers perfected the way to grow and process Si substrates in a cost-effective way. Today, every appliance uses an integrated circuit that contains millions to billions of transistors and every cell phone carries an embedded camera that are made out of Si. However, Si has an indirect bandgap, therefore, fails to perform efficiently in the optical domain. The optical absorption is weak and generating light is troublesome. Alternatively, III-V compound semiconductors have established themselves over the last 30 years and play a key role in the optoelectronic device industry owing to their excellent electron mobilities, direct band gap and low exciton binding energy. Light emitting devices such as lasers [1, 2, 3] and light emitting diodes (LEDs) [4, 5], record breaking solar cells [6] and other components like modulators [7] and amplifiers [8] as well as various types of photon detectors [9, 10, 11] dominantly comprises of III-V semiconductor compounds at their core when high efficiency is a must.

III-V semiconductor-based photodiodes are key components of optical receivers used in today's fiber optic communication networks operating at 1300 nm and 1550 nm owing to low dispersion and low loss. The optical receivers require photodiodes capable of detecting weak optical pulses travelling over long distances to handle high transmission rates of digital information. Data transmission rates must continue to increase as the global Internet traffic increases exponentially [12], where the electric wires and wireless systems hit physical limits. High quality streaming services, photo sharing applications, Internet of Things (IoT) and increasing usage of internet around the world necessitate better internet

infrastructure and data centers that introduces challenges to engineers for developing more sensitive optical receivers. Without a doubt, the central piece to the optical receivers, the III-V semiconductor-based photodiodes need to evolve to ensure the increasing traffic is properly managed.

1.1 Broad range of applications

Improving the sensitivity of existing III-V semiconductor photodetectors goes way beyond fiber optic communication. There is a broad range of technologies from healthcare to autonomous cars and from CMOS defect inspection to satellite communication. For instance, free space satellite to satellite communication technology needs extremely sensitive detectors since the information has to fly vast distances to arrive intact to the receiver. The large distances between satellites or probing deep into the space are referred to as photon starved applications; detecting extremely weak signals down to the level of single photons proves critical.

Optical quantum information is an emerging field where single photon detection is essential. Transmitting a quantum object over a quantum channel ensures near perfect encryption between the sender and receiver. Any eavesdropping attempt decoheres the quantum nature of the travelling object. Quantum Key Distribution (QKD), a protocol to encrypt the information, guarantees a secure channel and relies on single photon detectors to properly detect arriving quantum objects if the information is encoded into photons. This protocol was demonstrated to securely transmit data over long distances [13]. The QKD systems need high efficiency and precise temporal resolution for proper operation. In addition, the system can benefit from being compact and portable in order to extend the applications to satellite based QKD systems [14].

There are other upcoming systems that could significantly benefit from more efficient photodiodes. Light detection and ranging (LIDAR) systems utilize light detectors that work at NIR and SWIR ranges. A LIDAR system typically uses a laser that scans a particular geographical feature and photodiodes collect the severely attenuated reflection signal. Correlating the time of flight yields the distance of the object with precision. The precision largely depends on the detection performance of the photodiode used, therefore, a more sensitive detector can collect weaker reflected signals. In addition, faster detectors (excellent temporal resolution) can record the arrival time of the reflected light more accurately. LIDAR modules typically are mounted on airplanes to access the geographical information that helps with planning and management of land, evaluation of the sea floor and riverbed elevation as well as detection of hazardous natural disasters like flooding. A

detector capable of registering single photons with near-unity efficiency is highly sought after for these applications. Furthermore, a new class of LIDAR systems could potentially revolutionize the autonomous car industry. Currently, LIDAR systems also offer a safe driving experience by ensuring accuracy and precision. They are able to generate 3D mapping of the features surrounding the car during driving. However, LIDAR modules are bulky and expensive increasing the cost of automobiles. It is believed that the cost will go down as the autonomous car technology matures and the market share grows. However, autonomous cars do not yet constitute a big market in car sales since the LIDAR technology cannot scan more than a radius of 100m to avoid collision. On the other hand, Geiger mode LIDAR systems (avalanche photodiodes operated above breakdown) that are capable of detecting single photons could improve the detection of less reflective objects such as black cars. It could also improve the range from 100 m to 400 m which would improve the precision of the objects such as identifying whether a person is facing forward or backward helping the artificial intelligence system to navigate safely [15].

Efficient single-photon detection can also improve technologies for health monitoring. Photodynamic theraphy (PDT) to cure skin cancer is a great example. PDT relies on monitoring molecular oxygen, which is an essential part of life and plays a major role in various biological processes such as cell maintenance and cell termination. Singlet oxygen, an excited state of molecular oxygen, is highly reactive toward organic compounds which makes it attractive to exploit in treatment of cancer and vascular diseases. PDT process relies on electronic energy transfer between a photosensitizer molecule and molecular oxygen. In the photosensitization process, a sensitizer chemical absorbs high-energy photons (VIS or UV); in return, it creates singlet oxygen. The photosensitizer is excited from its ground state to singlet states (higher energy states), then, kinetic energy reduces to its triplet state (or ground state directly) with an internal transition mechanism [16]. Consequently, the triplet state of the photosensitizer relaxes to its ground state while transferring the energy to ground state oxygen and exciting it to singlet state oxygen [16]. Singlet state helps termination of tumor cells; this process can be monitored when oxygen molecule returns to its ground state by emitting photons at a wavelength around 1270 nm. Hence, singlet oxygen luminescence is monitored to elicit and gauge accurate dose of the drug applied to patients. In addition, a microscope-based imaging system can locate the position of singlet oxygen generation [16]. Nonetheless, detection of the direct luminescence calls for high efficiency single-photon detectors that operate at 1270nm. The emission probability of singlet oxygen is very low [17], therefore, singlet oxygen luminescence monitoring requires photon detectors that are sensitive to low intensity light illumination.

Another health-related application of quantum detection can also aid optical coherence tomography (OCT). OCT systems inspect the biological tissue of distinctive layers in

the human retina to detect early signs of blinding diseases. OCT systems operate in a wavelength range from 600 nm to 1300 nm [18]. A detector with high efficiency that can work within this entire wavelength range does not yet exist, a spectral range scanning from 800 nm to 1000 nm is called the "Valley of Death". This limitation reduces the bandwidth and axial resolution of OCT systems operating in this wavelength range. Si detectors have excellent quantum efficiencies in the visible range, however, the quantum efficiency drops to 40 % at 900 nm. On the other hand, InGaAs reaches to its maximum quantum efficiency of 82% above 1000 nm; only 40% is achieved at 900 nm using InGaAs photodetectors. High efficiency detectors working within 800 nm to 1000 nm range will enhance the sensitivity and axial resolution for eye imaging.

1.2 III-V photodiodes at NIR and SWIR

III-V semiconductors are the common material system of choice for applications demanding high efficiency and fast detection. This choice is governed by the electronic properties of III-V semiconductors, as they possess direct band gap with high absorption coefficients accompanied by their high electron mobilities. Si and Ge are the alternative options since they offer cost effective solutions. Nonetheless, the active material of Si and Ge must be made much thicker than III-V materials to fully absorb the same intensity of light, which comes at the cost of a slower device response. In addition, Si has an indirect bandgap of 1.24 eV corresponding to a cut-off wavelength of 1100 nm. Thus, Si becomes transparent to any photons with wavelengths longer than 1100 nm. Unlike Si, Ge based photodiodes can operate at telecom bands. Ge has an indirect bandgap energy of 0.67 eV corresponding to a cut-off wavelength of 1.84 μm at room temperature; however, Ge photodiodes are more susceptible to temperature changes and exhibit high dark current and lack the efficiency of III-V based detectors. These shortcomings make Si and Ge detectors inapt for detecting weak optical signals at NIR and SWIR. III-V semiconductor technology can address these shortcomings better but there are other limitations of III-V semiconductors that needs improvement.

The overall performance of III-V semiconductor devices has been steadily improved over the last 30 years by advancement in growth technology. However, defect density is still a major issue in III-V based devices compared to Si. The current performance of photodetectors based on III-V semiconductors is directly dependent on the bottleneck of growth technology. As of today, improving the quality of III-V semiconductor growth still presents a challenging task for researchers, therefore, alternative approaches are needed until the quality of films substantially improve. Our approach is to reduce the total number

of defects by etching away material while also boosting the absorption efficiency by creating tapered nanowire arrays.

1.3 State-of-the-art single photon detectors

The early-stage technology to detect single photon detectors were photomultiplier tubes (PMT). PMTs work on the principle of multiplication of photon induced electrons in a vacuum environment. Cascaded electrodes multiply the electrons by means of impact ionization. This technology is currently seen as archaic, the detection efficiency of (2%) is poor in the infrared (1300 and 1550 nm), it requires high bias voltage (-1750 V) and the timing resolution (1.5 ns) is behind leading state-of-the-art systems [19]. The two leading technologies for single photon detection are semiconductor-based single photon avalanche photodiodes (SPAD) and the superconducting nanowire single-photon detectors [20]. The major problem for semiconductor-based avalanche photodiodes is that the high efficiency is only achieved for a relatively narrow wavelength range and the temporal performance degrades as the efficiency is improved [20]. For instance, commercial Si and InGaAs single-photon avalanche photodiodes have limited efficiencies of only 50% (@ 830 nm) [21] and 20% (@ 1550 nm) [22] for high speed operation. On the other hand, state-of-the-art superconducting nanowire based single-photon detectors overcome this limitation, exhibiting over 90% efficiency with excellent timing jitter (<20 ps) and fast rise times (<1 ns); however, they need to be cooled to cryogenic temperatures below 4K [23]. The need for cryogenic cooling severely restricts the practicality and portability of such detectors.

In addition to the aforementioned semiconductor and superconducting nanowire devices, there are emerging technologies as well but they lack the required all-round device performance essential for detecting single photons. These emerging devices include quantum-dot-resonant tunnel diode devices [24] and quantum dot gated field effect transistors [25], which do not reach the performance level of superconducting nanowire and avalanche photodiode devices. For instance, the detection efficiencies of these emerging technologies are weak. The efficiencies of quantum-dot-resonant tunnel diode devices and quantum dot gated field effect transistors are 6% and 2% [24, 25], respectively, and suffer from low temperature operation. Moreover, there are notable recent work on graphene to detect low intensity light. Graphene-based studies either showed high speed photodetection [26] or high efficiency [27] but not both, and they did not show single photon operation. On the other hand, other types of graphene-based devices showed that they can detect single photons but they are still in their infancy. Therefore, it is not possible yet to compare to them with existing metrics. They also require cryogenic temperatures because of

bolometric-based detection [28].

1.4 Semiconductor nanowire photodetectors: Path to near-unity absorption

Semiconductor nanowires have been subject to extensive research in the fields of optoelectronics and photonics for the last two decades owing to their remarkable optical and electrical qualities that offer potential improvements to the existing technologies [29, 30, 31]. Miniaturization of the active volume offers higher absorption, lower noise, less power consumption as well as wider range of freedom to tune their properties as compared to their bulk counterparts. The size, shape and number of nanowires can be readily changed thanks to the current state of nanofabrication techniques. Nanowires can be fabricated as a single nanowire structure for ultrasensitive bio-detection [32], for an efficient entangled photon source for quantum repeaters [33] or for a nanophotonic system to improve efficiency of integrated optics [34]. On the other hand, nanowire structures can be utilized in an array form to realize an efficient solar cell [35] and to detect single photons [36]. Nanowire structures can be fabricated either by top-down etching or can be grown from a substrate [37, 38] depending on the requirements. They can be made very long to make use of the length and high surface area for biosensors [39] or very short [40] to take advantage of metamaterial properties. They can be fabricated in various shapes such as cones [36], inverted cones [41, 42], hourglasses [43] and cylinders [44]. They can be grown horizontally [44] or vertically [45] depending on the advantage it brings to the specific application. Nanowire growth can also accommodate lattice mismatch as the built-up stress can be relaxed laterally, therefore, integration of III-V on Si platform is possible [46].

Nanowires are low-dimensional structures which can be utilized to adjust the band gap [47] for applications like LEDs [48] and photodetectors [49]. The nanowire shape could help to control beam propagation, absorption and transmission spectra, which lasers [50], waveguides [51], solar cells [52] and photodetectors [46] could take advantage of. Nanowires are also excellent candidates for single photon emitters, when a quantum dot is embedded in the nanowire. The nanowire could also act as a waveguide to direct the beam in desired directions [33].

Nanowire photodetectors are, in particular, one of the most sought-after domains of optoelectronic devices. Nanowires are great tools in terms of manipulating light in the visible and the infrared range, therefore, photodetectors can demonstrate near-unity absorption with proper nanowire array design. In particular, nanowire arrays can be designed such

that they can reduce the Fresnel reflections at the air-semiconductor interface by means of forward Mie scattering and coupling into waveguide modes [53]. Moreover, the geometrical shape of the nanowire can perform natural filtering, i.e., they can be selective or unselective based on the designed geometry [54, 55]. Cylindrical nanowire arrays can achieve narrow band absorption with high efficiency, whereas tapered nanowire arrays can absorb a much wider range of the spectrum [54]. The nanowire geometry, taper angle, top and bottom diameter as well as nanowire separation are some of the parameters used to optimize the absorption profile (detailed analysis is presented in Chapter 3).

Single nanowire photodetectors are actively being researched. A single nanowire will limit the dark current and noise due to the miniscule volume. Thus, due to the low dark noise, it can achieve very high sensitivity (I_{photo}/I_{dark}) down to single photons [56, 57]. In addition, the small volume of the nanowire can lead to excellent temporal resolution thanks to the highly confined nanowire geometry. However, the efficiency drops dramatically since the optical beam is much larger than the nanowire due to the diffraction limited spot achieved by the objective lens. Therefore, practicality of those sensors becomes an issue. Furthermore, electrical contact fabrication is a challenge for a single nanowire since the contact area is a tiny fraction of the already minuscule volume. As a result, the high contact resistance limits the bandwidth of the photodetectors.

In contrast to single nanowire-based photodetectors, arrays of nanowires is a promising alternative. Typical devices contain hundreds to thousands of nanowires, so the device diameter can be scaled up to be comparable to typical beam sizes used in optical fiber or free-space communication for near-unity coupling to the device area. The effective contact resistance improves significantly because of contacting thousands of nanowires. In addition, the device capacitance drops to a much smaller value as compared to bulk counterparts as a result of reduced active-device area. Therefore, the bandwidth can be above 100 GHz, which is desirable for fiber optic communication systems.

Similar to bulk photodiodes, the sensitivity of nanowire photodiodes can be improved by introducing a gain mechanism. In general, photoconductive gain and avalanche gain are the two main types of gain mechanisms for high efficiency photodetection. Photoconductive gain is a slow process limiting the bandwidth and response time to milliseconds [58, 59] but avalanche gain can enable fast response times in the order of picoseconds with high efficiency [36, 60, 61]. Nanowire-based photodiodes operating as free running single photon avalanche diodes was also demonstrated [62], however, the photon detection efficiency was a major issue and still needs improvement. Room temperature operation is desired but single photon avalanche diodes require very sensitive detection, therefore, photodiodes are cooled down to 200K to suppress dark current/dark count sources.

1.5 Motivation

There is an ever growing need for detectors of light from the visible (VIS) to long wave Infrared (LWIR) that are sensitive enough to detect single photons possessing a miniscule energy of 10^{-19} J. Current technologies offer high performance only on a few avenues of device metrics but all-around capability of quantum detection is lacking in the majority of existing systems and are mostly overlooked. Applications excelling in one category can be impractical, where use of practical systems proves futile in certain situations. For instance, the requirement of cryogenic cooling for superconducting nanowire single photon detector (SNSPD) technology limits their use in applications such as LIDAR systems in aircrafts, autonomous cars, and quantum communication systems deployed in satellites. Satellite quantum communication, in particular, benefit from single photon detectors with high detection efficiency and precise timing resolution at 1550 nm. As good as SNSPD devices perform at 1550 nm, their deployment in space shuttles and satellites is infeasible. Due to portability issues, semiconductor SPADs must be used. However, InGaAs SPADs detection efficiency of 10% in free running mode, timing resolution of 0.2 ns and only a bandwidth of 100 MHz restricts QKD operation [22]. Furthermore, a one size fits all type of detector could be of help to many technologies. Higher detection efficiency semiconductor SPADs can replace some of the SNSPDs thanks to their lower cost and mild temperature cooling that do not need bulky and costly equipment.

The art of engineering demands bridging superior performance traits with practicality by introducing alternative perspectives to enhance performance metrics and to eliminate limiting aspects. Semiconductor nanowire avalanche photodiodes offer an alternative path toward enhancing the performance metrics and eliminating the limiting aspects. Semiconductor nanowires exhibit remarkable optical and electrical properties that enhance and repair some of the limiting aspects of semiconductor-based photodiodes. Nanowire arrays can greatly help photon starved situations benefiting from high sensitivity without trading-off fast time response and precise timing resolution. They can be a footprint for photodetectors and CCD cameras used to inspect biological systems in the NIR range or so called "valley of death" range. This thesis presents an alternative approach towards devices that can overcome the low quantum efficiency and low timing resolution drawbacks by developing a novel semiconductor nanowire array photodiode capable of detecting light with high efficiency over a broad wavelength range from the visible to SWIR and at temperatures compatible with thermo-electric cooling only.

In this thesis, we have optimized $In_{0.53}Ga_{0.47}As$ (hereafter InGaAs) tapered nanowire array structures capable of achieving near-unity absorption by performing FDTD simulations. Next, we have successfully developed a novel top-down nanofabrication recipe to

create highly ordered, high yield, low surface roughness tapered nanowire arrays using InGaAs with an ability to tune the optical absorption spectra by optimizing the nanowire shape and spacing. The InGaAs nanowire arrays demonstrated a near-unity absorption property with wide detection range spanning from the visible to SWIR. Next, the p-i-n photodiodes were built using InGaAs nanowire arrays and the performance of the photodiodes were optically and electrically characterized. The results obtained were compared with existing commercial devices.

Furthermore, the gain mechanism that is exploited in avalanche photodiodes to achieve single-photon detection can easily be incorporated into the nanowire geometry. The gain mechanism can further increase the sensitivity of InGaAs nanowire arrays with enhanced absorptance. However, using InGaAs photodiodes for gain will result in high leakage currents due to band-to-band tunneling. Thus we have implemented separate absorption, charge and multiplication avalanche photodiodes as a nanowire array. We have used a wider band gap material ($In_{0.52}Al_{0.48}As$, hereafter InAlAs) as the multiplication layer in conjunction with InGaAs as the absorption layer. We have characterized the performance of the nanowire array avalanche photodiodes at from 100K to 250K.

1.6 Organization of the thesis

The organization of the rest of the thesis is as follows:

Chapter 2 provides the necessary technical background of the semiconductor device physics to explain photodiode operation, performance metrics and design considerations. It involves device operation of p-i-n photodiodes, avalanche breakdown, gain mechanism to detect weak optical signals and path to detecting single photons. The chapter ends with the considerations applied to the design of the fabricated devices from the perspective of nanowire arrays and the modifications to the common design principles to successfully demonstrate higher performance with nanowire arrays.

Chapter 3 focuses on the optical properties of nanowire arrays and design principles to achieve near-unity absorption. It also investigates the behavior of light coupling and high absorption using optimized nanowire arrays based on InGaAs.

Chapter 4 describes the methodology of realizing III-V semiconductor nanowire arrays in the cleanroom facility, recipe optimizations and end-to-end device fabrication.

Chapter 5 presents the results and discussion on InGaAs p-i-n photodiodes based on tapered nanowire array geometry. The analysis of the results are also included as well as the improvements and shortcomings.

Chapter 6 extends the design idea of nanowires to single photon avalanche diodes based on separate absorption, charge and multiplication layer design. It briefly describes the device fabrication, then discusses the findings of optical and electrical characterization.

Chapter 7 concludes the thesis by providing a summary of the results, their implications and potential next steps to improve the state-of-the-art devices. It gives a comparison of the developed technology with existing photodetection systems.

Chapter 2

Design of p-i-n and avalanche photodiodes for nanowire arrays

This chapter summarizes the fundamentals of semiconductor device physics in order to realize high sensitivity photodiodes using the remarkable properties of nanowires. Basic principles of the photodiode operation are described and performance metrics and strategies to maximize those metrics are discussed. The discussion also touches upon the unique properties of nanowires and key considerations when designing a nanowire based photodiode. The design of the nanowire based photodiodes slightly differs from bulk photodiodes based on planar or mesa structures. Embedding the photodiode design into a nanowire geometry provides improvement in more than one metric, offering a pathway towards realizing a new class of more sensitive devices that could be used in various technologies such as optical communication and health monitoring as discussed in Chapter 1.

Photodiodes operate based on creation of electron-hole pairs upon photo excitation (photoelectric effect) and successful arrival of those pairs to the device electrodes. In principle, the chain of events starts with absorption of a group of photons or a single photon and subsequent generation of electron-hole pairs. Then, the electron-hole pairs are separated with the built-in electric field and transported (if exists, accompanied by amplification using internal gain mechanism) to device electrodes. Next, the electrons and holes are collected by the electrodes and device current increases in the external circuitry with respect to optical excitation. The quality of this operation is determined by the success rate of the absorption and collection of the carriers, the speed of the detection event and the level of noise. Nonetheless, trade-off exists as one cannot achieve the best metric in all categories. Nanowire arrays aid to alleviate the trade-off by increasing the absorption and collection efficiency while also increasing the speed of the detection event. The noise level

can also be reduced with the nanowire geometry provided that the nanowires have proper surface passivation.

2.1 Photodetector evaluation metrics

To properly evaluate and compare photodetectors, a set of performance metrics is used. The common key metrics are responsivity/external quantum efficiency, temporal response and noise characteristics.

2.1.1 Responsivity/External Quantum Efficiency

Responsivity is a measure of the generated photocurrent in response to power of the incident light. Similarly, the external quantum efficiency is a parameter that describes the ratio of photogenerated carriers to the number of photons incident onto the detector. It gives detailed information on the absorption and carrier collection efficiency when plotted as a function of wavelength at different voltage biases. The responsivity is given by:

$$\mathfrak{R} = \eta \frac{q}{h\nu} = \frac{I_{ph}}{P_{opt}}, \tag{2.1}$$

where η is the external quantum efficiency, q is the elementary charge, h is the Planck's constant, ν is the frequency of the light, I_{ph} is the photocurrent and P_{opt} is the incident optical power. The responsivity has units of A/W, whereas the external quantum efficiency is a unitless number between zero and one. $\eta = 1$ represents "perfect" photodetection, whereby every incoming photon is successfully converted into an electron-hole pair and collected by the external circuitry. Less than 1 means that some portion of the photons are reflected, transmitted or recombined via non-radiative or radiative decay channels.

2.1.2 Noise/dark current

In an ideal diode model, it is assumed that the current is zero when the diode is reverse biased. In real devices; however, a non-zero "dark current" is always observed. The dark current arises from electrons making a leap from valence band to conduction band due to semiconductor imperfections. Once electrons jump to the conduction band via imperfection sites (also leaving holes behind in the valence band), they are inseparable from photogenerated electrons that make direct transition to the conduction band (similarly

photogenerated holes). As a result, they raise the photodetection floor, introducing noise to the incoming photons and reduce the contrast between light and dark conditions. Photodiodes are in general more sensitive when they have lower dark current. It is a designer's goal to minimize the dark current. There are three major noise sources, which are background radiation noise, thermal noise and shot noise as shown in Figure 2.1a [63, 64]. Background radiation noise can be eliminated if the photodiode is placed in an optical enclosure. Thermal noise arises from the internal resistance of the external circuitry or amplifier before the final output. The equivalent circuit is given in Figure 2.1b. i_p is the photocurrent, i_s is the shot noise as given as the root mean square, C_j is the junction capacitance, R_j is the junction resistance which represents the shunt resistance that causes leakage current, R_s is the series resistance which is a combination of space-charge resistance and contact resistance, i_T is the RMS thermal noise current, R_L is the load resistance and R_I is the input impedance of the external circuitry.

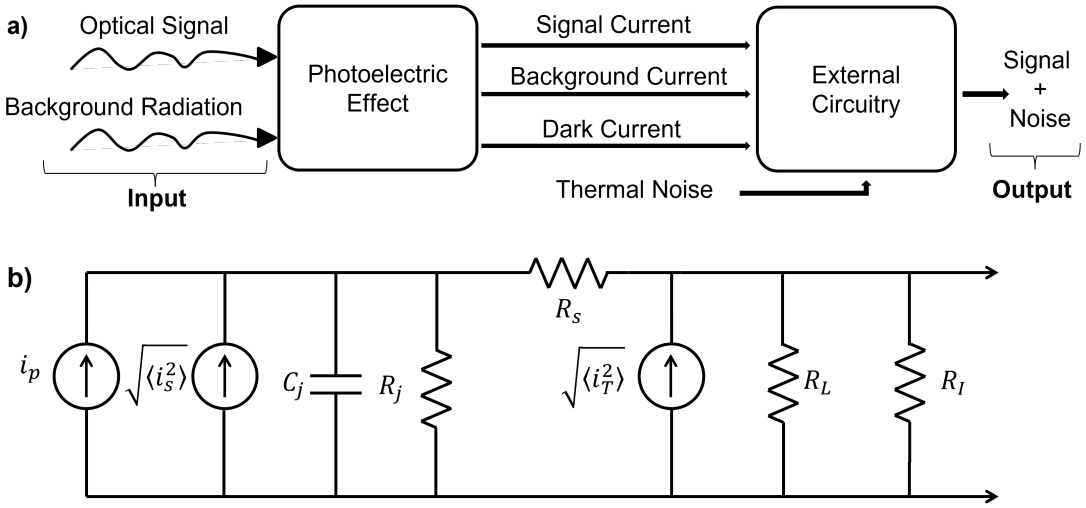


Figure 2.1: Schematic of noise sources of a photodetector. a) The photodetection process with the addition of noise sources. Photodiodes absorb an optical signal and background radiation. Electron-hole pairs are generated. Dark current is generated internally by the photodiode. Shot noise arises from the statistical nature of dark, signal and background current. Thermal noise is added to the external circuitry. b) The equivalent circuit of a typical photodetector including the noise sources. The figure is reproduced from reference [64].

The shot noise originates from the discreet nature of photons and electrons. Photon pulses consist of a discreet number of photons, and photons cannot arrive at a detector with

perfect synchronization. The average number of photons can be the same but individual pulses have little fluctuations. These fluctuations induce fluctuations in the electrical current resulting in noise. The shot noise, also known as quantum noise, arises from the random arrival time of photons that produces a flicker effect in device current. Similar to photons, dark current generation in a semiconductor behave similarly. Dark current sources in a semiconductor is of statistical nature, random generation in time causes additive noise to the detector. The noise power spectral density of shot noise combining the photon and dark current is

$$\sigma_{shot}^2 = 2q(I_{photon} + I_{dark}) = 2q(\Re P_{opt} + I_{dark}), \tag{2.2}$$

where q is the elementary charge, I_{photon} is the photocurrent, I_{dark} is the dark current, $\Re$ is the responsivity, P_{opt} is the optical power. The root mean square noise current is

$$\langle i_{shot}^2 \rangle = \sigma_{shot}^2 BW, \tag{2.3}$$

where BW is the bandwidth of the receiver. The thermal noise, also known as Johnson noise, is generated by the load resistor of the photodetector. Contact resistance also contributes to the total thermal noise. The noise power density due to thermal noise is

$$\sigma_{th}^2 = \frac{4k_B T}{R_{eq}}, \tag{2.4}$$

where k_B is the Boltzmann constant, T is the temperature and R_{eq} is the equivalent resistance of the circuit in Figure 2.1b. The mean square noise current is similarly

$$\langle i_{th}^2 \rangle = \sigma_{th}^2 BW. \tag{2.5}$$

The signal-to-noise (SNR) ratio of a detector is defined as:

$$SNR = \frac{\langle I_{photon}^2 \rangle}{\langle \langle i_{shot}^2 \rangle + i_{th}^2 \rangle + \langle i_{amplifier}^2 \rangle} = \frac{(2q\Re P_{opt})^2}{2q(I_{photon} + I_{dark})BW + \frac{4k_B TBW}{R_{eq}}}, \tag{2.6}$$

where $\langle i_{amplifier}^2 \rangle$ is generated by the transimpedance amplifier connected to the photodetector. The numerator is the mean photocurrent originating from the optical signal and the denominator is the statistical variations of that photocurrent due to the sources of noise mentioned above.

A metric called noise equivalent power (NEP) describing the minimum detectable power of a photodetector is also commonly used to evaluate the sensitivity [65]. NEP is described as the optical incident power onto a detector that produces a signal to noise ratio of 1 per unit bandwidth. In other words, it is the noise floor where the optical signal is barely

detectable on the waveform. The bandwidth term comes into the picture since the majority of applications require modulated signals. The NEP is given by:

$$NEP = \frac{P_{opt}}{\sqrt{BW}} = \sqrt{\frac{4kT}{\Re^2 R_{eq}}}. \tag{2.7}$$

2.1.3 Temporal response

The response time of a detector to an optical signal and the time duration it restores to the dark state determines the temporal response of the detector. In general, the rise/fall time is given to describe the temporal response speed of a photodetector. The transient response is determined by the time of photogenerated carriers traveling through the device structure, reach the electrodes and contribute to the electrical current in the external circuitry. In terms of the photodiode operation, carriers move with drift reaching to saturation velocity under sufficiently high electric field in the depletion region. To increase the quantum efficiency, the thickness of the depletion region is extended. However, extension of the depletion region thickness will translate into a delay in the response time due to the longer path that the photogenerated carriers have to travel. In addition, a carrier generated in the quasi-neutral regions within the Debye length of the depletion region will diffuse into the depletion region and then travel to the contacts. Diffusion is a much slower process than drift. As a result, the carrier collection through diffused carriers will further delay the response time. Finally, the photodetector response is affected by the RC time constant of the system, where the depletion region capacitance and the equivalent resistance dominate the RC time constant. The device capacitance and the equivalent resistance determines the device bandwidth. The 3 dB cut-off frequency is given as:

$$f_c = \frac{1}{2\pi RC}. \tag{2.8}$$

The device capacitance can be reduced by increasing the intrinsic layer but this comes at the cost of increasing the carrier travel time, or the device area can be made much smaller but this will limit the optical spot size that can be detected. Additional factors such as the stray capacitance and leakage current (shunt resistance) play a significant role in the total response time. Ideally, the stray capacitance should be minimal and the shunt resistance should be infinity. Trade-offs have to be considered based on the specific needs of the project when a conventional photodiode structure is used.

2.2 P-I-N photodiodes

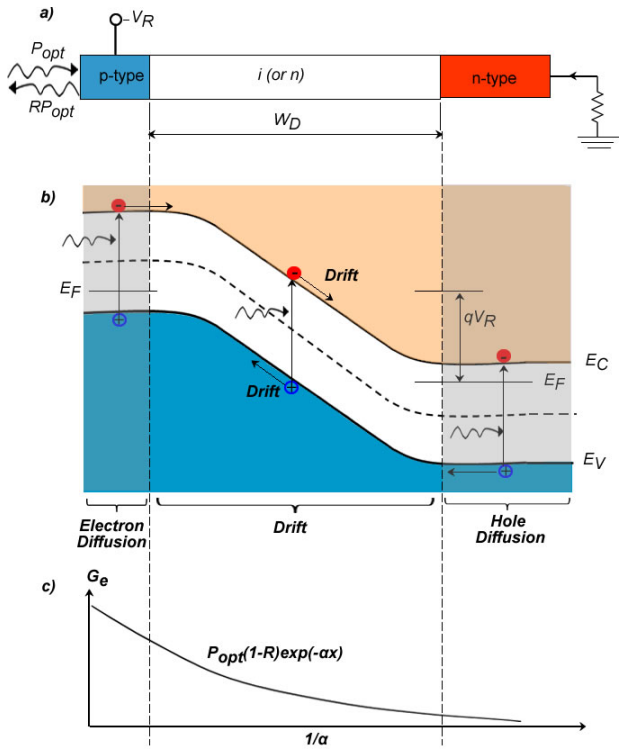


Figure 2.2: Principle operation of a p-i-n photodiode. a) Cross-sectional view of a hypothetical p-i-n photodiode illuminated from the left hand side. The intrinsic region defines the depletion region, therefore, the absorption region. b) Energy band diagram of the p-i-n photodiode depicting the detection of a photon under reverse bias. c) The intensity of light decays with respect to the absorption coefficient (distance). The figure is reproduced from reference [64].

P-i-n photodiodes are a special class of p-n junctions to maximize light detection and still operate at high bandwidth. The layer i (intrinsic layer) is sandwiched between p-doped and n-doped layers giving ample freedom to extend the absorptive region as shown in Figure 2.2. Photogenerated carriers upon absorption in the i region are swept to the opposite sides of the junction. The incoming optical signal is dominantly absorbed within the depletion region, which is determined by the thickness of the intrinsic region (i region). The absorption process can also take place in the quasi-neutral n and p buffer layers. The generated carriers in those regions will diffuse to the depletion region if they are within

the diffusion length and are swept by the electric field. On the other hand, the expanded intrinsic region introduces a trade-off between quantum efficiency and response time of the photodiode, therefore, one has to decide on the intrinsic region thickness based on the application. The general p-i-n photodiode operation relies on the incoming photons absorbed within the intrinsic region that needs to be fully depleted to achieve the highest quantum efficiency possible as shown in Figure 2.2b.

The energy band diagram of a typical p-i-n diode is depicted in Figure 2.2b. The electrical current under reverse bias (Drift current) is dominated by minority carriers being transported with the electric field. In general, the heavily doped top region where the excitation arrives (p-type in Figure 2.2a) is chosen to be short enough as to not absorb a significant portion of the optical input. The primary reason for that is carriers generated by absorption will be outside of the depletion region where they will recombine. They can also slowly move towards the depletion region by diffusion but slow diffusion will delay the response time of the optical detection. Figure 2.2c shows how the carrier generation is dependent on the material depth. The absorption in bulk materials follows an exponential decay as a function of the absorption coefficient α. Some portion of the generated carriers in the p and n type of the junction can also contribute to the photocurrent. If the carriers are within the Debye length of the junction, those carriers can flow into the depletion region via diffusion where they will be swept under the electric field to opposite sides of the junction.

The created carriers due to photon excitation can then give rise to a photocurrent which has to be higher than the dark current. Aside from carriers created by photon absorption, there are other sources of carrier generation in the semiconductor in the absence of light excitation. These sources are diffusion current, thermal generation-recombination current (also known as (SRH) Shockley-Read-Hall current), tunneling current and avalanche current. Each dark current mechanism and the associated carrier action is depicted in Figure 2.3.

The diffusion current arises from the thermally generated minority carriers outside of the depletion region but diffusing into the depletion region. The diffusion current is given by:

$$I_{diff} = I_s\left(e^{\frac{qV}{kT}} - 1\right), \tag{2.9}$$

where I_s is the saturation current, V is the applied voltage, q is the electronic charge, k is the Boltzmann constant and T is the temperature. This equation also describes the diode forward bias current since the diode current at forward bias is dominated by the diffusion

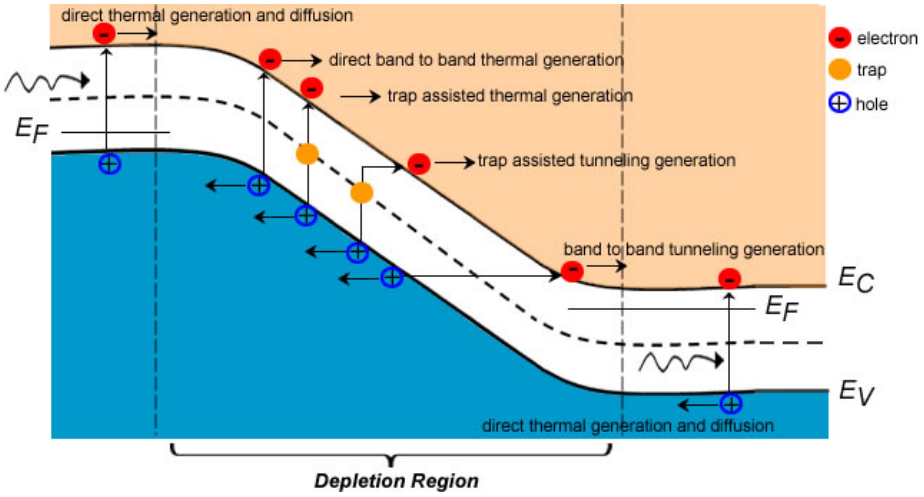


Figure 2.3: Dark current sources of a p-i-n photodiode shown within the energy band diagram. Free carriers can be generated without the absence of light through thermal generation (direct or via traps), tunneling (band-to-band or trap-assisted) or diffusion (from quasi-neutral regions) in a p-i-n junction. The generated carriers will contribute to the device current. The figure is reproduced from Reference [66].

current. The saturation current for a mesa punch-through p-i-n structure can theoretically be calculated as [67]:

$$\begin{aligned} I_s &= qn_i^2 \frac{\pi}{\tau_d^{1/2}} \Big((\frac{D_n^{1/2}}{N_A}) \frac{d^2}{4} + \frac{D_p^{1/2}(W_d)}{N_D} \Big) \\ &\approx qn_i^2 \pi \sqrt{\frac{D_p}{\tau_d}} \frac{W_d}{N_D}, \end{aligned} \tag{2.10}$$

where n_i is the intrinsic carrier concentration, D_n and D_p are the minority carrier diffusion coefficients, N_A and N_D are the acceptor and donor doping concentrations, d is diode diameter, W_d is the depletion region length and τ_d is the minority carrier lifetime of electrons and holes (assuming equal for electrons and holes). Intrinsic carrier concentration is one of the variables in the Equation 2.10 that can significantly change the diffusion current. n_i^2 increases the I_{diff} quadratically; the intrinsic carrier concentration increases exponentially as the material band gap decreases. τ depends on the quality of the film (defect density), depletion region thickness and doping concentrations are within the control of designers. The equation for the intrinsic carrier concentration is

$$n_i = 2(4\pi^2 m_e m_h k^2/h^4)^{3/4} T^{3/2} exp(-E_g/2kT), \tag{2.11}$$

where m_e is the mass of electrons, m_h is the mass of holes, k is the Boltzmann constant, T is the temperature and E_g is the material band gap.

Another important dark current mechanism is the generation-recombination current. This current arises due to traps caused by semiconductor defects and impurities during growth. At low voltages, the trap levels located at the midgap dominantly contribute to the excess dark current. It can be calculated as

$$I_{gr} = \frac{q n_i A W}{\tau_{eff}} (e^{qV/2kT} - 1), \tag{2.12}$$

where τ_{eff} is the effective carrier lifetime, A is the junction area, W is the depletion region thickness, V is the applied voltage, k is the Boltzmann constant and T is the temperature. The recombination generation current changes with the depletion layer volume, given the specific defect density of the material. For an abrupt junction, the depletion layer thickness is calculated for a one sided junction.

$$W(V) = \sqrt{-\frac{2\kappa_s}{qN_D}(V - V_{bi})}, \tag{2.13}$$

where q is the elementary charge, V_{bi} is the built-in potential, κ is the dielectric constant, N_D is the donor concentration, V is the applied bias. When excess electric field is applied, diodes exhibit non-ideal behaviors such as breakdowns. Band-to-band tunneling affects direct band gap semiconductors with small band gaps. Mostly breakdowns are recovarable as soon as the device doesn't generate excessive heat. In most cases, the

$$I_{tun} \cong \gamma A exp(-\frac{\Theta m_o^{1/2} \epsilon_g^{3/2}}{q\hbar E_m}), \tag{2.14}$$

where m_0 is the mass of electron, ϵ_g is the material energy band gap, E_m is the maximum electric field in the junction, $\hbar$ is the reduced Planck constant and Θ is a fitting parameter and found to be around 0.3 for InGaAs [68] and 0.15 for InP [69]. The prefactor γ is dependent on the number of traps. It can be found as [67]

$$\gamma = \left(\frac{2m^*}{E_g}\right)^{0.5} \left(\frac{q^3 E_m V}{4\pi^2 \hbar^2}\right), \tag{2.15}$$

where m^* is the effective mass.

Another source of dark current comes from device surface. Semiconductor surface has dangling bonds and process induced defects. Presence of depletion region reaching to the surface of the semiconductor in turn gives rise to surface generated carriers and promote leakage current. For a circular mesa photodiode the surface generation current can be approximated by

$$I_{s-g} \simeq q n_i s_o A_s = q n_i s_o \pi d W_s, \tag{2.16}$$

where s_o is the surface recombination velocity, A_s is the device surface area $A_s = \pi d W_s$, W_s is the depletion region width. Minimization of surface generation current is necessary to ensure high performance. In general, two distinct approaches were used to suppress surface generation and recombination current. The first method is to grow a heterojunction with a wider band gap material covering the surface for planar type photodiodes [70]. Wider band gap materials are typically chosen so that light is only absorbed in the absorption region as well as to reduce surface generation that scales with the intrinsic carrier concentration n_i. In addition, lattice constant of the each side on the heterojunction has to be the same to eliminate dangling bonds at the interface. Heterointerfaces can act as a surface generation centers unless the epitaxy quality is perfect. The second method to reduce surface generation current is to passivate the semiconductor with an insulating material. It is not feasible to grow epitaxial films on top of already patterned structures. Device configurations like mesa type p-i-n diodes have active regions where the depletion region reaches to the surface. Proper surface passivation can reduce surface recombination velocity. Silicon based photodiodes are advantageous since they can be passivated with thermal oxidation that results in very low recombination velocities [71]. However, oxides of III-V result in poor quality causing high surface recombination velocities. Instead, materials such as SiO_2, SiN_x [72] or Al_2O_3 is deposited to reduce the dangling bonds. The effective surface passivation techniques to reduce surface recombination velocity is discussed in Chapter 4.5.

2.2.1 Avalanche multiplication

Avalanche photodiodes offer at least 5-10 dB more sensitivity than p-i-n photodiodes by taking advantage of their internal gain mechanism provided that the multiplication doesn't introduce additional noise that lowers the overall sensitivity [73]. However, higher sensitivity increases the cost of the growth due to more complex device structures. It also introduces heterojunctions where advanced growth techniques are needed. After the discovery of low dispersion and low loss characteristics of optical fibers at 1300 and 1550 nm wavelengths, researchers transitioned from Si p-i-n and APD technology to InGaAs, which

is capable of detecting photons at those wavelengths unlike Si. InGaAs p-i-n photodiodes reigned the market until they are found to suffer from excess dark currents due to band-to-band tunneling (BBT) when the electric field is increased to achieve impact ionization. Later, the problem is alleviated by using a wider band gap material for the multiplication region while still using InGaAs for the absoption region.

The avalanche multiplication starts by a photogenerated carrier gaining enough energy under strong electric field. The carrier accelerates due to the electric field until it collides with the crystal lattice or an impurity site, transferring its energy to the lattice. If the energy is high enough to bump an electron from the valence band to the conduction band, a secondary electron hole pair forms. This is called impact ionization. Since the secondary carriers are also under the influence of the strong electric field, they also accelerate the same way the primary carrier did, therefore, they gain sufficient energy and transfer their energy to the tertiary electron hole pairs. The primary carrier along with consequent carriers can also contribute to additional ionization events. The process keeps expanding to an increased number of carriers as the electric field is sustained. Some of the carriers may recombine and some travel through without ionization due to its statistical nature but overall the gain mechanism creates a macroscopic current from a single carrier. The overall operation is depicted in Figure 2.4a. Figure 2.4b shows how carriers are multiplied in a p-i-n junction.

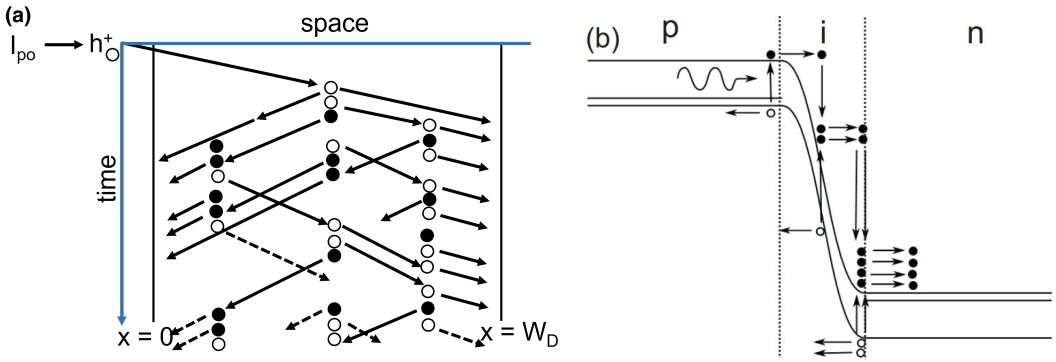


Figure 2.4: Avalanche multiplication. a) A hole enters the avalanche region from the left and creates an extra electron hole pair via impact ionization. The secondary electron and hole will similarly trigger impact ionization events. Therefore, the total number of carriers will multiply. Inspired from Reference [74]. b) Avalanche breakdown demonstrated within an energy band diagram of a p-i-n junction. Taken from reference [75].

The rate which the carrier undergoes impact ionization is characterized by the inverse mean distance between two consecutive collision events that leads to the creation of sec-

ondary electron hole pair. α and β represent the impact ionization rate of electrons and holes, respectively [76, 77]. For a hole initiated avalanche multiplication process, as shown in Fig 2.4, the initial current at the $x = 0$ is $I_p(x = 0) = I_{po}$. I_p will increase as it travels towards the $x = W_D$. Assuming $\alpha = \beta$, at $x = W_D$, the hole current $I_p(x = W_D) = M_p I_{po}$ [64]. Similarly, the electron current $I_n(x = W_D) = 0$ and $I_n(x = 0) = I_{total} - I_{po}$ where the total current $I = I_p + I_n$ [64]. The multiplication factor or the gain can then be calculated by

$$M_n = \frac{I_n(W_D)}{I_n(0)} = \frac{I_{total}}{I_{no}}. \tag{2.17}$$

In the discussion above, α and β were assumed equal, meaning the electrons and holes are equally likely to undergo impact ionization. However, this case is very rare, the majority of the materials have uneven ionization coefficients. Designing an avalanche photodiode requires careful consideration of the α and β or more commonly the ratio $k = \alpha/\beta$ (or $k = \beta/\alpha$). The value of k can determine type of the carrier that initiates the avalanche multiplication. In addition, the difference between α and β may introduce a statistical noise to the avalanche photodiode operation called excess noise. The noise power density due to avalanche process is

$$\sigma^2_{excess} = 2qM^2F(I_{photon} + I_{dark}) = 2qM^2F(\Re P_{in} + I_{dark}), \tag{2.18}$$

where excess noise factor F is defined by McIntyre's expression [76] as

$$\begin{aligned} F(M) &= \langle M^2\rangle / \langle M\rangle^2 \\ &= k\langle M\rangle + (1-k)(2 - 1/\langle M\rangle). \end{aligned} \tag{2.19}$$

The SNR of an avalanche photodiode with the addition of gain and excess noise to the previously discussed noise model can be calculated as:

$$SNR = \frac{\langle I^2_{photon}\rangle}{\langle \sigma^2_{th}\rangle + \langle \sigma^2_{excess}\rangle} = \frac{(M\Re P_{in})^2}{\left(2qM^2F(\Re P_{in} + I_{dark}) + \frac{4k_BT}{R_L}F_n\right)BW}, \tag{2.20}$$

NEP can be derived from finding P_{in}/BW when $SNR = 1$. Choosing M for the best SNR depends on the k dependence of M as in Equation 2.19.

The early avalanche photodiodes working at 1300 and 1550nm wavelengths were based on InGaAs p-i-n structures. However, these p-i-n structures exhibited poor gain and high leakage current relative to the Si and InP based APDs due to the existence of soft knee characteristics in the breakdown current. The studies showed that the soft knee behavior is a result of band-to-band tunneling (BBT) mechanism, which is more prominent in

narrow band gap materials [68, 69]. To illustrate the tunneling issue, Figure 2.5a shows the simulated band-to-band tunneling current for InGaAs (0.75eV) and InAlAs (1.5eV) based on Equation 2.14. In InGaAs device, the BBT onset (1.5×10^5 V/cm) arrives at a smaller bias than avalanche breakdown field (2×10^5 V/cm) leading to high dark current and low sensitivity above 1.5×10^5 V/cm. To alleviate the problem, a heterostructure was proposed that separates the absorption and multiplication layer in avalanche photodiodes [78, 79]. A wider band gap material was chosen for the multiplication layer where band-to-band tunneling probability is small and was used in conjunction with the small band gap material for absorption. That method separates the absorption and multiplication regions in the device, limiting the band-to-band tunneling current. Moreover, a heavily doped field control layer was later introduced in between the absorption and multiplication layers to keep the electric field low in the absorption region to avoid band-to-band tunneling and high in the multiplication region to ensure sustained avalanche breakdown [80]. Furthermore, grading layers, quaternary alloys between the absorption and multiplication regions are used to avoid blockage of carriers at the conduction and valence band discontinuities between heterojunctions. Transit times of carriers were improved notably when grading layers were introduced [81]. Currently, most majority of the avalanche photodiodes incorporate separate absorption, charge and multiplication layers (SACM).

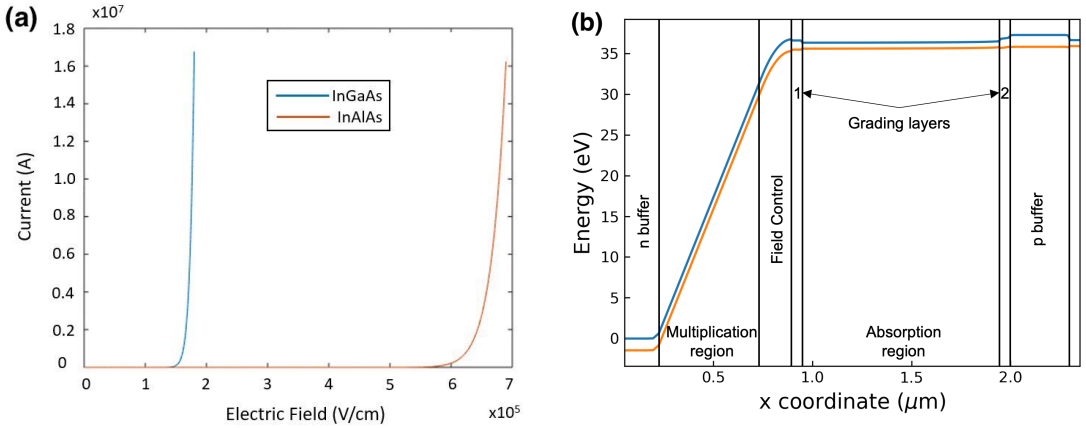


Figure 2.5: Electrical simulations of band-to-band tunneling and separate absorption, multiplication and charge layers device energy band diagram. a) Analytical simulation of band-to-band tunneling current in InGaAs and InAlAs. b) Energy band diagram of a typical separate absorption and multiplication avalanche photodiode, with charge (field control) and grading layers.

In InGaAs-InAlAs SACM APDs, electrons trigger the avalanche breakdown. To illus-

trate, an electron-hole pair is generated in the absorption region which is shown in Figure 2.5b. The primary electron drifts to the left towards the field control and multiplication region whereas the hole drifts to the right side of the device. The electron is injected into the multiplication region traversing through the grading and charge layer. The charge layer ensures the electric field in the multiplication region is sufficiently high for avalanche breakdown as well as it keeps the electric field in the absorption region sufficiently small to suppress tunneling current. A non-zero electric field is still required to drift carriers with saturation velocity to ensure fast detection. Once the electron is injected into the high field multiplication region, it gains enough energy to impact ionize with acceleration. Throughout this process, secondary electron hole pairs will be generated. As the multiplication continues for sequentially generated carriers, a self sustaining avalanche will be created. When the avalanche is self-sustaining and the gain sufficiently high, single photon can be detected.

The diode thermal generation recombination current will also get multiplied with the photocurrent; the total current will change with respect to the internal gain mechanism. The dark current then will be rewritten as:

$$\begin{aligned} I_{g-r} &= qA(\frac{n_i}{\tau_{eff}})_B W,\ V \leq V_p \\ I_{g-r} &\cong qA[\frac{1}{2}(\frac{n_i}{\tau_{eff}})_B x_I(1+M_p) + (\frac{n_i}{\tau_{eff}})_T(W-x_I)M_p],\ V > V_p, \end{aligned} \tag{2.21}$$

where q is the elementary charge, A is the junction area, n_i is the intrinsic carrier concentration, τ_{eff} is the effective carrier lifetime, W is the depletion layer thickness, M_p is the avalanche gain. The subscript A represents the absorption material whereas subscript M represents the multiplication material.

2.2.2 Single photon avalanche diodes

Avalanche photodiodes can also be used to detect single photons with the help of gain mechanism. The separate absorption, charge and multiplication layers architecture is used for single photon avalanche diodes. SPAD devices operate above the breakdown so the operation and design differ from linear mode APDs. APDs work at moderate gains 10-100 below the breakdown voltage in order to keep the SNR at its maximum achievable point [73]. In APDs, thinner multiplication regions yield higher gain-bandwidth product and more deterministic response to input pulses, whereas, SPADs need longer multiplication regions to promote higher probability of breakdown leading to increased gain [82]. In addition, the linear mode APDs can leverage low punch-through voltage to have high

dynamic range, on the other hand, V_p for SPADs is only considered to ensure that the absorption layer is fully depleted at low temperature operation (to minimize the noise).

Since single photon detection using SPADs is a digital event due to counting individual photons, the device characterization is done by inspecting different set of metrics to quantify the detector performance. Photon detection efficiency, dark count rate, afterpulsing, maximum count rate, timing jitter and spectral range are considered the most prominent metrics to quantify the performance [20]. **Photon detection efficiency** defines the efficiency of successfully registering single photons. With a single photon injected into the device, the photon will be absorbed and converted into an electron-hole pair. Then, the electron and hole will be separated by the electric field, each carrier will trigger subsequent impact ionization events and reach to the contacts. After a macroscopic current is detected, the quenching circuit and photon counter will register the photon. The whole process needs to be optimized as to not miss any incoming photon. **Dark count rate** is the false counts in the absence of incoming photons. It has to be minimized since the dark counts are the leading noise source for single photon detection. The **afterpulsing** is another type of noise mechanism. When a large current passes through the device after a detection event, some carriers get trapped in the semiconductor defects. The detrapping time of those carriers is much longer than the photon detection time, so trapped carriers will trigger a false count by starting an avalanche event. To ignore afterpulse dark counts, long dead times are used. As a result, the maximum count rate decreases. The **maximum count rate** is the maximum number of photons counted per unit time (typically per seconds or Hz). This excludes any dark counts, so higher maximum count rate is a measure of detection speed of the SPAD. **Timing jitter** is the statistical uncertainty in time between the photon absorption to the detection of the pulse with the electronics. This includes the location of absorption of individual photons, how fast carrier can move inside the device and how fast can the quenching electronics respond. **Spectral range** is another important metric. It represents the range of wavelengths which the detector is sensitive to. A wider range can improve the flexibility of the detection system.

2.2.3 Material selection and growth

A critical part of designing a photodiode is choosing the right material for the active region of the diode. Strong absorption can only occur when the incoming photons have higher energy than the energy band of the absorptive material. To make a photodiode responsive to 1550 nm for instance, the energy band gap of the material should be at most 0.8eV according to the Equation 2.22. However, other parameters need to be considered as well

to design an efficient photodiode. Absorption coefficient is determined by finding the lattice match growth, optical absorption and energy band gap, mobility, absorption coefficient.

$$E_g = \frac{hc}{\lambda}, \tag{2.22}$$

where E_g is the material band gap, h is the Planck constant, c is the speed of light and λ is the wavelength. The absorption coefficient of each material can be calculated theoretically by calculating the transition rate of electrons from valence band to conduction band using Fermi's Golden Rule and calculate the rate for the occupancy of the valence and conduction bands. The theoretical calculation of the absorption coefficient is beyond the focus of this thesis. Instead, measurement of the absorption coefficient of various semiconductors are readily available in the scientific literature [83]. Absorption coefficient is a function of wavelength (or energy) and temperature, therefore, a material with high absorption coefficient within the wavelength range of interest should be selected.

Table 2.1: Critical material parameters of some semiconductors considered for avalanche photodiodes in this study: Energy band gap, intrinsic carrier concentration, electron and hole mobilities, ionization coefficient ratio $k = \alpha/\beta$ (or $k = \beta/\alpha$), saturation velocity [84, 85, 73].

Material	$\mathbf{E_g}$ **300K**	$\mathbf{n_i}$ $(\mathbf{cm^{-3}})$	$\boldsymbol{\mu_e}(\frac{\boldsymbol{cm^2}}{\boldsymbol{V.s}})$	$\boldsymbol{\mu_h}(\frac{\boldsymbol{cm^2}}{\boldsymbol{V.s}})$	$\boldsymbol{k}$	$\boldsymbol{v_{sat}}(\frac{\boldsymbol{cm}}{\boldsymbol{s}})$
InP	1.344	1.3x10^7	5400	200	0.4-0.5	0.67x10^7
GaAs	1.424	2.1x10^6	8000	9400	-	0.72x10^7
GaSb	0.726	1.5x10^{12}	3000	1000	-	-
$In_{0.53}Ga_{0.47}As$	0.74	6.3x10^{11}	10000	300	-	0.75x10^7
$In_{0.52}Al_{0.48}As$	1.48	1.3x10^7	5400	200	0.29-0.5	0.35x10^7
Si	1.12	1.5x10^{10}	5400	200	-	1x10^7
Ge	0.66	2x10^{13}	3900	1900	-	0.6x10^7

Successful fabrication of optoelectronic devices requires single crystalline and defect free epitaxial layers. This is possible using high end systems such as molecular beam epitaxy (MBE), metal-organic chemical vapor deposition (MOCVD) and liquid phase epitaxy (LPE). Even though each system uses a different phase of the material to grow, all can successfully grow single crystal films. In each process, a substrate is needed to supply a platform for the thin films to grow in a preferable crystal structure. Therefore, the substrate has to have the same lattice constant to avoid dislocations at the interface. There

are only a few available wafers as the substrate for the growth, the lattice constant of the material to be grown has to match the lattice of the substrate to avoid crystal defects such as dislocations and dangling bonds at the interface. For the designer, Figure 2.6 is very useful to select the right material. Lattice constant of the stack has to match to avoid stress in the film which changes the semiconductor parameters, also to avoid trap centers forming due to the stacking faults, etc.

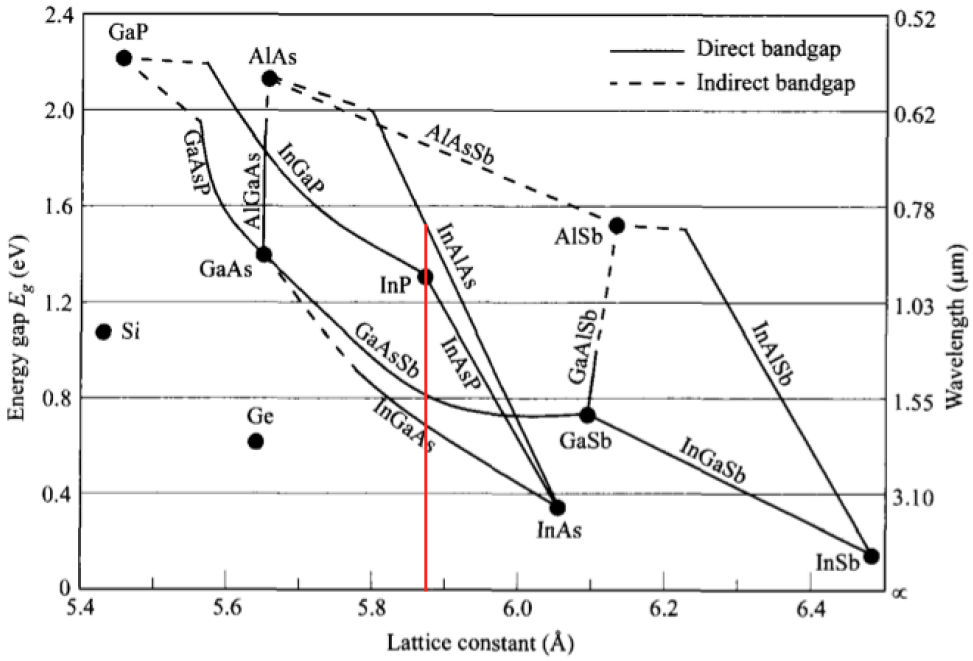


Figure 2.6: Energy gaps and lattice constants of commonly used III-V semiconductors. The calculated energy band gap of typical semiconductors and their corresponding lattice constants at room temperature. The left vertical axis shows the corresponding wavelength based on Equation 2.22. The figure is taken from reference [64].

Aside from the optical properties of the semiconductor, electrical properties such as mobility, critical breakdown field, dielectric constant and intrinsic carrier concentration etc. constitute a big role in determining the right semiconductor. Please refer to Table 2.1 some of the materials considered for this work. In this work, InGaAs is chosen for the active material. InAlAs is chosen for the multiplication layer for separate absorption, charge and multiplication layer architecture. InGaAs is the best material to work in NIR considering the excellent electron mobility and high absorption coefficient among other candidates that displayed in Table 2.1. InAlAs is another promising material that has a

better k value than InP and has a slightly wider band gap. It can be grown lattice matched to InGaAs. In addition, MBE system in ou laboratory has an expertise with arsenides than phosphides, therefore, InAlAs was picked.

2.3 Nanowire p-i-n diode design

The design of the diode structure for nanowire arrays follows a similar approach to designing planar/mesa photodiodes. There should be a thick intrinsic region enough to absorb and collect majority of incoming light, the buffer regions should be thin to limit light absorption and diffusion of minority carriers into the depletion region. The twist in the nanowire design procedure hinges on the feedback from FDTD simulations showing where the absorption locally focuses inside the bulk of the nanowire. Unlike planar/bulk structures, photons are forward scattered and coupled into the nanowire cores with the help of nanowire arrays (Detailed discussion can be found in Chapter 3). The depletion region must fully overlap the localized position of the optical beam so that maximum detection efficiency can be attained with much thinner intrinsic region. Therefore, maximum absorption can be achieved without trading off the bandwidth and transit delay.

2.3.1 Optical design considerations

Detailed analysis of how light interacts with InGaAs nanowire arrays and how to design near-unity absorbers is discussed in Chapter 3. Firstly, nanowires benefit from a truncated cone structure which minimizes the optical reflections from the air-semiconductor interface [86]. When the truncated cone shaped nanowires are present, the effective refractive index increases gradually as the light traverse from air into the nanowire as opposed to having a barrier of refractive index difference. The gradual change of the effective refractive index eliminates the light reflecting from the surface and couples into the nanowire with minimal reflection. Moreover, using a nanocone structure assures the incoming optical mode to couple into the localized radial resonant modes [54], where multiple frequencies can be absorbed given the continuum of the diameters increasing from the top to the bottom. This is not possible with uniform diameter nanowire arrays, since the discrete nature of the resonant modes can lead to a narrow wavelength range near the resonance [87]. Secondly, the nanowire length and the pitch should be optimal. The nanowire density should be sparse enough to ensure that the radial waveguide modes exist in the nanowires. However, the pitch cannot be too large, as the light cannot interact with the adjacent nanowires, therefore, absorption diminishes. Therefore, the pitch value should be chosen such that the

light interacts with the nanostructure. Thirdly, an optimal value for the nanowire length needs be found. If the nanowire is too tall, it will increase the chance to absorb more photons, but this will degrade the temporal response because the photogenerated carriers should travel long distances before reaching to the electrical contacts. Conversely, if the nanowire is too short, there is a danger of increased reflection or transmission of the light through the nanowire without getting absorbed.

The parameters of the nanowire array such as nanowire diameter, taper angle and pitch are not fully independent. Therefore, optimizing the nanowire geometry requires multiple simulations. Simulations were focused on obtaining the highest absorption around 900 nm, 1300 nm and 1550 nm which are used as the optical telecommunication bands. The InGaAs tapered nanowire arrays were able to achieve more than 97% of the light within a nanowire height of 1.5 μm with top diameter of 350 nm, 900 nm pitch and 6^o taper angle. The simulations revealed that the cylindrical nanowire arrays can achieve near unity absorption, but over a narrow band while the tapered nanowires can achieve an absorption value close to unity over a broader wavelength range which is discussed in Chapter 3.

The simulation results also showed that the higher absorption is observed by increasing the nanowire thickness since the longer wavelengths are absorbed deeper in the nanowire. However, the nanowire thickness is inversely proportional to the high speed operation. Hence, we selected a nanowire length around 1.5 μm to operate in an optimal regime. With the optimal parameters from the simulation results, the absorption spectra is significantly improved by carefully designing the parameters of the nanowire array compared to the planar structure. The nanowire array outperforms the slab device even though it contains less volume of material.

The optical absorption of the resulting absorption is given in the Figure 2.7. The optical mode inside the nanowire shows that the dominating mechanism is the leaky radial modes [54, 88]. The majority of the intensity of the optical mode is concentrated in the top half of the nanowire and there are other modes which resonate at different altitude. The longer wavelengths are absorbed deeper into the nanowires, so the p-n junction should be placed such that the highest detection efficiency and lowest timing jitter is obtained. Since the majority of the incoming light is concentrated at the top and contained in a small volume, timing jitter performance is likely to improve.

2.3.2 Electrical design considerations

Design of the electrical structure is done through adjusting the doping level and thickness of each layer in the layer stack. The aim is to attain a maximum photon detection efficiency

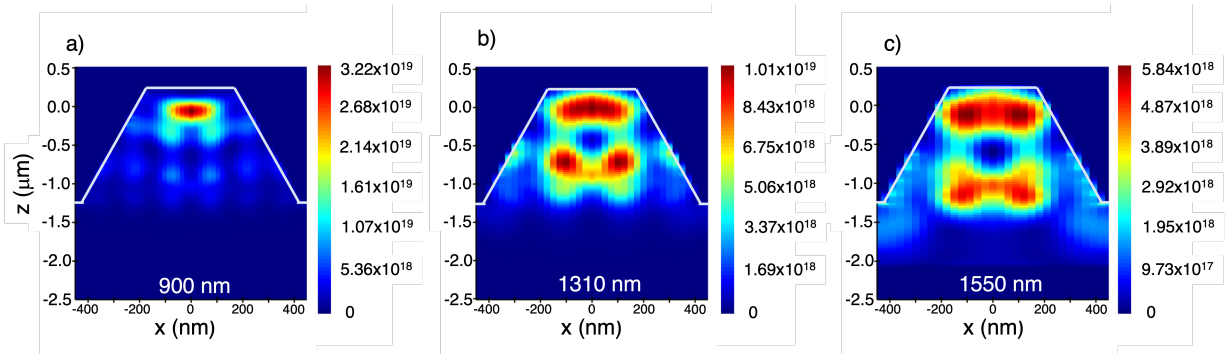


Figure 2.7: Simulated cross-sectional absorption profile in an InGaAs nanowire array. FDTD absorption simulations of a 1.5 μm long InGaAs nanowire array showing the optical absorption inside an individual nanowire when illuminated with wavelengths of a) 900 nm, b) 1310 nm and c) 1550 nm, respectively. The color bar shows the number of carriers generated per m^3. The top nanowire diameter is 400 nm with a 6^o nanowire taper angle and 900 nm separation between nanowires.

(external quantum efficiency) with minimal timing jitter and low noise (low dark current, low excess noise, low dark counts and minimal afterpulsing). It is also important to consider the growth limitations since the background doping can change the effective doping density of the layers. The optical mode profile inside the nanowire shows that the photons at different wavelengths are absorbed within the 1.5 μm thickness of the nanowire. In addition, the majority of the incoming light is focused in the top 300-400 nm of the nanowires. Therefore, the p+ to i (π region) junction should be placed such that the intrinsic region encapsulates the optical modes as much as possible. Moreover, the intrinsic region thickness should be as long as the longest wavelength optical mode spreads verically, therefore, the transit time of the carriers can be minimized for fast detection. Target absorption efficiency can be attained with much thinner material further contributing to a fast transit time.

Nanowire arrays offer other advantages such as reduced device capacitance for high bandwidth operation due to reduced active area of the devices and reduced fill factor (less device volume). Since capacitance is idirectly proportional to the device active area, the nanowire devices have lower capacitance compared to same area planar device. Similarly, reduced area will proportionally reduce the junction current that can increase the detectivity of the detectors. However, increased total surface area in nanowire arrays could give a rise to high leakage current due to the fact that the nanowire surface may lead to higher surface generation current. There are strategies to limit surface generation and reduce surface recombination velocity with proper surface passivation [89].

The p-i-n diode structure in this study starts with a heavily n doped (10^{18} cm^{-3}) InP substrate. As a start, 200 nm of InGaAs with the same doping density is deposited by molecular beam epitaxy (MBE) system as a n buffer layer which also forms a seed layer for the subsequent layers. Then, a 2000 nm (1600 nm) thick lightly doped InGaAs region is grown to form the intrinsic region. The thickness is selected in order to accommodate different nanowire heights depending on the location of the absorption with respect to incident wavelength. In order to avoid unintentional doping, the intrinsic layer is lightly doped with 5×10^{15} cm^{-3} using silicon (Si) atoms. As a p buffer, 300 nm (200 nm) thick heavily p doped region is then grown with a carrier concentration of 10^{18} cm^{-3}. Beryllium (Be) is used to create the p type doping. Finally, 50 nm (30 nm) thin p++ layer is formed with a concentration of 10^{19} cm^{-3} at the top of the structure to help with low contact resistance for the top electrode. The buffer layers help to deplete the lightly doped region (π region) sandwiched between n+ and p+ regions even when there is no bias. This diode structure is a p-i-n diode, where the intrinsic length is fully depleted due to the highly doped p and n regions under reverse bias. The p and n buffer regions are chosen to be much shorter than the length of the intrinsic region since the depletion layer forms mostly in the lowly doped part. Besides, the thin p and n regions help to reduce the rate of recombination in the quasi-neutral regions then the diffusion of carriers into the depletion region. For nanowire array photodiodes, a shorter top buffer layer is desired since a shorter buffer increased the efficiency of InP nanowire array solar cells [35]. Unlike commercial diodes which contain InGaAs sandwiched between InP buffer layers to limit surface generation and diffusion current [90, 91, 92], our structure is fully made out of InGaAs to avoid heterointerfaces and ease of fabrication. The InGaAs electrical layer stack and corresponding band diagram based on Silvaco TCAD simulation are illustrated in Figure 2.8.

2.3.3 Avalanche photodiode based on p-i-n structure

To create avalanche multiplication, p-i-n photodiodes will have to be operated with higher bias than usual to promote avalanche multiplication. Once the breakdown field is reached, then the photogenerated carriers can multiply by means of impact ionization. The intrinsic region will serve as not only the absorption region but also multiplication region. The photogenerated electrons and holes will immediately see the high electric field and will accelerate towards to opposite sides of the junction. If the absorption takes place close to the p-i (i-n) junction, holes (electrons) will not find enough distance to gain sufficient energy to multiply. In this case, the electrons (holes) will trigger the self-sustaining avalanche.

As previously discussed, the nanowire structure reduces the fill factor of the device

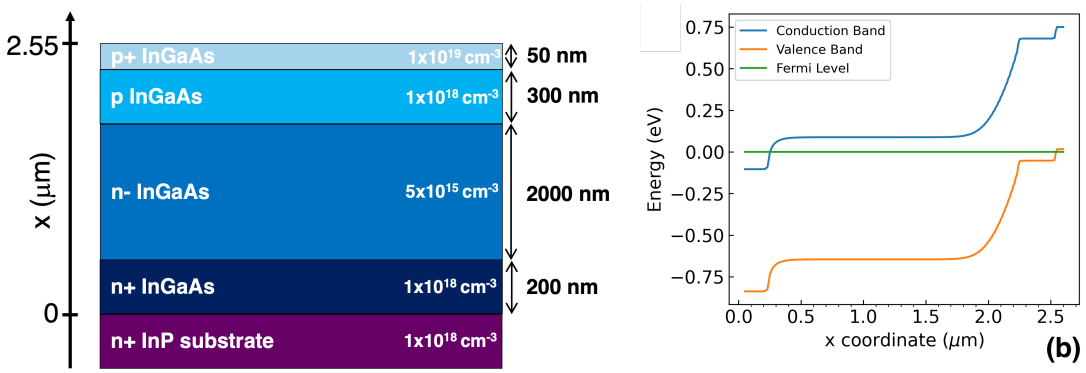


Figure 2.8: Designed InGaAs photodiode structure. a) The layer stack and doping concentrations of the InGaAs p-i-n photodiode and thicknesses of the designed InGaAs device. b) The corresponding energy band diagram of the designed layer stack shown in a).

and consequently, there are less number of mobile carriers inside the junction. Having a low fill factor also shrinks the active device volume which reduces the probability of dark counts since the total number of defects is significantly reduced [62]. This means that the afterpulses due to the bulk defects are expected to lessen greatly. There is less chance for carriers to be trapped by the existing trap levels, so less number of afterpulses is expected rooted from bulk defects. If the afterpulsing is reduced, then the maximum count rate will improve. Therefore, the nanowire structure can boost the overall performance of the single photon avalanche diodes. We have to note that, however, the reduced fill factor also leads to increased surface area, therefore, high surface area could potentially create new trap centers for afterpulses. Proper surface passivation is critical in order to limit afterpulses arising from surface traps.

A meticulous consideration must be given to the electron and hole ionization coefficients for p-i-n avalanche photodiodes. Electrons and holes have different probabilities to initiate an impact ionization event. For InP, for instance, holes have a higher probability of impact ionizing than electrons. In contrast, for InGaAs and InAlAs, holes are less likely to impact ionize than electrons, i.e., holes have a lower ionization coefficient than electrons. Depending on the value of k ($k = \alpha/\beta$ or $k = \beta/\alpha$), avalanche operation should be initiated with the more likely carrier type to maximize the chance to reach self-sustaining avalanche. Ideally, if both types have the same ionization coefficients, the device could generate a higher avalanche gain as well as low excess noise then a device with asymmetric ionization coefficients for electrons and holes. In most cases, though, due to variance in impact ionization coefficients of holes and electrons, devices exhibit high noise (poor timing jitter and high excess noise). This trade-off between gain and noise can be mitigated by

using a nanowire geometry [36]. If we design the stack layer such that the carrier type with the higher ionization coefficient to have a larger space available to create a self-sustaining avalanche, we can achieve high gain along with low timing jitter and low excess noise. For instance, we can set the top part of InP diode as n-type. Therefore, photogenerated holes (higher ionization coefficient) will move downwards where the trajectory is long enough to create a self-sustaining avalanche. The photogenerated electrons, on the other hand, cannot participate in a significant multiplication due to a limited space up to the top contact. This will ensure the timing jitter is not significantly affected by those electrons.

The collection efficiency benefits from fully depleted nanowire core which is dominantly the intrinsic region. A fully depleted nanowire core increases the probability of absorption of photons, lowers the device capacitance and provides enough space that leads to a self-sustaining avalanche. In avalanche mode for single photon detection (Geiger mode), the reverse bias is above the breakdown voltage, and the depletion length is much wider than the zero bias width. Therefore, the length of the lightly doped region needs to be optimized for the trade-off between gain and temporal response. In principle, an avalanche path larger than 0.5 μm is needed to create a self-sustaining avalanche in planar InP/InGaAs SPADs [93]. Nanowires are confined radially (not should be confused with quantum confinement even though when diameters are small enough they also experience quantum confinement) due to their 1D-like nature; hence, a longer distance may be required to allocate enough volume so that the diffusion assisted avalanche spreading can expand to create a macroscopic current [94].

2.3.4 Surface states of nanowires

Nanowires are high surface to volume ratio structures. As a result, high surface area can have a big impact on device operation. For InP, this effect is more pronounced as Fermi pinning can even change the majority carrier type at the surface. For a bulk device, this effect can be negligible, nonetheless, the radial band bending should be calculated for the nanowires devices. To investigate the radial band bending due to Fermi pinning, we performed analytical simulations and identified that the depletion region extends the entire diameter of the nanowires, thus, potentially leading to a reduced dark current. We simulated the nanowire core depletion of cylindrical p-InP structure caused by the surface states by solving the Poisson's equation in cylindrical coordinates [95]. According to the simulations, the p-InP nanowires have a critical nanowire diameter of 344 nm when the carrier concentrations of the actual device (array of InP nanowires with a top diameter of 150 nm and a bottom diameter of 350 nm [36]) is used as in Figure 2.9a. InP nanowires with a smaller diameter than 344 nm would have a fully depleted core due to strong radial band

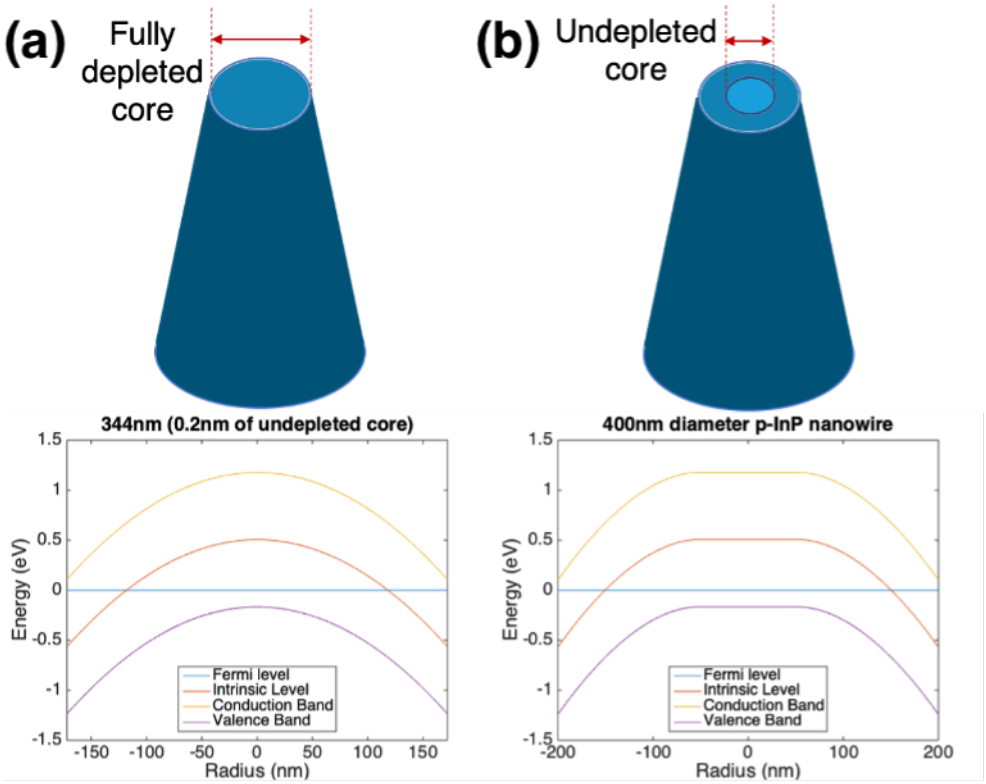


Figure 2.9: Simulated band bending due to the nanowire surface states. The energy band diagram of the cross section for the simulated InGaAs nanowire with diameters a) 344 nm and b) 400 nm. Fully depleted core in a) and partially depleted core in b) are illustrated. The surface band bending depletes the core fully when the InP nanowire diameter is smaller than 344 nm.

bending. Thus, the simulation result is in agreement with the prediction of a fully depleted nanowire core, which reduces the device dark current. We also included a simulation result of a p-InP nanowire with a diameter of 400 nm, which is greater than the critical diameter. Here, the nanowire is not fully depleted as illustrated by the presence of the 106 nm long quasi-neutral region at the core as shown in Figure 2.9b.

2.4 SACM avalanche diode design for nanowire arrays

The motivation behind using a separate absorption, charge and multiplication (SACM) configuration is to maintain low electric field intensity ($< 1.5 \times 10^5$ V/cm) in the absorption region to suppress dark current due to band-to-band tunneling and to use a wide band gap material to achieve high gain [96, 93, 97, 98, 99]. The same approach can be applied to nanowire arrays to achieve high gain with low dark current and high detection efficiency. This approach could be a gateway to the next generation of single photon avalanche diodes.

To operate at telecom wavelength bands (1300 nm and 1550 nm) InGaAs offers the best electrical and optical performance combination among other candidates. InGaAs has a narrow band gap of 0.75 eV with high absorption coefficient (See Table 2.1), has high electron mobility and reach to a high electron saturation velocity. Moreover, $In_{0.53}Ga_{0.47}As$ can be grown epitaxially on InP wafers without lattice mismatch. These material properties make InGaAs the front runner material candidate for NIR and SWIR photodiodes. Once InGaAs is picked as the absorption material, we have to consider a few angles for a successful design. Firstly, we determine the nanowire absorption layer parameters using InGaAs which include nanowire height and doping density. Typical values of InGaAs thickness in SPAD devices vary between 0.5 to 3 μm for the absorption region [93]. The thickness value is determined based on the quantum efficiency requirement of the application. In our study, we aim to maximize the optical absorption of 1310 and 1550 nm bands. Based on our optical absorption simulations (see Figure 2.7), the target wavelengths of 1310 nm and 1550 nm are absorbed within the first 1.5 μm height of InGaAs nanowires; therefore, there is no need to make the InGaAs layer thicker than 1.5 μm. A longer thickness would only provide marginal improvement of the quantum efficiency in exchange for undesirably high timing resolution and long transit times. With the help of enhanced absorption properties of nanowire arrays, a shorter absorption region can be used. Secondly, we believe that the timing jitter of photodiodes would significantly benefit from narrowly focused absorption location, reducing the spread in carrier travel times. Furthermore, a short InGaAs thickness as well as the reduced fill factor (the total volume of active material) of InGaAs thanks to the nanowire geometry can lower the thermal recombination-generation limiting the dark counts (dark count rate for single photon avalanche photodiodes) [93, 62]. Thirdly, the electric field in the InGaAs absorption region should be kept below $< 1.5 \times 10^5$ V/cm at all times, above which a significant field assisted tunneling current is present in InGaAs [67]. The device cannot operate efficiently at zero field in the absorption region since carriers will fail to reach to the multiplication layer. Small field will help with carrier drift, however, short transit times and efficient carrier transit requires high electric fields where the carriers move with saturation velocity. Therefore, the electric field value has

to optimized for operation bias. Moreover, the doping density should be below 5 $\times 10^1 5$, which ensures high mobility and keeps the probability of tunnneling low.

The multiplication region needs to function properly under high electric field with limited tunneling current and high gain. Firstly, the material has to have a wide band gap to ensure avalanche breakdown onset is earlier than band-to-band tunneling resulting in Zener breakdown. Simulated band-to-band tunneling current for InGaAs and InAlAs in Figure 2.5 shows the critical electric field intensities for consideration. The epitaxy should be devoid of crystal defects in the bulk and at the heterointerface to limit trap-assisted tunneling. Threading dislocations, high impurity density or other crystal defects could cause trap assisted thermal generation, or worse, trap assisted tunneling at high fields deteriorating device operation. Secondly, a high carrier saturation velocity is desired to support high speed detection. For that purpose, the material has to have high electron mobilities and high saturation velocity. Furthermore, the anode and cathode orientation should be carefully designed such that the carrier type with higher breakdown probability should initiate the avalanche breakdown. For instance, anode (p side) of the diode should be at the top if electrons are more likely to impact ionize since electrons will be drifted to the cathode (n side) side. Multiplication layer thickness presents another trade-off between timing resolution and multiplication gain. A thicker multiplication region results in higher thermal generation due to increased volume and worse temporal resolution but tunneling current would decrease as the self-sustaining avalanche can start at lower fields lowering the dark count rate [93]. Moreover, multiplication region thickness also determines the breakdown voltage, a long multiplication region will result in high breakdown voltages which may be not practically helpful. Additionally, thermal generation can be suppressed with low temperature operation but afterpulsing would be more pronounced below certain temperatures, therefore, optimal operating temperature needs to be determined at the design stage.

Two candidates for multiplication region that could work with InGaAs are $In_{0.52}Al_{0.48}As$ (hereafter InAlAs) and InP, both can be epitaxially grown without lattice mismatch on readily available InP wafers. InP is a commonly used material in SPAD technology and has been under intensive research over the years. Nonetheless, InAlAs is an alternative to InP, since recent research showed InAlAs has higher breakdown probability with increased overbias and lower dark count probability than InP, although InP can achieve a better timing jitter [100]. InAlAs has wider band gap than InP and has lower intrinsic carrier concentration; InAlAs will suffer less from diffusion of thermally generated carriers entering into the high field zone. In linear APDs, multiplication excess noise is suppressed with shorter multiplication layer thickness; InAlAs having lower k values than InP for equal thicknesses yield lower noise [73]. In addition, the surface recombination generation (r-g)

scales exponentially with the energy band height [70], so surface r-g current is expected to be less in InAlAs than InP. Furthermore, InAlAs exhibits smaller thermal coefficient of breakdown voltage allowing to use the detector at lower temperatures to minimize thermally generated dark current [101]. For all things considered, InAlAs is a clear material of choice.

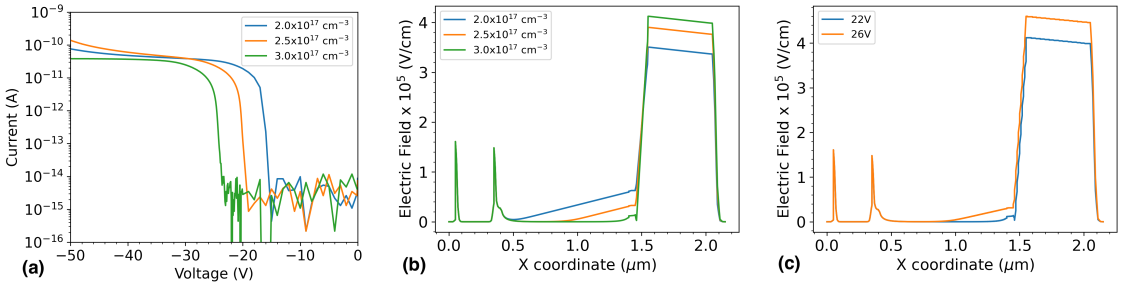


Figure 2.10: Reverse bias current and electric field profile simulations of separate absorption, charge, and multiplication layers of an avalanche photodiode for different charge layer doping densities and punch-through voltages. a) Simulated diode current for different charge layer doping densities demonstrating the shift in punch-through voltage. b) Corresponding electric field profiles of the varying doping densities in a). c) Simulation of electric field at -22 V and -26 V showing the onset of punch-through in the InGaAs absorption layer.

Field control layer plays a key role in avalanche photodiodes. It regulates the electric field between absorption layer and multiplication layer, therefore, determines the punch-through voltage, breakdown voltage and band-to-band tunneling current in InGaAs. To ensure low dark count rate and high detection efficiency, optimization of the charge layer is needed. For that purpose, device current of a device with different doping concentrations for a 100 nm thick charge layer were simulated to demonstrate the electric profile change. Figure 2.10a shows the effect of doping concentration on the punch-through voltage. As the doping density of charge layer increases, the punch-through voltage shifts to the higher voltages. The shift indicates the reduced electric field in the InGaAs absorption layer and increased electric field at the InAlAs multiplication layer at the same applied voltage(Figure 2.10b). This shift also points out to a reduced breakdown voltage since the electric field intensity will be higher for a given voltage with a higher charge layer doping concentration. If not designed carefully, this may lead to under depletion of the absorption layer leading to a poor quantum efficiency. On the other hand, a low value of charge layer will increase the electric field intensity in the InGaAs, the punch-through will be reached at a smaller voltage. In that case, possibly of giving rise to significant band-to-band tunneling increases.

Figure 2.10c displays the onset of punch-through voltage which is around -22V. The electric field intensity in InAlAs is still below the critical breakdown field since the current does not show breakdown characteristics but the InGaAs region has started to be depleted. The ideal design should aim for a fully depleted InGaAs absorption region with a field intensity enough to create saturation velocity for electrons but low enough to ensure the tunneling current is negligible when the InAlAs has electric field above the critical breakdown field.

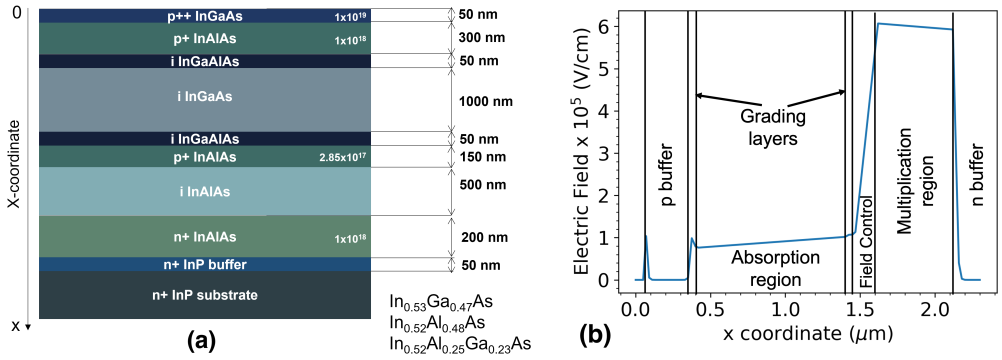


Figure 2.11: Designed avalanche photodiode parameters and the corresponding electric field profile at the breakdown voltage of -44V. a) Designed layer stack of separate absorption, charge and multiplication regions device employing InGaAs as the absorption region material and InAlAs as the multiplication and charge layer materials. b) The corresponding electric field profile of the stack layer displayed in a).

The designed device structure again starts with a heavily n doped InP wafer (1×10^{18} cm^{-3}). 50 nm seed layer of n+ InP and 200 nm n+ contact InAlAs layer were subsequently grown with the same doping density. A 500 nm of unintentionally doped InAlAs was added for multiplication layer, followed by a p doped 150 nm field control layer with a doping density of 2.85×10^{17} cm^{-3}. Next, a 50 nm grading layer of InAlGaAs, which is the interpolation of InGaAs and InAlAs was deposited. A 1000 nm of unintentionally doped InGaAs absorption layer and a second InAlGaAs grading layer of 50 nm were grown. Finally, a heavily p doped (1×10^{18} cm^{-3}) InAlAs buffer layer and 50 nm of InGaAs p+ contact layer (1×10^{19} cm^{-3}) were formed. Similar to the previous growth, Be and Si were used as p and n type dopants, respectively. A number of growth processes were performed to reach the desired specifications in terms of surface morphology and crystal quality. The growth study was initially done at University of Waterloo MBE laboratory and then the final device were fabricated from the thin films grown by Intelliepi Epitaxy Technology Inc. located at Richardson, Texas, USA.

2.5 Experimental methods and optical characterization setups

2.5.1 Dark current-voltage characteristics

To characterize the InGaAs based p-i-n and avalanche diodes, I performed a dark current voltage measurement at various temperatures. This measurement not only tells about the electrical characteristics, but also proves the existence of the avalanche breakdown as opposed to the Zener breakdown.

The avalanche multiplication is known to exhibit a positive temperature coefficient. At higher temperatures, hot carriers (highly energetic) passing through the depletion region loses more energy to the phonons by the collisions and the scattering which results in a smaller ionization rate. Therefore, there should be higher electric field to overcome the small ionization rate. As a result, the breakdown voltage increases by increasing the temperature of the device. Conversely, the Zener breakdown (tunneling) happens when there is a thin energy barrier. In that case, the carriers can make band-to-band tunnelling which results in a high current before the depletion region reaching to avalanche breakdown field. The breakdown voltages less than $\frac{4E_g}{q}$ are referred to the existence of the tunneling, where, the voltages in the excess of $\frac{6E_g}{q}$ are identified by the avalanche breakdown [64]. Since the energy band gap decreases by increasing the temperature, the breakdown voltages due to the tunneling are getting smaller, so we observe a negative temperature coefficient $V_{BR} \propto \frac{1}{E_g}$.

The results of the dark current-voltage measurements at different temperatures can be seen in Figure 5.3. There are two regions which shows the two different properties of the device characteristics. In the region 1, where it corresponds to the voltages up to 10 V, the dark current values increase with the elevated temperatures. The increase in current can be explained by the increased number of carriers by higher energy at higher temperatures. In the region 2, there is a shift towards the higher current with decreasing the temperature, since the avalanche breakdown happens at smaller voltages when the temperature is lower. According to the curve, we can say that the device has a positive thermal coefficient. It is also a signature of the avalanche breakdown as opposed to the Zener breakdown in which the breakdown voltages shift to the lower voltages by increasing the temperatures.

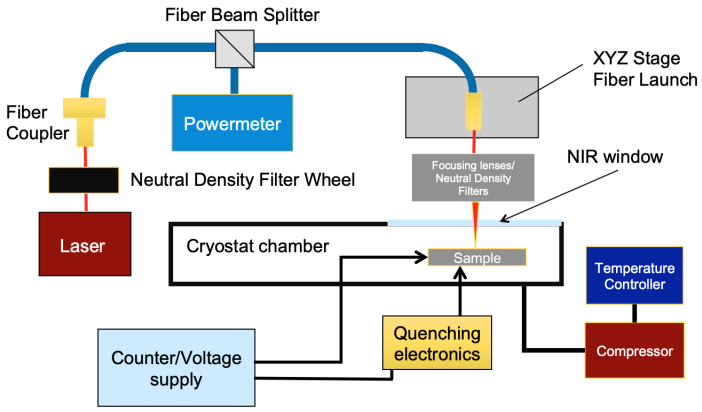


Figure 2.12: The optical characterization setup used to measure the single photon detection characteristics of the fabricated nanowire array avalanche photodiodes. The laser pulses are attenuated down to single photon per pulse and focused on the device active area. The signal is collected by the quenching electronics. The sample is cooled

2.5.2 Optical setups for characterization

The measurement setup for single photon detection measurements is shown in Figure 2.12. This system can characterize the metrics such as photon detection efficiency, dark count rate, alterpulsing, maximum count rate and spectral range. The laser is used as the single photon excitation source. Before shone onto the device active area, the intensity is reduced through a set of neutral density filters. This ensures that each laser pulse is attenuated down to a single photon per pulse level. The intensity of the laser is monitored continuously. The devices under test are placed in a cryostat chamber in order to test the devices at different ambient temperatures. The devices are connected to a quenching circuit and a counter module in order to count the photon pulses and dark pulses.

The timing jitter is measured using a measurement different system. Similar to the setup above, there is an incoming pulsed laser focused onto the device. We use high resolution timing electronics to measure the time delay between the time when the photon hits the device and the time when the output signal is detected. Then, a histogram is obtained from the measurements of multiple cycles which gives the timing jitter of the detector.

We use a passive quenching resistor to detect the single photons. This resistor is connected to the photodiode in series. The avalanche photodetector is kept at a voltage above the avalanche breakdown. When a photon is absorbed and converted into a macroscopic

current by the avalanche multiplication process (the trigger), the current passing through the device increases significantly. The voltage on the resistor increases as well, which is governed by the Ohm's Law. The resulting signal is detected by a comparator circuit and the photon count is registered. Since the applied voltage is constant, the voltage on the photodetector starts to decrease and drops below the threshold value (breakdown voltage) as a result of the voltage division by the resistor. Therefore, the resistor quenches the voltage on the photodetector and brings the photodetector into its initial state. The photodetector can detect another photon after quenching when the voltage comes to the initial level. The timing of the process depends on the electrical properties of the photodetector and the quenching resistor (quenching resistance, junction capacitance, parasitic capacitance etc.).

The active quenching circuits are designed to cancel the large transient signals by a complex circuitry and they quench the single photon avalanche diode for a certain period of time [62]. However, these detectors cannot register another photon within the time interval, which limits the photon count rate. We want to use the so-called "free running mode" which is ideal for a system when the photon arrival time is unknown. The nanowire based devices show a great promise to reduce the noise mechanisms (namely afterpulsing which limits the photon count rate) by using the low fill factor nanowire structure, thus eliminating the need for an active quenching circuit [62].

Chapter 3

Near-unity absorptance nanowire arrays

Chapter contributions: Brad van Kasteren provided the initial design of the nanowire metamaterial through numerical calculations. Sasan V. Grayli performed FDTD optical simulations. Daozhi Shen helped with the FTIR measurements. Man C. Tam and Zbigniew Wasileski provided the MBE grown InGaAs wafers. Dayan Ban provided scientific support. Adan W. Tsen provided the FTIR experimental setup. Michael E. Reimer supervised the project.

This chapter is adapted from the publication:

Tekcan, B., van Kasteren, B., Grayli, S.V., Shen, D. Tam, M.C., Ban, D., Wasilewski, Z., Tsen, A.W., and Reimer, M.E. (2022). Semiconductor nanowire metamaterial for broadband near-unity absorption. *Scientific Reports*, 12, 9663.

3.1 Nanowires for near-unity absorption

Photonic metamaterials is a promising field of study owing to the unorthodox interaction and manipulation of light by a specific arrangement of subwavelength sized structures, namely, metaatoms [102, 103, 104, 105, 106, 107, 108]. A metaatom is the smallest repeatable structure, a unit cell of a metamaterial; it produces a unique response to optical excitation when placed in an array with special arrangement. Therefore, the cumulative response of metaatoms exhibits different characteristics than the individual units. To take advantage of those capabilities, metamaterials have been extensively scrutinized recently;

interesting demonstrations emerged such as super-lenses, negative refraction, asymmetric transmission, and cloaking [102, 103, 104, 105, 106, 107, 108, 109, 110, 111]. Initially, metamaterials were shown to exploit collective oscillations of electrons in metals as in surface plasmons, where electromagnetic oscillation of light couples into a metal structure by creating electron dipoles leading to light absorption [102, 103, 111, 112, 113]. In addition, the desired response from the dipoles was controlled with the size, shape, and orientation of plasmonic structures, enabling the use of plasmonics for different requirements [111, 112, 113, 114, 115]. However, the obtained enhancement was not useful due to the high loss caused by the high-rate conversion of light into heat. Dielectric metamaterials, on the other hand, could overcome the high loss using highly absorptive or high transparent semiconductors [102, 103, 116, 117, 118, 119]. The ability to create highly absorbing or highly transmitting materials by controlling the electromagnetic field was highly sought after for many exikillsting technologies such as sensing and imaging applications [88, 104, 106, 109, 110, 116, 120, 121, 122, 123].

Examples of near-unity absorption with metamaterials have been previously demonstrated using nanowires and Mie resonators, nonetheless, the near-unity absorption is limited to a narrow wavelength range in the reported studies [110, 124, 125]. In this study, we design a new metamaterial structure using InGaAs nanowire arrays by carefully designing the geometry of individual wires and wire separation (lattice constant). The designed InGaAs metamaterials exhibited a near-unity absorption over an unprecedented wide wavelength range from 400 nm to 1650 nm, averaging 92% absorptance. After the nanowire arrays were fabricated having high resemblance to the designed structure, FTIR measurements yielded an average absorptance of 93% from 900 nm to 1500 nm, while the simulations estimated an average absorption efficiency of 97% . The comparison of the absorption efficiency between the InGaAs nanowire array and a thin InGaAs film with the same thickness as the nanowire array showed a 2-fold enhancement. The designed and fabricated InGaAs nanowire arrays show great potential of enhancing the existing technologies where near-unity absorptance is crucial. The result can be of particular interest in quantum detection systems for quantum key distribution or satellite communication and in health applications such as dose monitoring for cancer treatment and optical coherence tomography for eye imaging to diagnose potentially blinding diseases.

3.2 Enhanced absorption by nanowire arrays

Near-unity absorption with cylindrical nanowires have been studied extensively; however, the function of the spacing between nanowires was not properly investigated [53, 54, 126].

In this study, the role of periodicity on the absorption profile was investigated to design a broadband near-unity absorber. The light absorption in nanowire arrays is governed by two separate mechanisms that work collaboratively leading to enhanced absorption in a wide spectrum as demonstrated in Figure 3.1a. Firstly, incoming light can couple into individual nanowires via leaky guided resonance modes, namely hybrid electric and hybrid magnetic modes (HE_{11} and EH_{11}) [54, 124, 126]. Secondly, light can excite fundamental transverse electric (TE) and transverse magnetic (TM) modes after exiting from a neighboring nanowire. In leaky guided modes, the mode can exit (due to its leaky characteristics) the primary nanowire as light propagates in the direction of the nanowire longitudinal axis similar to light propagation in an optical fiber. The exiting light subsequently interacts with the neighboring nanowire giving rise to TE and TM modes in the secondary nanowires (neighboring nanowires). As a result, a strong interaction between neighboring nanowires enhances the light absorption significantly. Figure 3.1b shows the leaky nature of the guided mode with a FDTD simulation. The direction of the electric field changes as the light wave propagates. In this figure, the diameter of the nanowire was taken as 200 nm and 833 nm separation between nanowires was used. The nanowire height was 1400 nm. Figure 3.1c shows the absorption profile when the nanowire array was illuminated with 1020 nm, exhibiting a leaky guided mode resonance and localized absorption in the nanowire.

Solving Maxwell's equation with cylindrical boundary conditions yields the eigenvalue equation that describes the angle dependence of the supported modes in a cylindrical waveguide [127] also given here as Equation 3.1. For grazing angles of incident light, light couples into the EH and HE modes and the absorption is governed by the leaky guided modes. When the excitation is perpendicular to the cylinder, fundamental TE and TM modes are excited. In nanowires, when the light decouples from the primary nanowire and is directed at the secondary nanowire perpendicular to the nanowire longitudinal axis, it couples into TE and TM modes to enhance the absorption.

$$\left(\frac{1}{k_1^2-k_2^2}\right)^2\left(\frac{\beta m}{a}\right)^2 = k_0^2\left(n^2\frac{J_m'(k_1a)}{k_1J_m(k_1a)} - n_0^2\frac{H_m'(k_2a)}{k_2H_m(k_2a)}\right)\times\left(\frac{J_m'(k_1a)}{k_1J_m(k_1a)} - \frac{H_m'(k_2a)}{k_2H_m(k_2a)}\right), \tag{3.1}$$

where k_1 and k_2 represent the transverse components of the wave vectors (inside and outside of the nanowire, respectively), n and n_0 are the refractive indices (inside and outside of the nanowire, respectively), β and k_0 are wave vectors along the nanowire axis and in free-space, respectively, and J_m and H_m are the m^{th}-order of the Bessel function and the Hankel function of the first kind, respectively. The prime indicates the derivative of these Bessel and Hankel functions. The transverse components in Equation 3.1 are angle dependent,

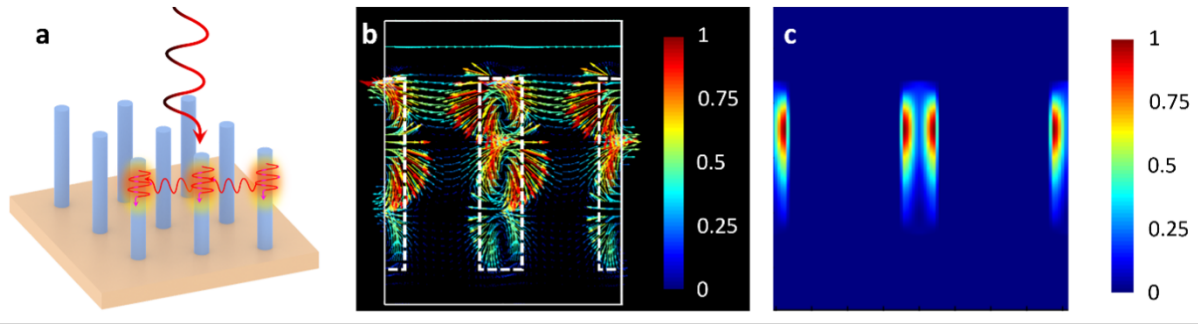


Figure 3.1: Enhanced light absorption with nanowire arrays. a) Graphical representation of enhanced absorption in nanowire arrays. Incoming light couples into leaky guided modes in the nanowires. The coupled mode decouples from the nanowire due to its leaky guided nature, then the decoupled wave is absorbed by the adjacent nanowire by excitation of transverse (TE and TM) modes. b) Simulated electric field vectors inside the nanowires with a periodicity of 833 nm, nanowire diameter of 200 nm and height of 1400 nm. The color bar displays the strength of the electric field normalized to the maximum value. c) Simulated absorption profile of the nanowire array when illuminated with λ=1020 nm (nanowire geometry with the same dimensions as b)). Similarly, the color bar shows the strength of electric field normalized to the maximum value.

where $k_1 = k_0\sqrt{n^2 - cos^2\theta}$, $k_2 = k_0 sin\theta$, and $\beta = k_0 cos\theta$. Thus, changes in the angle of incidence govern which modes are excited in the neighbouring nanowires. There are two main incident angles that we consider, perpendicular ($\theta = 90°$) and parallel ($\theta = 0°$) to the nanowire axis. First, with an incident angle corresponding to the wave vector being perpendicular to the nanowire axis, β becomes 0. This results in the excitation of purely TE or TM leaky resonant modes. Alternatively, deviation of the wave vector angle from 90° results in the excitation of HE and EH leaky guided modes.

3.3 Narrowband absorber

Simulated absorptance of a single InGaAs nanowire as a function of nanowire radius is shown in Figure 3.2a. For nanowire radii smaller than 175 nm, the InGaAs nanowire can only support a single leaky guided resonant mode. With increased nanowire radius, the supported mode shifts to longer wavelengths that is also observed in other studies [126]. Moreover, the absorption profile broadens as the radius is further increased due to the excitation of multiple modes. The absorption response approaches to the bulk absorption

spectrum as the nanowire radius is above 660 nm. However, the wider response of a single nanowire still remains far from high absorption efficiency.

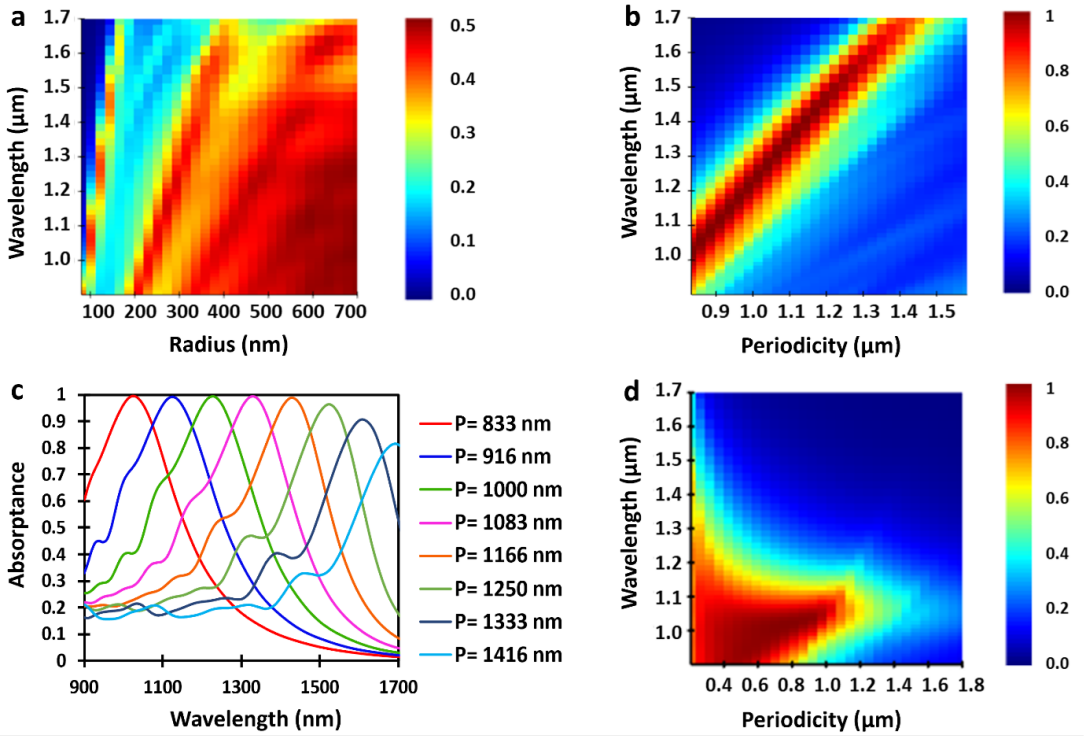


Figure 3.2: Finite-difference time-domain (FDTD) simulations of narrowband near-unity absorptance of 1400 nm tall InGaAs cylindrical nanowire arrays. a) Surface plot of absorptance in cylindrical nanowire arrays with respect to the nanowire radius and excitation wavelength. b) Shift in absorption peak wavelength (resonant wavelength) as a function of periodicity. The nanowire diameter to periodicity ratio is kept as 0.24. c) Absorption spectra of nanowire arrays with varying periodicity while the ratio of the nanowire diameter to periodicity kept as 0.24. d) Surface plot of absorptance for cylindrical nanowire arrays as a function of periodicity with a 200 nm nanowire diameter.

The near-unity absorptance can be achieved by placing the nanowire in an array and finding the optimal separation distance. For that purpose, we have simulated the absorptance of InGaAs nanowire arrays for a range of separation (periodicity) from 800 nm to 1.6 μm as shown in Figure 3.2 b and c. Figure 3.2b shows that the maximum absorption shifts to longer wavelengths with the separation while the nanowire diameter to periodicity ratio is kept constant (0.24). Figure 3.2c shows the absorption spectra of nanowire arrays

with varying periodicity. Each periodicity curve shows clearly that the resonance wavelength shifts with the change in periodicity. The 0.24 ratio gives the narrowest full-width half maximum and the maximum resonance resulting in 99% maximum absorptance. A remarkable wavelength selectivity is achieved by changing the separation distance while keeping the nanowire diameter to separation ratio constant. A small decay in the maximum absorption was observed after 1500 nm, with a high absorptance of 80% at 1650 nm.

To dissect the specific contribution of periodicity for enhanced near-unity absorption, we selected a nanowire diameter of 200 nm and height of 1400 nm, then varied the periodicity. The simulated absorptance were obtained for periodicity values ranging from 0.3 μm to 1.8 μm as shown in Figure 3.2d. Near unity-absorptance (>99%) was observed for separations in the range between 676 nm and 885 nm. High absorption in this range corresponds to enhanced absorption by excitation of TE and TM modes in the adjacent nanowires from decoupling of leaky guided modes in the primary nanowire. In cases where the separation is out of this range; however, the spectral sensitivity degrades and the maximum absorptance value worsens. Smaller nanowire periodicity leads to a broader absorption spectrum, nonetheless, the maximum absorptance gets smaller since the material approaches to bulk InGaAs from the nanowire geometry. On the other hand, narrow absorption spectra were observed for larger periodicity of nanowires, but the maximum values drop since the interaction between neighboring nanowires decreases.

3.4 Route to broadband absorption

While cylindrical nanowire metamaterials offer narrow bandwidth, near-unity absorption capabilities, certain sensing applications require broad spectral range detection. One successful approach with a nanowire metamaterial utilizes tapered nanowire metaatoms to accommodate the coupling of a broad range of frequencies [36, 54, 55, 86, 128]. In this strategy, the nanowire tapering provides a continuum of diameters for all wavelengths to couple to resonant HE and EH leaky guided modes. This broadband behaviour combined with a proper choice of semiconductor material can produce a desirable broadband metamaterial absorber in the infrared.

To design a near-unity broadband absorber in the infrared, we first optimize the tapered InGaAs nanowire shape of a single nanowire by varying the height and bottom radius for a fixed top radius. The top radius was selected (r = 170nm) to coincide with the cylindrical nanowire radius that produced the highest resonant spectral response near the edge of the InGaAs bandgap (1650 nm). The bottom radius of the tapered nanowire was increased

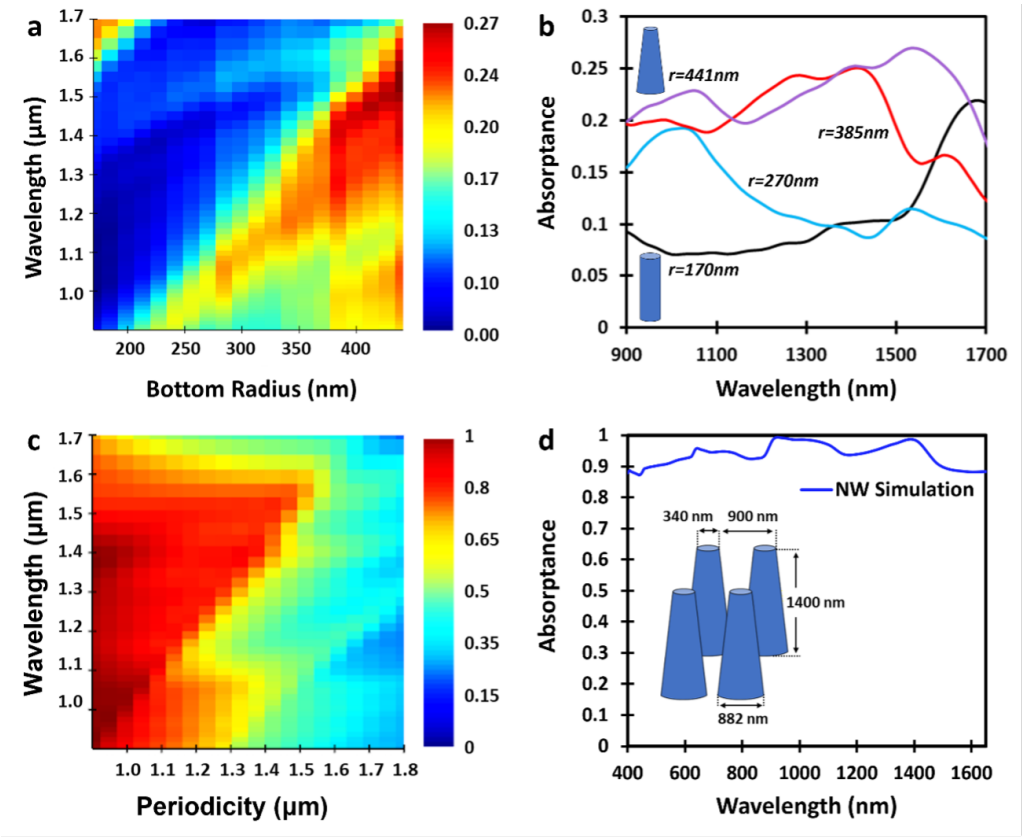


Figure 3.3: Finite-difference time-domain (FDTD) simulations of the broadband absorption efficiency for tapered InGaAs nanowires. (a) Calculated absorption efficiency (color bar) of a single tapered nanowire as a function of bottom nanowire radius with a fixed top radius of 170 nm and height of 1400 nm. (b) Two-dimensional slices of the absorption efficiency from (a) of a single nanowire with varying bottom radius (170 nm, 270 nm, 385 nm, 441 nm) and a fixed top radius of 170 nm. The nanowire is cylindrical at r = 170 nm as indicated by the bottom inset. Increasing the bottom radius leads to a nanowire tapering as indicated by the top inset for r = 441 nm. (c) Calculated absorption efficiency (color bar) dependence on the nanowire periodicity for a nanowire height of 1400 nm, top radius of 170 nm and bottom radius of 441 nm. (d) Calculated absorption efficiency over an extended wavelength range for an optimized nanowire metamaterial, demonstrating near-unity absorption over an unprecedented wavelength range from 400 nm to 1650 nm. The optimized dimensions (shown in the inset) were found to be: lattice constant: 900 nm; bottom diameter: 882 nm; top diameter: 340 nm; and height: 1400 nm.

in size until the absorption was enhanced over a broad spectral range (see Figures 3.3a and 3.3b). The optimal combination of parameters that we found included a top nanowire radius of 170 nm, bottom nanowire radius of 440 nm and height of 1400 nm.

Next, the optimal nanowire metaatom from Figure 3.3a was placed in a two-dimensional square lattice to form a metamaterial where the lattice constant can be leveraged to achieve broadband, near-unity absorption. In Figure 3.3c, we plot the calculated absorption efficiency as a function of periodicity. For this metaatom, we determine that broadband, near-unity absorption is achieved at a lattice spacing of 900 nm. Increasing the periodicity leads to a decrease in the absorption efficiency as the interaction between neighbouring nanowires weakens. Similar to cylindrical nanowire metamaterials, this behaviour implies that the larger lattice constant reduces the effective recollection of the scattered field by the tapered nanowire array. We note that a lower bound of 900 nm was set for the periodicity since a smaller separation would result in the nanowires overlapping, reducing their selected height.

In Figure 3.3d, we plot the calculated absorption efficiency over an extended wavelength range (400 nm to 1650 nm) at the optimal periodicity to highlight near-unity absorption over an unprecedented bandwidth. The calculated average absorption efficiency is found to be 92%, with peak efficiencies of 99% at 909 nm and 98% at 1406 nm. We note that the observed peaks in Figure 3.3d result from the nanowires being suspended in air; however, these peaks are later found to be less prominent in our updated model after including a substrate to better compare with the experimental results.

3.5 Device measurements

A scanning electron micrograph of the fabricated optimized nanowire metatoms is shown in the inset of Figure 3.4a. This image illustrates the uniformity of the tapered nanowires that was achieved during the fabrication process. The high absorption efficiency of the nanowire metamaterial is apparent in the optical image of Figure 3.4a as the array appears black when compared to the blue-grey InGaAs film. We performed FTIR spectroscopy to measure the absorption efficiency of the nanowire array. A tungsten light source was used to illuminate the sample, and a liquid-nitrogen-cooled Mercury-Cadmium-Telluride (MCT) detector was employed to measure the intensity of the reflected and transmitted spectra. To achieve a spot size smaller than the nanowire metamaterial dimensions in these measurements, a Schwarzschild reflective objective with a numerical aperture of 0.5 was used. The measured reflectance as a function of wavelength is shown in Figure 3.4b, illustrating the low reflection from the nanowire metamaterial. The reflectance is found to be below 4%

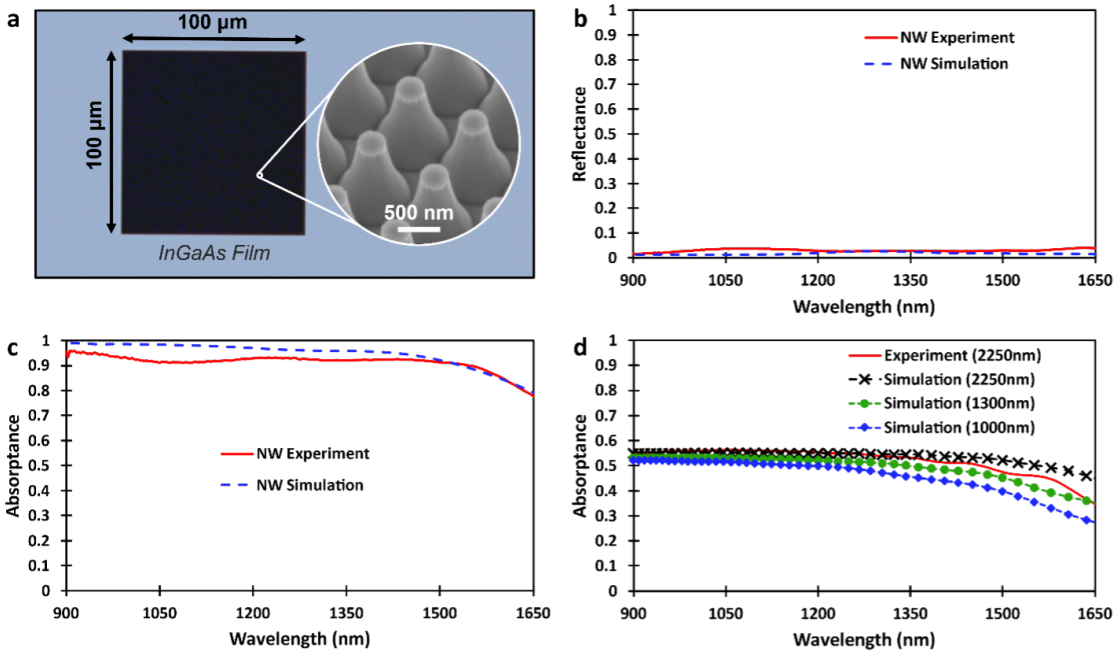


Figure 3.4: Near-unity nanowire metamaterial absorption. (a) Optical microscope image of the fabricated InGaAs tapered nanowire metamaterial (black square) on an InGaAs film (blue-grey). The lack of contrast in the 100 μm x 100 μm active area is indicative of high absorption. The inset shows a scanning electron micrograph of tapered InGaAs nanowires that is representative of the selected area from the high absorbing metamaterial region. (b) Comparison of the simulated and experimentally measured reflectance for the nanowire metamaterial as a function of wavelength. The fabricated (modelled) nanowire metamaterial dimensions are similar with a top radius: 175 nm (170 nm), bottom radius: 440 nm (441 nm), height: 1300 nm (1400 nm), and a pitch: 900 nm (900 nm). (c) Comparison of the simulated and experimentally measured absorption spectra of an InGaAs tapered nanowire metamaterial with the same dimensions as (b), which demonstrates the near-unity absorption over an unprecedented wavelength range. The measured (simulated) average absorption efficiency from 900 nm to 1500 nm is 93% (97%). (d) Measured and calculated absorption spectra of a planar InGaAs film on an InP substrate for various thicknesses - Measured film: 2250 nm; Modelled films: 1000 nm, 1300 nm, and 2250 nm.

over the entire wavelength range from 900 nm to 1650 nm, with an average reflectance of 3%. These results are compared to simulations of the same nanowire metamaterial dimensions, which show excellent quantitative agreement. We note that the fabricated nanowire

metamaterial dimensions closely resemble the optimized structure from the numerical calculations. The fabricated nanowire metamaterial (modelled metamaterial) was found to approximately have a top radius of 175 nm (170 nm), bottom radius of 440 nm (441 nm), height of 1300 nm (1400 nm), and a pitch of 900 nm (900 nm). We therefore updated the dimensions in our model for a direct comparison with experiment. We also note that the reflective objective in the FTIR experimental setup introduces a range of angles for light incident on the nanowire array from normal (0°) to 30°. Additionally, the nanowire array is fabricated from an InGaAs film on an InP substrate; however, up to this point the numerical models only considered InGaAs nanowires suspended in air. Thus, these factors were accounted for in our improved model for a more realistic comparison (further details in Appendix B).

We now bring attention to the measured broadband near-unity absorption, as shown in Figure 3.4c. Remarkably, we measure an average absorptance of 93% from 900 nm to 1500 nm, with a peak efficiency of 95%. Comparing these experimental results with the simulated data in Figure 3.4c, an excellent agreement is attained with minimal discrepancy. The small deviation that is observed between simulation and experiment may be due to the differing sidewall geometries of the fabricated and modelled nanowires. To obtain the absorption efficiency from the measured results, we utilize $A = 1 - R - T$, where A, R and T are the absorptance, reflectance, and transmittance, respectively. In our measurement, we found that the transmission data also comprises of thin film interference due to the presence of the reflective objective. We therefore corrected for this interference in the measured absorptance. Details of this correction procedure is presented in Appendix B5. We note that the process we implemented to correct for the thin-film interference underestimates the measured absorptance, thus providing a conservative lower bound to the absorption efficiency of the nanowire metamaterial.

To demonstrate the enhanced absorption in tapered nanowire metamaterials we compared it to an unprocessed bulk InGaAs film with a thickness of 2250 nm. The measured bulk InGaAs film absorptance is shown as a function of wavelength in Figure 3.4d (red solid curve). This experimental data is compared to the simulated bulk InGaAs film with an identical thickness of 2250 nm and demonstrates excellent agreement (black dashed cross). The enhancement of the absorption towards unity when utilizing the tapered nanowire geometry is evident when comparing tapered nanowires (Figure 3.4c) and the planar bulk material (Figure 3.4d). We also simulated bulk InGaAs with an identical thickness (1300 nm) to the thickness of the tapered nanowire array (green dashed circle) and a thickness (1000 nm) of commercially available InGaAs photodetectors for reference (blue dashed diamond). Numerical calculations and the measured performance for a series of varied nanowire geometries were also studied (see Appendix B). Despite deviating from the opti-

mized structure, measurements show the reproducibility of enhanced absorption.

3.6 Conclusion

We investigated the governing mechanism of enhanced absorption in InGaAs nanowire array metamaterials. We showed that enhanced absorption is achieved by the collective response of nanowires when the nanowire shape, height, diameter and periodicity is specially designed. Incoming light initially couple into the nanowires by means of hybrid leaky guided modes. As the light is guided vertically, a portion of the wave decouples due to its leaky nature. As the wave decouples, they subsequently excite transverse modes (TE and TM) of neighbouring nanowires. We have reported that these two mechanisms can lead to near-unity absorptance in InGaAs nanowires, provided that the nanowire separation (periodicity) is carefully selected to ensure a strong interaction between neighboring nanowires. Moreover, we have demonstrated a design guide to achieve near-unity absorptance for a broad wavelength range using tapered nanowires. With this design guide, we fabricated InGaAs nanowire arrays with a tapered nanowire geometry. We demonstrated experimentally that the fabricated InGaAs nanowire arrays exhibited near-unity absorptance of 93% in average for an unprecedented wavelength range from 900 nm to 1500 nm. The fabricated devices in this study is a demonstration of a design methodology of realizing near-unity absorptance for a desired wavelength range, and the wavelength range can be tailored for other spectral regions using the same principles. The findings here are hoped to help improving photon starved technologies such as quantum information, biomedical applications and LIDAR technologies.

Chapter 4

Fabrication of Nanowire arrays

This chapter presents the optimized method of fabricating nanowire array based photodiodes from InGaAs semiconductor thin films grown on InP substrates.

4.1 Process Flow

Fabrication of the nanowire array photodiodes are schematically shown in Figure 4.1. The device fabrication starts with an MBE growth of InGaAs stack layer precisely laying the doping profile to create pin structure on top of InP wafers (Figure 4.1a). The substrate is a S doped InP wafer (100) with an etch pit density of <100 cm^{-2}. The wafers with grown layers are then cleaned and a silicon nitride layer is subsequently deposited to form nanowire masks (Figure 4.1b). After the silicon nitride deposition, e-beam lithography is used to transfer the nanowire pattern onto the wafer. Following the e-beam exposure and development, a bilayer metal structure (Al/Cr) is deposited that creates a protective mask to pattern SiN_x nanowire masks. A lift-off process leads to the metal masks that protect the SiN_x under the Al/Cr mask from reactive ion etching as in Figure 4.1c. Next, SiN_x is etched with Inductively coupled plasma - reactive ion etching (ICP-RIE) creating the mask for nanowire etching as shown in Figure 4.1d. Consequently, InGaAs film is etched while the InGaAs under the mask is protected. This creates tapered InGaAs nanowire arrays with the designed top diameter (See in Figure 4.1e).Next, the back contact metal stack is deposited and annealed for improved contact resistance (also in Figure 4.1e) Then, the SiN_x hard mask (nitride and metal) is removed with chemical etching (See Figure 4.1f). Planarization will be done by initially depositing SiO_2 with PECVD, then filling the empty space between nanowires with a polymer called Benzocyclobutene (BCB), curing the BCB

for solidification, etching BCB until the nanowire tips are exposed and finally removing the SiO_2 from the tips (See Figure 4.1g). Next, ITO is be deposited as a transparent conductive oxide and it forms the top contact of the device as shown in the 4.1h. As a final step Ti/Au metal stack is deposited for wirebond pads (See Figure 4.1i).

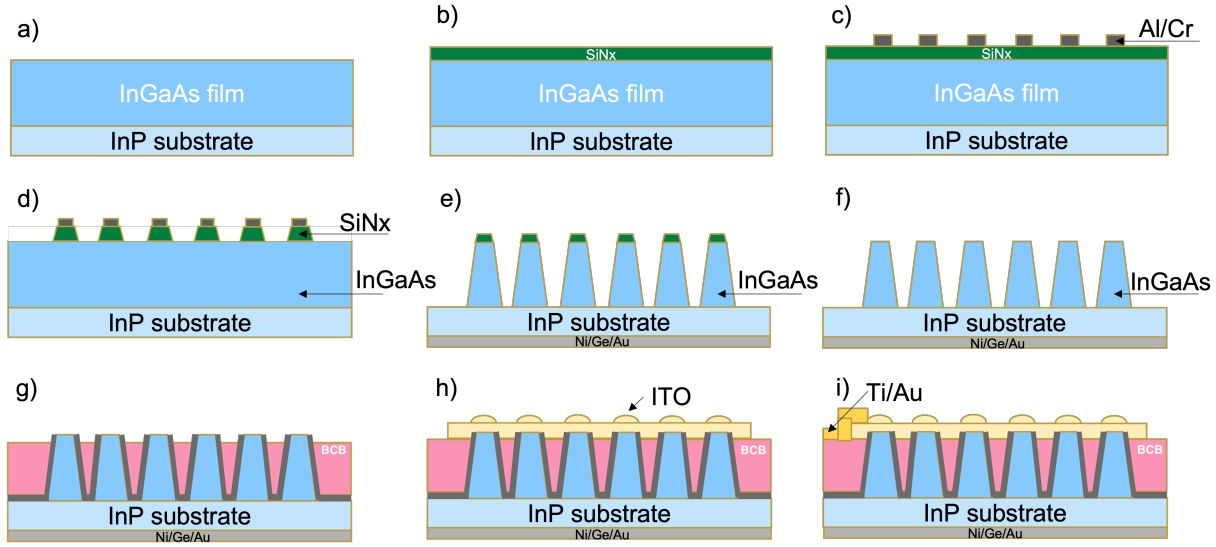


Figure 4.1: Process flow of InGaAs nanowire array photodiode fabrication: a) Molecular beam epitaxy (MBE) deposition, b) SiN_x hard mask deposition, c) E-beam lithography, Al/Cr hard mask deposition and lift-off, d) Inductively Coupled Plasma - Reactive Ion Etching (ICP-RIE) of SiN_x, e) ICP-RIE of InGaAs, f) SiN_x removal and back-contact deposition, g) Surface passivation, planarization with Benzocyclobutane (BCB) and removal of SiO_2, h) Photolithography and Indium Tin Oxide (ITO) deposition i) Photolithography and Ti/Au wirebonding pad deposition.

4.2 MBE growth of semiconductor layer stack

Molecular beam epitaxy (MBE) system is a common choice to grow high quality epitaxial layers with low defect density. More specifically, optoelectronic devices based on III-V material system can be grown with high quality thanks to high vacuum MBE systems. The source materials are heated to the gas form and sent to the heated substrate in a high vacuum chamber. With the help of this technique, monoatomic precision can be achieved. MBE is a time consuming and a costly method to grow single crystals compared to other

epitaxy systems such as MOVPE and MOCVD, nevertheless, it is ideal for prototyping, often achieving a better crystal quality. For our research, the high quality InGaAs and InGaAs-InAlAs thin films were grown with Veecco GEN10 MBE system in the Quantum Nano Centre Molecular Beam Epitaxy Laboratory managed by Prof. Zbigniew Wasilewski at University of Waterloo. The second generation of InGaAs-InAlAs thin films for separate absorption and multiplication region devices were grown by Intelliepi Inc (Richardson, Texas, USA).

The process starts with the selection of 3" InP wafers that were purchased from AXT Inc (Fremont, CA, USA). InP was chosen to grow lattice matched $In_{0.53}Ga_{0.47}As$ layers. A high carrier concentration of 10^{18} cm^{-3} (Sulfur doped) was selected for InP wafers to minimize the back contact resistance since the cathode of the diodes were formed on the back side of the wafers. Heavily n doped wafers are also found to have lower defect density [99]. A p-i-n diode structure was designed and grown for InGaAs photodiodes. An lightly doped n- region is sandwiched between two heavily doped n+ and p+ layers. Beryllium (Be) and Silicon (Si) atoms were used as the p type and n type dopants, respectively. The carrier concentrations and respective thicknesses of each layer is presented in Figure 4.2a. A more intricate design of single photon avalanche diodes requires multiple layered heterostructure, therefore, demands further optimization to achieve the required quality in terms of optical and electrical performance. However, the nanowire array and device fabrication were done with the same recipes.

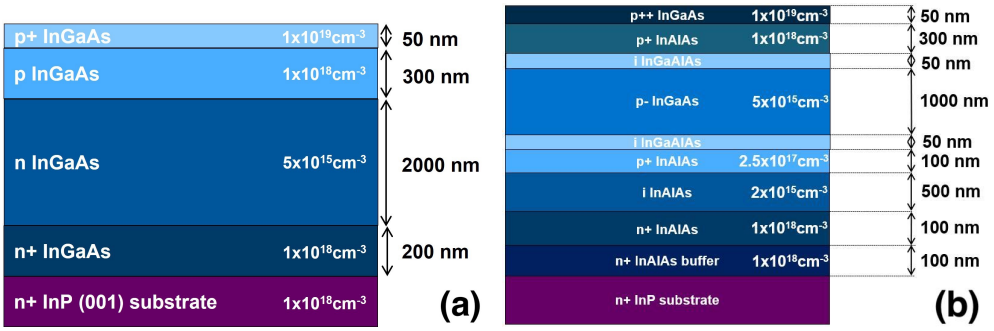


Figure 4.2: Device layer stacks of InGaAs pin and InGaAs-InAlAs separate absorption, charge and multiplication avalanche photodiodes layer stack deposited by molecular beam epitaxy.

After the growth, our analysis showed that the thin films contain minimal number of defects and have single crystalline atomic structure. InGaAs based p-i-n diode growth showed excellent quality as seen from the narrow X-ray diffraction (XRD) peaks and the smooth surface morphology in Figure 4.3a and c, respectively. Indium flux was overshot by

roughly 3% during the growth of G0821, which resulted in a compressive strain resulting in a minor lattice mismatch. There is a tiny split of InGaAs layer peak positions which is attributed to not only In flux drift but possibly also lattice expansion due to heavy Si/Be doping. An attempt to correct the In flux for InGaAs-InAlAs SPAD structure yielded tensilely strained InAlAs as seen from right shifted InAlAs peak on XRD plot in Figure 4.3b. The strained films are still considered up to par as seen by the smooth surface morphology as in Figure 4.3d; a further optimization can always be done for higher performance, however, this optimization is not the focus of this thesis. For the InGaAs-InAlAs thin film, the wide tails in the XRD image suggests further optimization is left for future studies.

We have also purchased custom MBE grown thin films of InGaAs-InAlAs from Intelliepi Inc when University of Waterloo MBE system was undergoing a major upgrade/maintenance. Similar avalanche photodiode structure to our APDs was grown by the same company for a different research group and the results are reported elsewhere [**?**]. The avalanche photodiodes based on the films from the company also showed high crystal quality.

4.3 Preparation of hard masks for nanowire creation

After the film growth, the wafer was diced into 0.75 x 0.75 cm square pieces to work with small individual chips. A standard solvent cleaning was applied to remove organic contaminants and residing dust on the chip surface: Diced wafer pieces were dipped into beakers filled with Acetone then Isopropyl alcohol (IPA) in ultrasonic agitation tank for 10 minutes each sequentially. After solvent cleaning, the chips were dried with Nitrogen blow gun. Next, the chips were submerged into a Buffered Oxide Etch (BOE) 10:1 solution to remove any native oxide residing at the surface. The samples were kept in BOE around 30-60 seconds until the surface shows hydrophobic nature.

After removal of the native oxide, the samples were transferred to our plasma enhanced chemical capor deposition (PECVD) (Oxford 100 PECVD/ALD) chamber to deposit Si_3N_4. Si_3N_4 was the choice of hard mask material for its chemical sturdiness during InGaAs etching and ease of removability with the buffered oxide etchant without damaging the InGaAs, therefore, it is used to etch protect InGaAs to create nanowires. A 500 nm Si_3N_4 layer was deposited on the top side of the chips; a thickness enough to achieve an etch depth nanowire height of 2 μm without fully etching Si_3N_4. PECVD SiO_2 was also tried as an alternative hard mask for nanowire fabrication, however, the surface quality of the nanowires were found to be poor (rough surface) after the process.

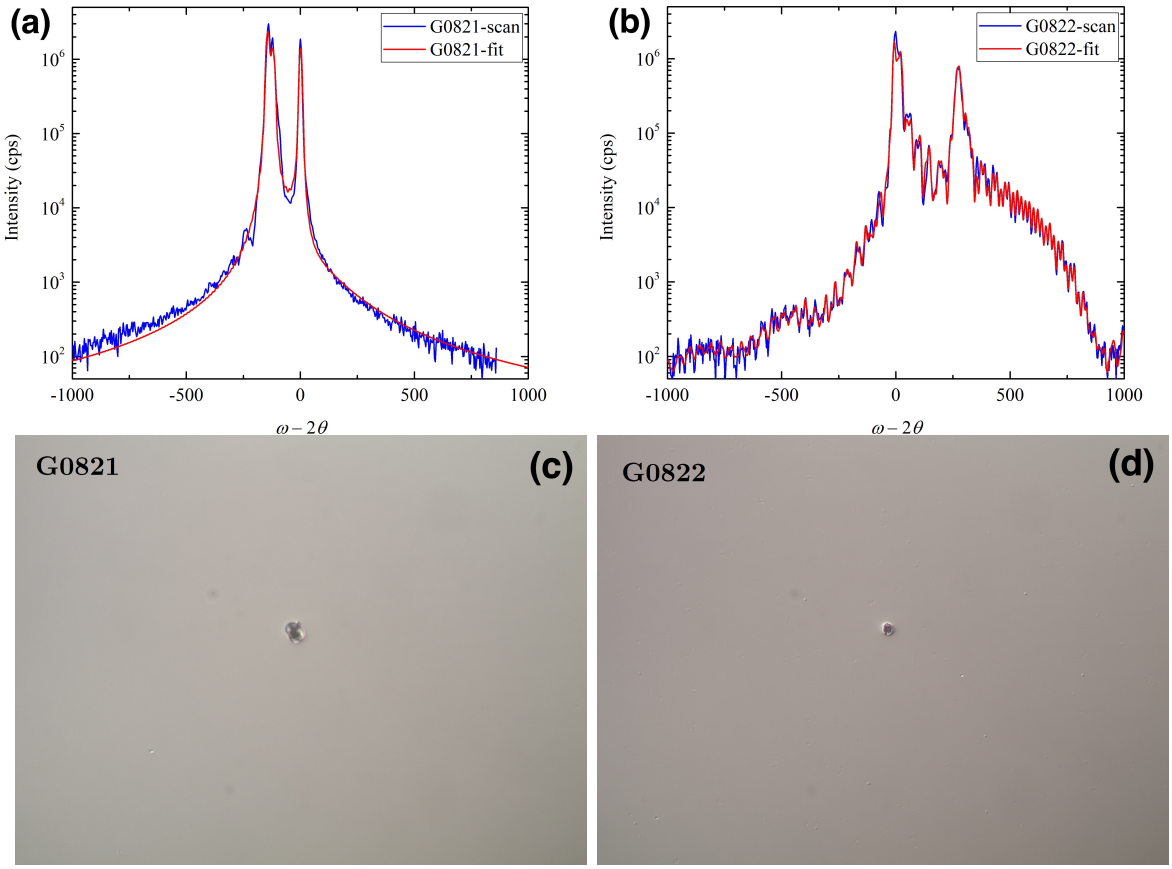


Figure 4.3: X-ray diffraction measurements and Nomarski microscope images for InGaAs p-i-n (G0821) and InGaAs-InAlAs (G0822) separate absorption, charge and multiplication avalanche photodiode thin films. The central marks on the Nomarski images are not crystal defects but laser created defects for optimal focusing. The craters, on the other hand, are indicators of localized defects or stacking faults.

After Si_3N_4 film growth, e-beam lithography resist, PMMA A3, was spin-coated with a target thickness of 150 nm followed by soft baking. Then, the chips were placed into the e-beam lithography system (JEOL JBX-6300FS) to expose nanowire patterns. The design of the e-beam lithography patterns of InGaAs nanowires follows the analysis done on the optical absorption study described in 3. A varied set of nanowire diameter and period values were included in the e-beam lithography patterns to test the validity of the optical simulations and the electrical performance of different nanowire geometries. The target top nanowire diameters scale from 320 nm up to 400 nm were used with periods of 700

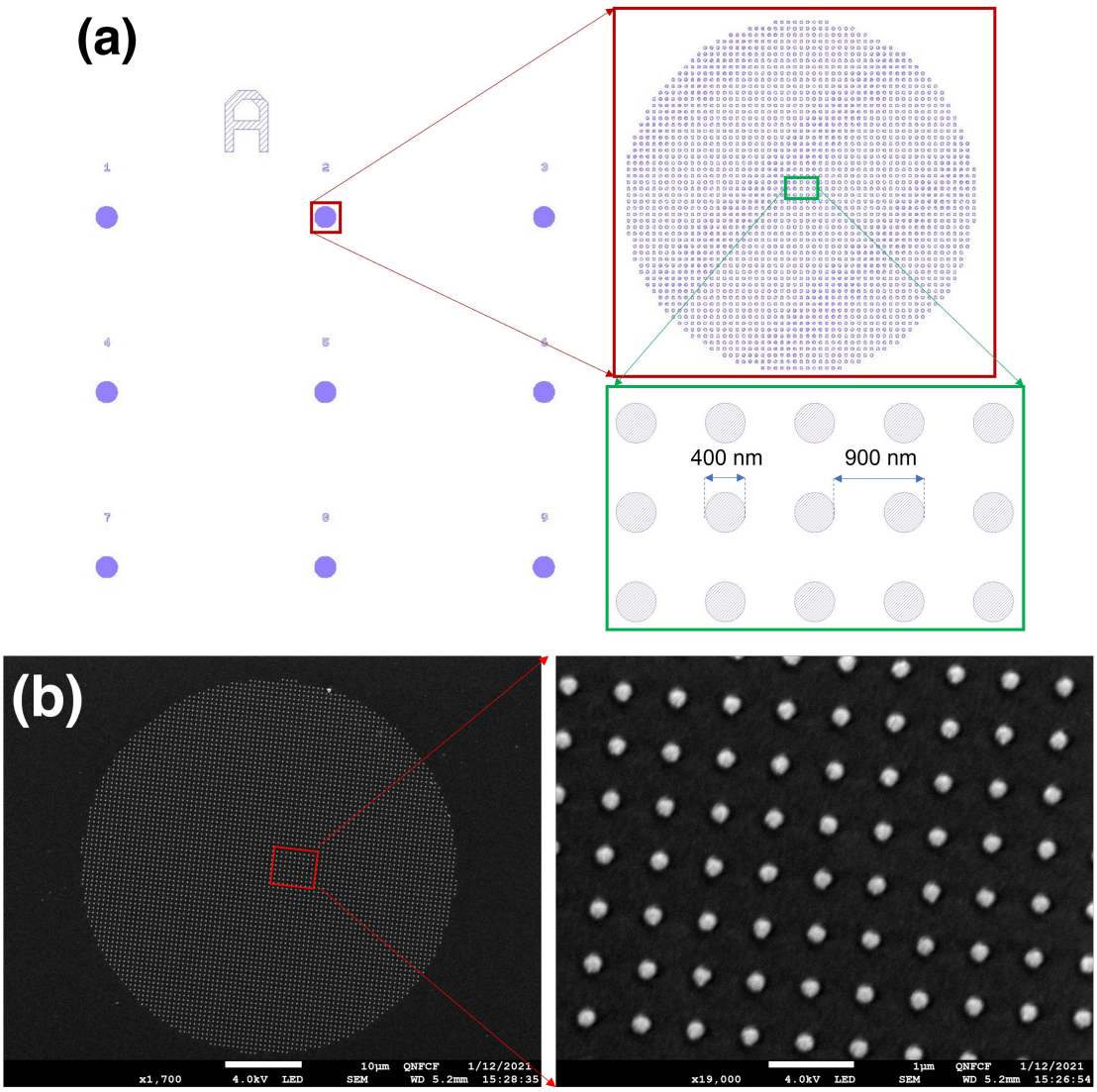


Figure 4.4: Nanowire array pattering with e-beam lithography and metal mask deposition. a) E-beam lithography masks ofInGaas nanowire arrays varied diameter and pitch, b) Scanning electron microscopy image of the resulting pattern on the wafer surface including . The mask has 9 different device configurations nanowire arrays with varied top nanowire diameters (320, 340, 360, 380 and 400 nm) and pitch (700, 800, 900, 1200, 1400 nm) values.
.

nm, 800 nm, 900 nm, 1200 nm and 1400 nm. Figure 4.4a shows a device with a diameter of 400 nm and a pitch of 900 nm.

Before depositing real patterns, a dose test was applied to find out the optimal electron beam exposure intensity. Doses scanning from 600 μJ/cm^2 to 1400 μJ/cm^2 with a step of 100 μJ/cm^2 were tested. The dose values lower than 1000 μ/cm^2 resulted in under-developed patterns. 1000 μJ/cm^2 and above were sufficient for the transfer of patterns. After selecting the exposure value of 1000 μJ/cm^2, the nanowire mask patterns were exposed onto a PMMA layer, followed by development using MIBK:IPA (1:3) solution. Exposed regions lifted-off during the development process, creating openings for metal hard masks. The metal hard mask was used to pattern Si_3N_4, which then protects the nanowire cores from exposure to the etchants in ICP-RIE system. Cr initially was selected as the metal mask which is known to be a durable material for this type of etching. However, Cr is also a "soft metal" making the lift-off very problematic, which was also experimentally observed. To circumvent the lift-off problem, a thin Al layer was depositedbefore Cr deposition as successfully demonstrated elsewhere [129]. The lift-off was successfully performed using Al/Cr metal combination with thicknesses 15 nm and 40 nm for Al and Cr, respectively. Figure 4.4b demonstrates the Al/Cr metal hard mask created on the Si_3N_4 layer.

4.4 Top-down nanowire etching

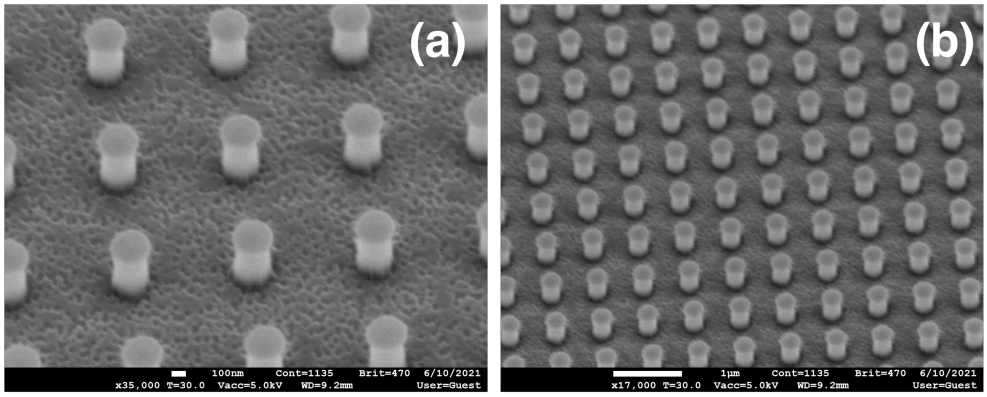


Figure 4.5: Scanning electron microscopy images of etched SiN_x using inductive plasma coupled - reactive ion etching system. a) Close-up view of the sample surface, b) Zoomed out version of the surface.

To pattern nanowire arrays, SiN_x hard mask structure was created by etching SiN_x using ICP-RIE (Oxford ICP380) system until only the hard masks formed by e-beam lithography remains on the InGaAs surface. Al-Cr metal hard mask was still remaining at the top of SiN_x after 115s ICP-RIE etch of Si_3N_4. The metal mask is still sitting on top of the masks, without fully etched, showing that the thickness of the metal was sufficient for the Si_3N_4 etch process as in Figure 4.5. The nanowire surface after InGaAs etch was found to be very rough when SiO_2 is used compared to Si_3N_4. Since BOE can also etch Si_3N_4 [130], we selected Si_3N_4 as the hard mask material for InGaAs etching. The fabricated SiN_x hard mask are shown in Figure 4.5.

To etch InGaAs, it is important to use the right chemistry to obtain the desired geometry and surface morphology. In general, In-based materials are hard to etch due to involatile In byproducts at low temperatures, as a result, In-based clusters are redeposited onto the surface, reducing the etch rate and increasing the surface roughness [131]. To alleviate this problem, increasing the chamber temperature is a possible solution, however, it is costly and time-consuming. Also, high temperatures might cause the chemicals to outgas and contaminate the chamber sidewalls and process wafers. In a typical etch process, a thermal paste is applied to the back side of the chips to ensure good heat transfer between the wafer chip and the carrier wafer, as a consequence, the wafer chip is kept at the same temperature during the process. If the material is etched without using the thermal paste, heat as a result of the process would be trapped within the chip and raises the local chip temperature. The heating of the wafer chip can provide enough energy to volatilize the $InCl_x$ clusters. In this way, the wafer chip can get to the high temperatures without heating the chamber.

To etch InGaAs with smooth surface the right combination of gases needs to selected. Typically, Cl-based gases such as Cl_2, BCl_3 and $SiCl_4$ or CH_4 are used to etch In based semiconductors such as InGaAs or InP [132, 133, 134, 135]. Pure Cl_2 recipes generally give a high etch rate, but the surface roughness becomes an issue due to the involatile $InCl_x$ clusters [136]. CH_4 gas is alternatively used for smooth etching; however, it leads to excessive polymer deposition around the chamber walls and on wafer surfaces [137]. To exploit to benefits of both, we use a recipe that combines different ratios of Cl_2, CH_4 and H_2 to perform the etch. H_2 is added to the mixture in order to neutralize the surface charges which is helpful to achieve a smoother surface. We have kept the temperature at 60^oC for most of the processes for the sake of simplicity, but, higher temperature is known to improve the surface quality of InGaAs nanowires [132]. We initially used the recipe InP OPT and Recipe 1 (Same recipes except the flow rates of each gas is doubled in order to test the flow rate ratio) in the Table 4.1.

The etch rate was found to be around 300 nm/min based on the three different samples.

Table 4.1: Investigated Inductive Coupled Plasma - Reactive Ion Etching recipes to etch InGaAs and InAlAs. The table presents parameters RF power, ICP power, Cl_2 flow, CH_4 flow, H_2 flow, chamber pressure and process temperature, respectively.

Recipe	**RF**	**ICP**	**Cl_2 flow**	**CH_4 flow**	**H_2 flow**	**Pressure**	**Temp**
InP OPT	65 W	2000 W	8 sccm	4 sccm	7 sccm	4 mTorr	60^{o}C
R1	65 W	2000 W	16 sccm	8 sccm	14 sccm	4 mTorr	60^{o}C
R2	65 W	2000 W	12 sccm	4 sccm	7 sccm	4 mTorr	60^{o}C
R7	65 W	2000 W	16 sccm	10 sccm	14 sccm	4 mTorr	60^{o}C
R9	65 W	2000 W	16 sccm	16 sccm	14 sccm	4 mTorr	60^{o}C
R10	75 W	1000 W	6 sccm	10 sccm	15 sccm	2 mTorr	60^{o}C
R11	75 W	500 W	6 sccm	10 sccm	15 sccm	2 mTorr	60^{o}C
R12	50 W	500 W	6 sccm	10 sccm	15 sccm	2 mTorr	60^{o}C
R13	25 W	500 W	6 sccm	10 sccm	15 sccm	2 mTorr	60^{o}C

The etch rate of the mask was found to be less than 100 nm/min. The SEM image of the etched nanowires with those recipes are displayed in Figure 4.6a. It is clearly seen that the the initial recipes yielded nanowires with hourglass shape. The resulting nanowire arrays looked well-ordered, the surface and the sidewalls looked smooth as seen in Figure 4.6a. There was a noticeable undercut in the individual nanowires and the undercut was more pronounced when the pitch was larger. Arrays with 150 nm top diameter seemed to have a bottleneck structure, where some nanowires were broken because of the thinning around the waist.

The tapering of the nanowire enables the broadband absorption for the proposed devices as discussed in Chapter 3. Therefore, the fabrication of nanowire arrays with a proper taper angle was critical for our project. We studied parameters of etching one by one in order to have a greater control on the nanowire shape. The set of parameters that can be changed were Cl_2 and CH_4 flow rates and their ratio, ICP and RF powers, chamber pressure and ambient temperature. It was previously shown that the ratio between the gas flow rates of Cl_2 and CH_4 can modify the taper angle. Cl_2 rich RIE etch processes was shown to produce positive angled structures whereas CH_4 processes result in vertical or slightly undercut etch profiles on In-based substrates [135]. According to the literature analysis, a

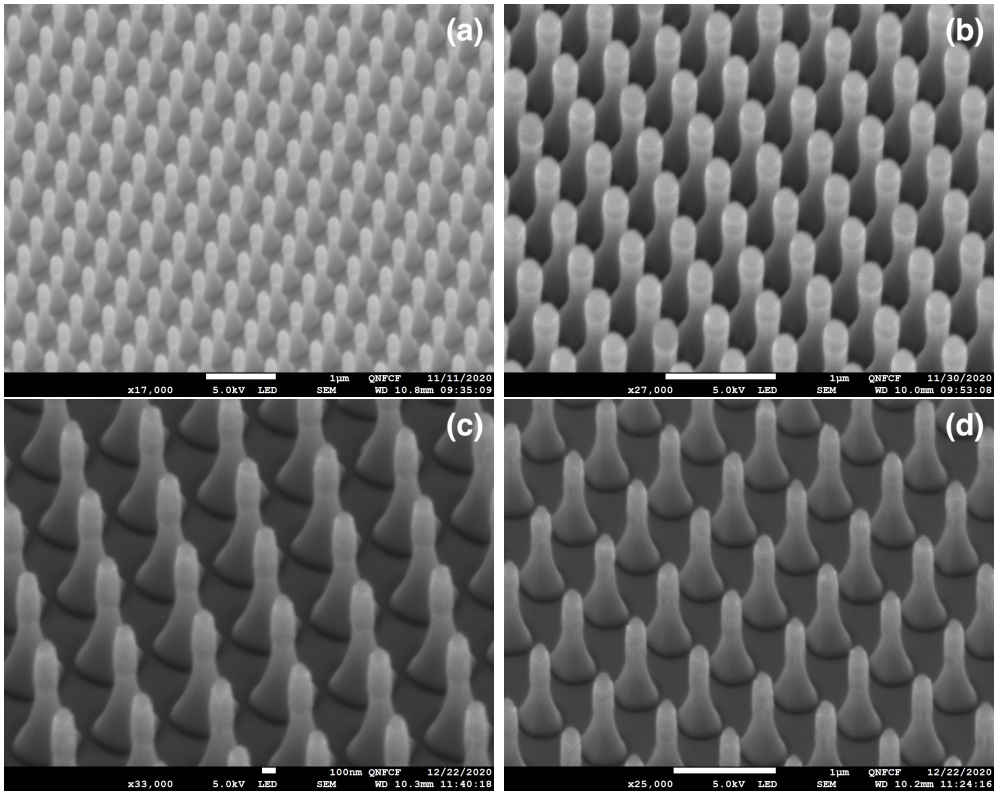


Figure 4.6: Scanning electron microscope images of InGaAs nanowire array etched with varying recipes Cl_2/CH_4 ratio. Scanning electron microscope images of InGaAs etch with Recipes a) 1, b) 2, c) 7 and d) 9. The recipes have the same conditions except the Cl_2/CH_4 ratios are 3, 2, 1.6 and 1, respectively.

higher ratio between the flow rates of CH_4 and Cl_2 was thought to decrease the tapering angle, i.e., the nanowires could be shaped closer to a cylinder (or more undercut depending on the complex chemistry of RIE) than the truncated cone shape. Reversely, a smaller ratio was estimated to create more positive sidewalls, the structure would get closer to a truncated cone geometry. Controlling the taper angle as well as the overall shape could add another dimension to control the optical mode inside the nanowire aside from top diameter and adjacent nanowire separation. To tune the shape of individual nanowires, several etch recipes have been tested as shown in Table 4.1. First, we analyzed the effect of Cl_2/CH_4 ratio in an ICP-RIE chamber. The recipes R1, R2, R7 and R9 were applied to different samples from the same wafer with corresponding Cl_2/CH_4 ratios of 3, 2, 1.6 and 1, respectively. The SEM images of the fabricated nanowire arrays with each recipe

is displayed in Figure 4.6. The reduction in the Cl_2/CH_4 ratio resulted in a rather subtle change in the geometry unlike the reported observations. While the top of the nanowires became more cylindrical, the bottom half still had high positive slope (Figure 4.6). It was clear that the process was dominated by the other parameters which separated our observations from the previously reported studies.

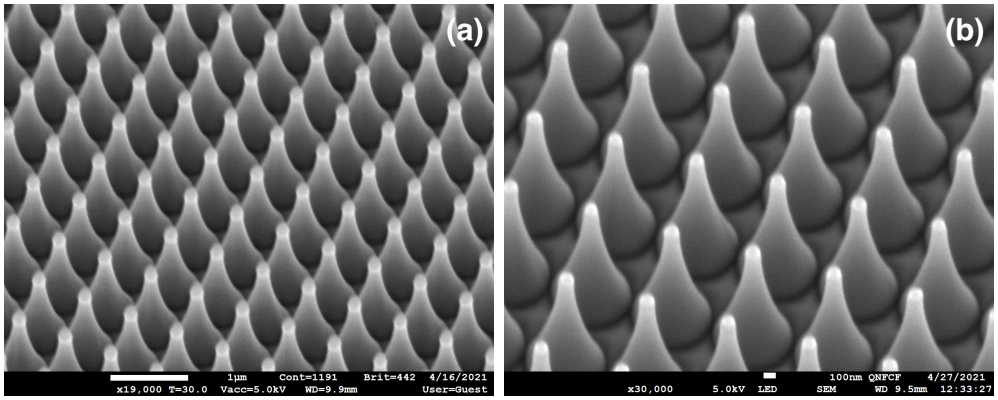


Figure 4.7: InGaAs nanowire array fabrication. SEM images of InGaAs nanowire arrays fabricated with Recipe 10 and Recipe 11. Recipe 11 had 500 W ICP power while Recipe 10 had 1000 W. All the other parameters of the process were the same.

Next, the ICP and RF powers as well as the chamber pressure was modified to alleviate the strong undercut behavior leading to the hourglass shape. Cl_2/CH_4 ratio was dropped below 1 targeting a more cylindrical shape especially at the bottom half. Also, the previous ICP power of 2000W was found to be too strong and was potentially the primary reason of the negative tapering angle at the top by increasing the local temperature rapidly in turn leading to a more isotropic etch. In addition, the chamber pressure was cut to half from 4 mTorr to 2mTorr in order to promote more vertical etching since the lower pressures would result in less scattering of ions and radicals. Finally, the RF power was increased slightly to supply more energy to the radicals to reduce undercut and support vertical etching. We also continued to process the wafer chips without the use of thermal paste; however, we divided the process into steps of shorter etches to limit the excessive heating of the sample in long process times. For instance, we etched the InGaAs with recipe 10 for 12 minutes in total, but the process was performed by two 6 minute etches (6+6 mins) just to limit the overheating of the samples over a longer time. After this major upgrade (Recipe 10), the shape of the nanowires improved substantially (Figure 4.7). The undercut was still observed, however, the hourglass shape disappeared. In addition, recipe 11 which had 500 W ICP power compared to 1000 W in recipe 10 was used to etch InGaAs. The InGaAs

etch rate of recipe 11 was found to be the half of recipe 10 as the ICP power was reduced to half, therefore, the sample was for 24 minutes (12+12 minutes) to achieve the same nanowire height of 1.3 μm for a fair comparison. The nanowire shape was very similar what is achieved with recipe 10, however, a stronger sidewall erosion was observed as seen by the shrinkage of the top diameter of the nanowires in both recipes. It was also clearly deduced from this analysis that the etch rate is linearly related to the ICP power.

We have also investigated the effect of RF power on the nanowire shape. For that purpose, we created recipes 11, 12, 13 that had RF powers of 75 W, 50 W and 25 W, respectively, while the other parameters kept constant. The fabricated nanowires with recipes 11, 12 and 13 are displayed in Figure 4.7b, Figure 4.8a and Figure 4.8b, respectively. The reduction in RF power lowered the etch rate since it took 24 mins, 32 mins and 42 mins to etch the same height of nanowires (1.3 μm). The recipe 12 had nice surface properties similar to recipe 11 but a more pronounced undercut was observed at the top portion of the nanowires. Also, the initial taper angle was sharper at the top and it widened more rapidly towards the base compared to recipe 11. On the other hand, recipe 13 yielded a similar shape to the Recipe 7 with cylindrical top half and high taper angle bottom half. Also the surface roughness was clearly seen to be an issue.

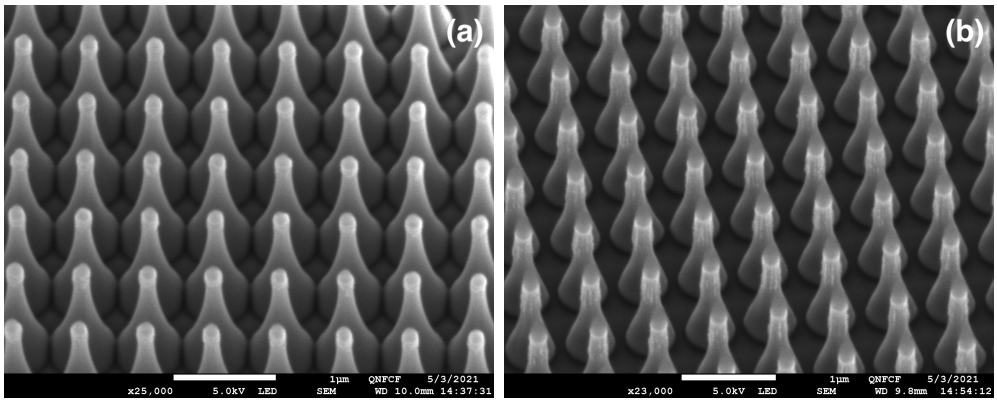


Figure 4.8: [InGaAs inductively coupled plasma reactive ion etching nanowire array fabrication with varying RF power. Scanning electron microscopy images of nanowire arrays fabricated with a) Recipe 12 and b) 13. Recipe 12 had an RF power of 50 W while Recipe 13 had 25 W. The remaining recipe parameters were kept the same.

Based on the analysis of the SEM images, we have chosen the recipe 10 for the device fabrication. To create nanowires as close as possible to the optimized structures based on optical simulations, we used larger mask diameters to etch InGaAs nanowire arrays

accommodating the strong sidewall etching. The fabricated InGaAs nanowire arrays after the hard mask is cleaned is displayed in Figure 4.9a. The nanowire height was measured to be around 1.3 μm after 12 minutes of total etch time. To reach to the desired nanowire height of 1.5 μm, we etched the same nanowire array an additional 1.5 minutes as shown in Figure 4.9b. Interestingly, we observed a smoother nanowire surface after that final 1.5 minute etch. This observation is attributed to the relatively milder temperature in a short 1.5 m process compared to 6 + 6 mins process.

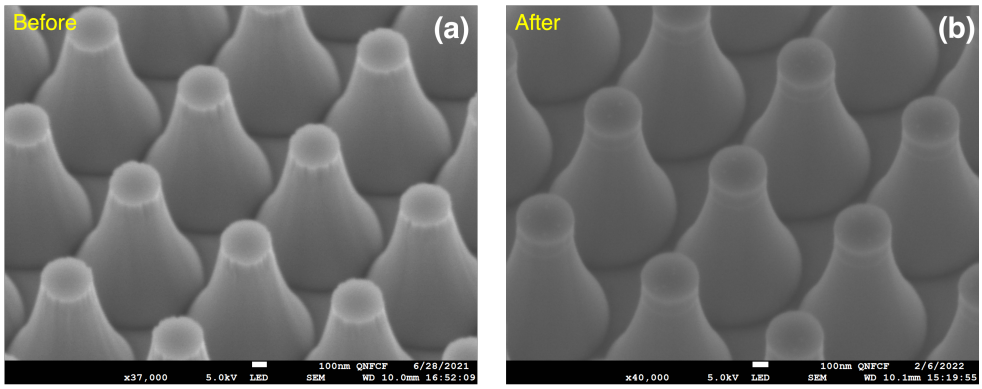


Figure 4.9: Nanowire sidewall smoothening. Scanning electron microscope images of InGaAs nanowire arrays fabricated with Recipe 10 with larger hard mask diameter of a device with mask of 400 nm top diameter. The separation is 900 nm. a) Image of the nanowire array after 12 (6+6) minute of InGas etching, b) Image of the nanowire array after 13.5 (6+6+1.5) minute of InGaAs etching.

4.5 Surface passivation

ICP-RIE process is known to induce damage to the sidewalls of the nanowires due to ion bombardment and byproduct desorption [132]. The damage can degrade the device performance if the damaged area is part of the active region of the photodiodes. For instance, mid gap defect centers formed after nanowire etching could cause charge trapping/detrapping deteriorating current stability. Therefore, the ion induced damaged needs to be removed followed by an effective surface passivation. The common approach is to apply digital sidewall etching [138]. Digital etching method, a self limiting etching process is ideal for cleaning the sidewalls of nanostructures without over-etching. Also, this method cleans the surface from any organic byproducts of the ICP-RIE etch process further improving the

interface quality. In addition, digital etching process is also commonly used to thin the diameters of nanowires controllably without damaging the structures, even single nanowires with diameters 30nm-50nm [133].

Wet etching of III-V materials is done by submerging the semiconductor into an acid solution consisting of oxidizing agent and complexing (oxide etching) agent.Oxidation is followed by oxide etch in this process; the material is getting etched continuously by the sequential oxidation and oxide removal.The etch rate is determined by the total time the material is kept in the acid solution. In digital etching, those two agents are applied separately and cyclically, therefore, the total etch depth is determined by the number of cycles. The oxidization of materials like GaAs and InGaAs are diffusion limited, the oxidation thickness scales logarithmically with time. DeSalvo et. al. showed [139] that 6 days of H_2O_2 submersion at room temperature yielded on 11.5 nm oxide thickness in GaAs. Hussey et. al. [140] showed an oxide thickness of 0.7 nm after 60 minutes of oxidization at 300^oC. This process is very slow, therefore, it allows a precise control of the etch depth. In addition, stoichiometry measurements revealed that the ratio of Ga-O to As-O is approximately 1 after oxidizing GaAs surface, suggesting that the oxidation process occurs very uniformly [139]. This leads to atomic smooth surface once the oxide is removed.

We have used digital etching to clean the surface of InGaAs nanowire arrays after ICP-RIE process. An oxygen asher system (YES CV200RFS) is used to oxidize the surface with a typical descum recipe. After that, the diluted H_2SO_4 solution is used for 10 s to remove the oxide layer. The etch rate was found 2 nm/cycle after repeating the cyclic process 10 times. The number of etch cycles was further investigated to optimize the process.

After digital etching, device fabrication continued with passivation of the nanowire surfaces and isolation between the top and the bottom contacts. The wafer chips were directly transferred to the PECVD system for deposition of a passivation layer. A 150 nm SiO_2 was deposited. The inspected SiO_2 thickness around the vertical sidewalls is found between 70-80 nm. The SiO_2 deposition is followed by a thick photoresist spin-coating to the top side, cleaning the native oxide by BOE on the bottom face of the chip, then deposition of a metal stack of Ni:Ge:Au (20:20:40 nm). After the deposition, the photoresist is cleaned thoroguhly from the top surface and the sample was annealed at 430^oC for 60 s in Ar environment to improve the bottom contact resistance.

4.6 Planarization and contact formation

Benzocyclobutane (BCB) was used for planarization. BCB is a commonly used passivation polymer with long chemical and thermal stability, low electric conductivity and high mechanical strength. It comes in liquid form, therefore, it can be spin coated on the samples, then cured at high temperatures for solidification. It also has strong adhesion to SiO_2, therefore, it is ideal for planarization of nanowire arrays for photodiode applications. AP3000, the adhesion promoter of BCB was also applied before BCB to improve the surface adhesion. Cyclotene 3022-46 (BCB) was spun for 5000 RPMs giving a thickness of 2.3 μm, which is enough to fully cover 1.5 μm nanowire thickness. After the spin-coating and back side edge bead removal, the sample was placed in nitrogen purged oven to cure the BCB layer. The sample was kept at 250^{o}C for 60 minutes until the BCB is >98% cured. The temperature profile was ramped according to the company technical sheet [141]. It was verified by profilometer measuremenets that the surface roughness of 2.3 μm BCB layer is less than 100 nm within 7.5 mm $\times$ 7.5 mm sample area.

Next, the BCB layer was etched plainly using ICP-RIE system with a recipe containing gas combinations of SF_6 and O_2 with a ratio of 1:5. The etch was performed with two steps. The first etch had 2000W ICP power with a BCB etch rate of 1.1 μm/min. The second etch was performed with a softened version of the first recipe with an etch rate around 180 nm/min. The successful etch of BCB layer to expose the tip of the nanowires are shown with SEM images in Figure 4.10a.

Once the nanowire tips are uncovered, a bilayer PMGI and S1811 photoresists were spin coated. ITO contact areas are exposed by maskless photolithography (MLA 150) system and patterns were developed opening up the areas of device contact. Then, the sample is once again dipped into BOE (10:1) to remove the SiO_2 cap on top of the nanowires. The top surface of nanowire arrays were carefully inspected until the SiO_2 cap is fully removed. This step is immediately followed by deposition of 300 nm thick ITO using sputtering system (AJA-ATC Orion). The samples were kept in a Remover PG solution overnight until ITO lift-off is complete. The deposited ITO contact pads are shown in Figure 4.10b. This method is preferred over blank ITO deposition and etching due to a difficulty in ITO wet etch process.

Finally, the wirebond pads were patterned with photolithography and a 20:180 nm Ti:Au metal stack was deposited on top of ITO pads. The fully fabricated devices are inspected under microscope and SEM as shown in Figure 4.11. To perform optoelectronic testing on the fabricated devices, the devices were glued on leadless ceramic chip carriers. Next, the electrodes of the devices were electrically connected to the pins of the chip carrier

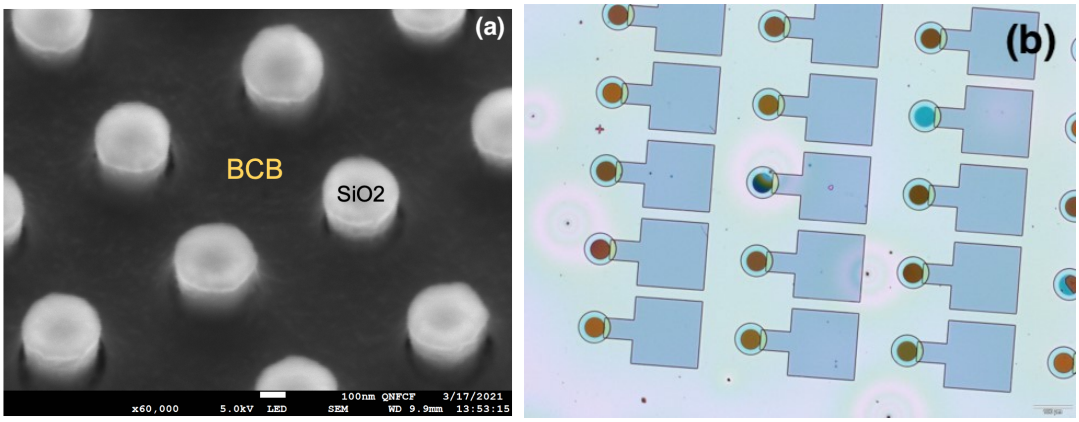


Figure 4.10: Etching Benzocyclobutene (BCB) layer to expose nanowire tops and depotision of ITO contacts. a) SEM image of plainly etched BCB until the nanowire tips were exposed. b) A microscope image of ITO contact pads placed on the nanowire arrays as well as the wirebond contact pads.

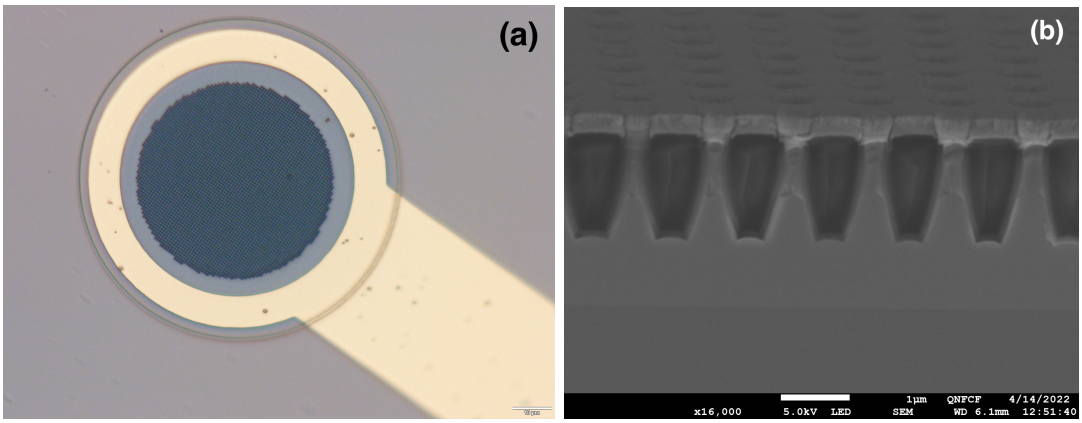


Figure 4.11: Microscope and scanning electron microscope images of the final fabricated device structure. a) A top microscope image of the completely fabricated device.b) A cross-sectional scanning electron microscopy image of the fabricated InGaAs nanowire array photodiode.

by means of gold wire bonds. The previous trials had issues with proper wire bonding due to poor adhesion properties of the filling material (BCB) underneath the gold electrodes. The wire bonds did not stick to the pads while stripping off the residing material. The problem was resolved by depositing an Indium tin oxide (ITO) layer before the gold electrodes. ITO

layer under the gold electrode improved the adhesion properties of gold while preventing the metal strip-off. After a few optimization runs, high yield wire bonds were achieved. Also, the bond pad size was increased to accommodate multiple wire bonds for high-speed measurements.

Chapter 5

InGaAs p-i-n nanowire array photodiodes

Chapter contributions: Lin Tian assisted with Ti:Sapphire laser responsivity and photocurrent measurements. Tarun Patel assisted with the FTIR photocurrent measurements. Brad van Kasteren and Sasan V. Grayli performed optical absorption simulations using Lumerical FDTD. William Losin assisted with electric field simulations for gain study. Man C. Tam and Zbigniew Wasilewski performed thin film growth of InGaAs.

5.1 Device fabrication and packaging

InGaAs nanowires arrays were created with the optimized recipe discussed in Chapter 4. Then, the samples were dipped into a 10:1 Buffered oxide etchant (BOE) solution for 7 minutes to remove the remaining hard mask of SiN_x after the InGaAs etch process (Figure 5.1a). The removal of hard mask was followed by nanowire surface cleaning with oxygen plasma exposure and 10s dip of the samples into diluted H_2SO_4 solution. The samples were immediately transferred to the PECVD system to passivate the surface with SiO_2. A 150 nm SiO_2 layer was deposited. Then, the top side of the sample was covered with a photoresist for protection, the bottom side native oxide was cleaned with a BOE dip. Back contact metal of 20:20:40 nm Ni:Ge:Au stack was deposited with e-beam evaporation. After lift-off, the samples were annealed at 430^{o}C for 60s to improve contact resistance. Next, 2.2 μm thick BCB was spin-coated and cured on the top side, then consequently etched back plainly by the ICP-RIE system until the tip of the nanowires were exposed.

The sample was submerged into BOE for 30s - 40s to remove the SiO_2 cap, then the samples were directly loaded into Sputtering system to deposit ITO transparent top contacts right after a photolithography step. Finally, a 20:180nm Ti:Au metal wirebond pads were first patterned with photolithography then deposited. Cross sectional SEM image of a device cut from the sample is displayed in Figure 5.1d. After lift-off the devices were glued on a ceramic chip carrier and devices were connected via wirebonding to gold pads of chip carrier (Figure 5.1c,d).

5.2 Current-voltage characteristics

Firstly, we fabricated a standard mesa type device in an InGaAs p-i-n device structure to examine the bulk current voltage characteristics as shown in Figure 5.2. The current-voltage characteristics of the InGaAs p-i-n large area devices (planar devices) were initially measured at the probe station using a semiconductor parameter analyzer. The diodes showed good rectification current behavior with on-off ratios of 10^6 when compared between -1V (reverse biased) and 1V (forward biased). The devices also exhibited smooth curves indicating that the device is free from crystal impurities or fabrication related defects. We simulated the device current voltage behavior using Atlas Silvaco TCAD to identify the dominant dark current mechanism. For that purpose, we enabled different sources of dark current mechanisms individually, namely Shockley-Read-Hall (SRH) recombination, trap-assisted tunneling (TAT) and band-to-band tunneling (BBT). We also combined them to determine which dark current mechanisms could best explain the measurement data. The measurement curve agreed quite well to the simulation result with all three dark current mechanisms included using carrier lifetimes for electron and hole of 10 ns. At lower voltages, the current was predominantly affected by the trap assisted tunneling mechanism, while at higher biases, the band-to-band tunneling became prominent. The latter mechanism is a property of the bandgap of the material itself and independent from the film growth quality, whereas the former can significantly be improved with optimizations in epi-layer growth quality. The strong voltage dependence of the dark current suggests that the trap assisted tunneling combined with SRH current is the dominant factor up to -35 V. The contribution of SRH current seems relatively weak when it is solely used. The origin of the trap-assisted tunneling is believed to arise from the carrier generation near mid-gap bulk and surface defects since the depletion region reaches to the mesa surface. band-to-band tunneling current starts to overcome the SRH and TAT current at around -30 V. In the measurement result, the current especially follows the same trend with the band-to-band tunneling current indicating that the mechanism after -35 V is mostly dominated by BBT

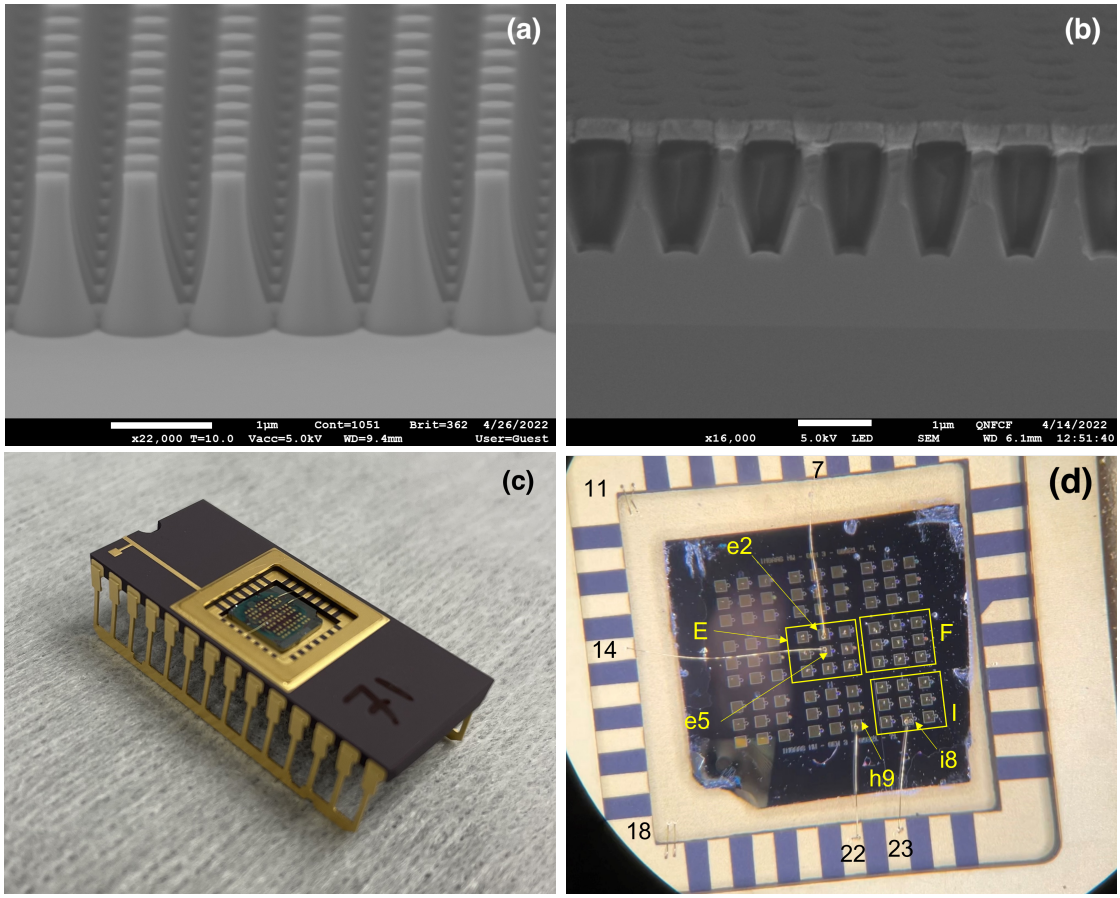


Figure 5.1: Device fabrication and packaging of InGaAs p-i-n nanowire array photodiodes. a) Fabricated InGaAs nanowire arrays. b) Cross sectional SEM image of the device. c) A photograph of the wafer chips that were diced and glued on ceramic chip carriers. d) Microscope image of the wafer chip 71 showing the outline of cells and wirebonded devices. Each cell is represented by a letter with respect to its position on the chip and each device within cells is represented by a number. The corresponding nanowire geometry for each device is given in Table 5.1.

current. There is no indication of avalanche breakdown onset up to -40 V. The soft knee visible at -35 V comes from the BBT breakdown [69]. The empirical formula of avalanche breakdown voltage (Equation 5.1) results in a breakdown voltage of -55 V for our InGaAs intrinsic region, which does not contradict our measurement result.

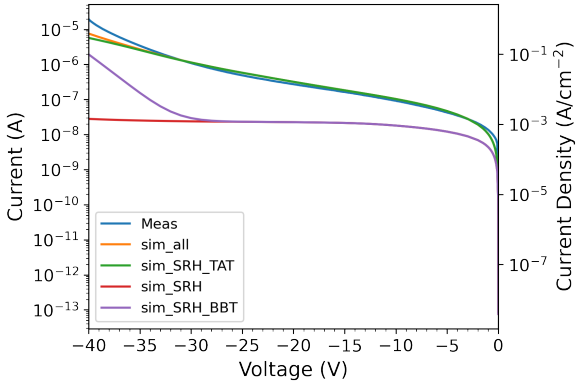


Figure 5.2: Current voltage characteristics of a fabricated InGaAs p-i-n mesa device and simulated current voltage curve fitted with the measurements. The figure also shows the individual dark current mechanisms as well as the combined effect. The best fit was achieved when all three dark current mechanisms were included and the carrier lifetimes of holes and electrons were taken as 10 ns ($\tau_n = \tau_p = 10$ ns). Meas is the measured device current, SRH is the Shockley-Read-Hall recombination current, BBT is the band-to-band tunneling current and TAT is the trap-assisted tunneling current. The orange curve shows the total simulated current from combined contributions of SRH, TAT and BBT.

$$V_B = 60(E_g/1.1)^{1.5}(N_D/10^{16})^{-0.75} \tag{5.1}$$

Table 5.1: Device identification (ID) numbers corresponding to configurations with nanowire top diameter and pitch values.

ID	**Diameter**	**Pitch**
1	280 nm	700 nm
2	350 nm	900 nm
3	340 nm	1400 nm
4	275 nm	800 nm
5	330 nm	900 nm
6	345 nm	1200 nm
7	270 nm	900 nm
8	290 nm	900 nm
9	310 nm	900 nm

Next, we characterized the current-voltage behavior of the InGaAs p-i-n photodiodes based on nanowire arrays using the probe station and semiconductor parameter analyzer. The current-voltage curves from the devices of cells E, F and I are shown in Figure 5.3. Each cell contains 9 devices with varied nanowire array geometry with nanowire top diameter and pitch values depicted in Table 5.1. In general, a good diode rectification ($>10^4$) is observed in the majority of the devices provided that the nanowire devices are fully made out of InGaAs unlike commercial InGaAs photodiodes where only the bulk intrinsic region is InGaAs and the buffer regions are InP. Buffer regions of wider bandgap materials minimizes the diffusion current in commercial devices. In the nanowire devices, the diffusion current is inherently reduced thanks to the nanowire geometry as the top buffer and large part of the intrinsic region only constitute a very small volume as compared to bulk devices. However, a higher dark saturation current was observed in nanowire devices than planar devices. We attribute this to the surface leakage current due to the high surface to volume ratio of the nanowires. In principle, the overall dark current is expected to decrease due to the reduced fill factor of the nanowire devices. Nonetheless, the low bandgap of InGaAs, the nanofabrication induced sidewall defects as well as presence of the intrinsic region at the nanowire base significantly increases the surface area, hence, giving rise to a strong surface leakage. The leakage current can be reduced by extending the nanowires across the entire intrinsic region and ending after the n-doped region. This modification would ensure that the surface area between nanowires is in the n-doped region, which is not depleted, thus, the surface area of the active region is minimized. Secondly, an optimized surface passivation strategy can significantly eliminate surface leakage [89].

The device characteristics with respect to their location in the sample is investigated. The devices at the center of the wafer chip (cell E) (See Figure 5.1d) showed consistent results within an order of magnitude even though they possess varied nanowire array geometries. The devices that are closer to the edge exhibited more variation in terms of the dark current. In cell F, only the device F3 showed high dark current in the range of mA, where others are within the nominal range of current values that are in the range of a few hundreds of μA. In cell I, three devices (I3, I6 and I9) had slightly higher dark current at reverse biases and a low voltage dependence as compared to other samples within the same cell. A higher rise of current at the smaller voltages indicate the existence of a dominant leakage path (Shunt path) that reduces the sensitivity of the photodiodes. In contrast, I8 showed an unexpectedly low dark current under reverse bias but also showed a low forward bias current, suggesting that the current is limited by the high contact resistance, which most likely arose from improper removal of SiO_2 with BOE. Similarly, device F4 had a much higher contact resistance value as seen from the forward bias current in the vicinity of 1V. In Figure 5.3d, the dark current voltage curves from a different sample that had been

processed with 5 cycles of digital etching is presented. Even though the magnitude of the current and the ON/OFF ratio is slightly improved, the current had a stronger dependence on the voltage bias signaling a stronger existence of surface caused trap-assisted tunneling. 5 cycles of digital etching possibly degraded the surface quality of the nanowires, which is also supported by the low external quantum efficiency of those photodiodes.

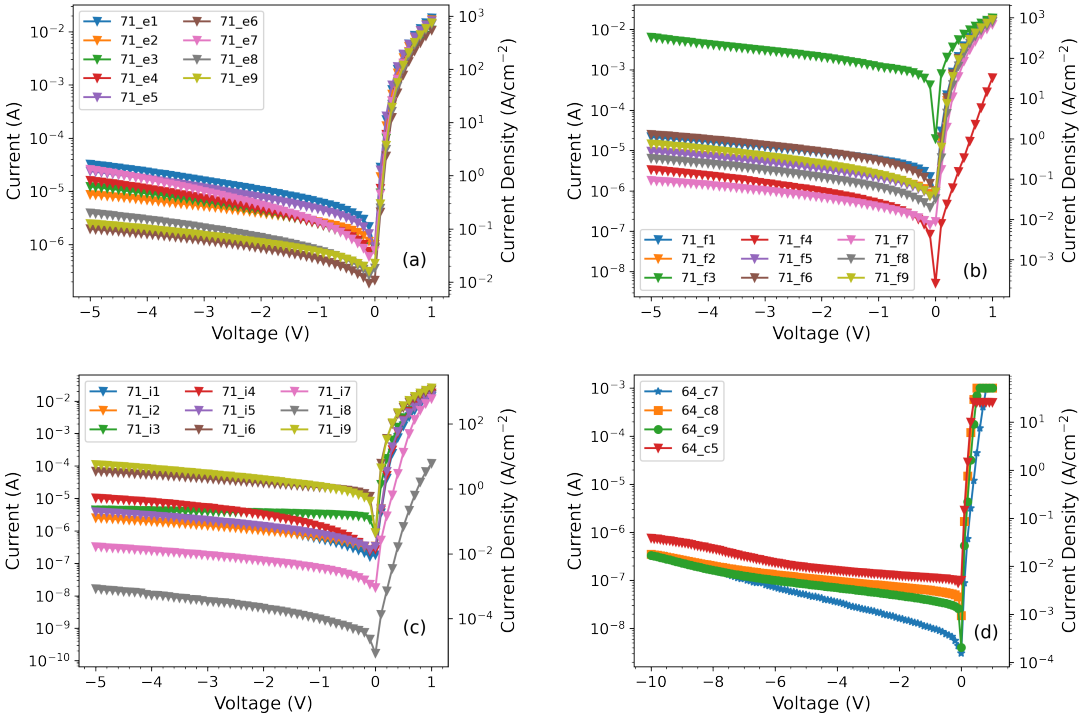


Figure 5.3: Current-voltage characteristics of fabricated nanowire array photodiodes based on InGaAs p-i-n structure. Cells E, F and I from Chip 71 were measured. a) Devices from cell E that is located at the center of the chip. b) Devices from cell F. c) Devices from cell I. The position of each cell can be seen in Figure 5.1. d) Devices from chip 64 using the same fabrication recipe as chip 71 except with 5 cycles of digital etching. Only 1 cycle of digital etching was applied to chip 71.

The measured forward bias current of the InGaAs nanowire array p-i-n photodiodes is shown in Figure 5.4a. The device E2 has a turn-on voltage of ∼0.4V, which can be estimated by the x-axis crossing of the current when extrapolated backwards from the quasi-linear high current region. We extracted the series resistance of ∼35 Ω from the slope of the forward current at high bias. Similarly, we found a Shunt resistance of ∼12 KΩ from

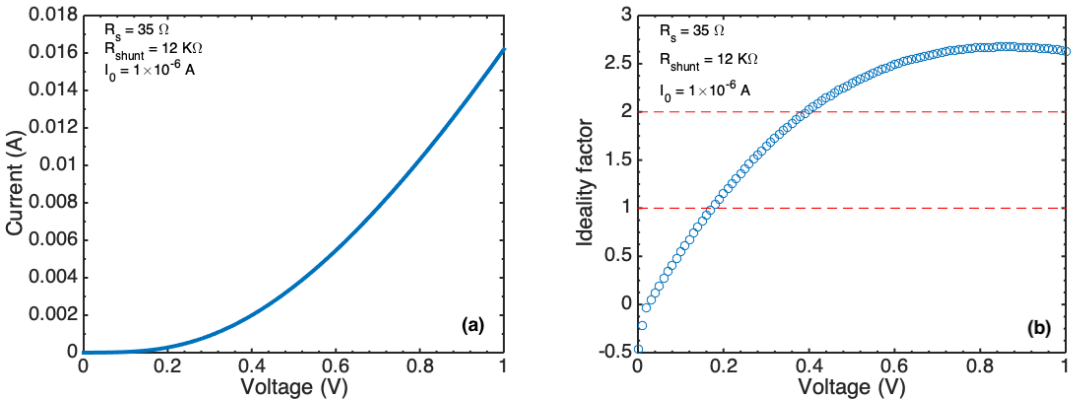


Figure 5.4: Forward bias characteristics of InGaAs nanowire array p-i-n photodiode (Chip 71 - Cell E - Device 2 corresponding to a nanowire top diameter of 350 nm and separation of 900 nm). a)Forward bias dark current of the InGaAs p-i-n nanowire array (E2). Series resistance, shunt resistance and saturation current is extracted from dark current sweeps b) Extracted diode ideality factor as a function of voltage bias. An ideality factor of 1 represents an ideal diode where the current is strictly governed by diffusion. An ideality factor of 2 points out that the diode current is governed by thermally generated carriers in the depletion region. A higher ideality factor signals that additional dark current mechanisms are present that contribute to the device current such as leakage current and series resistance.

the slope at zero volts. The shunt resistance, which is the parallel leakage path between the anode and cathode of the photodiode, is found to be very low. We believe it is very low because there is a leakage path caused by the nanowire surface or there is another leakage path associated with the chip sidewall. To better understand the forward bias current voltage characteristics of the diode we extracted the effective ideality factor n described by the Shockley Equation 5.2. The equation includes the effect of the series resistance of the diode as well as the shunt resistance since those parameters are non-negligible in our nanowire array based InGaAs p-i-n photodiodes. We plotted the extracted ideality factor as a function of voltage bias using Equation 5.2. Typically, the ideality factor is between 1 and 2, where 1 shows that the forward bias current is dominated by diffusion current, whereas 2 indicates that the current is dominated by thermal recombination and generation. Values above 2 (which can only be found experimentally) arise from other non-idealities such as the high contact resistance or high defect density. Our diode showed a typical diode behavior between 0.2 to 0.4 V but the ideality factor increases with voltage, which points to the surface defects [142]. After 0.5 to 0.6 V, the series resistance decreases

the slope of the current, hence, the n starts to drop again. The region up to 0.2 V indicates that the shunt resistance dominates the current, which can also be considered as below the turn-on current. The Shockley equation that describes the forward bias diode current is

$$I = I_0\left(exp\left[\frac{q(V - IR_s)}{nkT}\right] - 1\right) + \frac{V - IR_s}{R_{shunt}}, \tag{5.2}$$

where I_0 is the diode saturation current, q is the elementary charge, V is the diode voltage, I is the diode current, R_s is the series resistance of the diode, k is the Boltzmann constant, T is the temperature, n is the diode ideality factor and R_{shunt} is the Shunt resistance (leakage resistance).

5.2.1 Dark current improvement after cleaving the edges

An interesting finding showed that the same devices when measured before and after trimming the edges of the wafer chip demonstrated a significant improvement in the diode quality as shown in Figure 5.5. Before cleaving, the diode currents saturated at very low voltages, then showed only a weak voltage dependence. The resulting ON/OFF ratio was found to be around 10^2 and saturation current values were above 50 μA at -5V. After cleaving; however, the diode behavior notably improved. The reverse bias dark current dropped more than 100 times while the forward bias current stayed almost the same. The resulting ON/OFF ratio rose to more than 10^4. In addition, a slow current rise behavior replaced the behavior of a strong current rise at low voltages. The improved current trend is similar to standard mesa devices we fabricated as well. The origin of how the leakage path changes significantly, even at the devices in the center of the chip, is not known and needs more investigation. One possible reason to create this leakage path is that the silver paste can overflow the sidewalls during chip bonding to the ceramic chip carrier. Another possible reason could be the existence of a built-in electric field that spans the entire chip to the sidewalls since the nanowires are not etched all the way through the intrinic region to the n-doped region.

5.2.2 Nanowire diameter

Current-voltage sweeps were performed on InGaAs p-i-n nanowire array photodiodes with varying nanowire diameters to assess the effect of the nanowire size on the dark current. Devices with nanowire diameters of 270 nm (F7), 290 nm (F8), 330 nm (F5) and 350 nm (F2) were chosen with the same pitch of 900 nm for a fair comparison. The active area

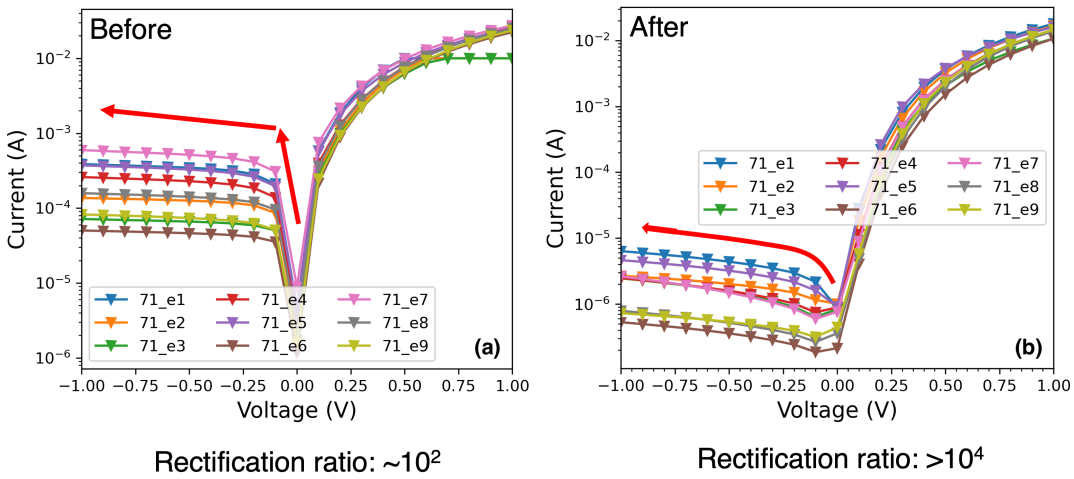


Figure 5.5: The effect of cleaving the sidewalls of the chips on the diode performance. Current voltage characteristics of InGaAs nanowire p-i-n device with 350 nm diameter and 900 nm pitch (71E2). a) Before the sidewalls of the wafer chip were cleaved. b) After the sidewalls of the wafer chip were cleaved. The ON/OFF ratio rose from 10^2 to 10^4 after cleaving. The characteristic of the dark current also changed from a step-like increase to a more gradual increase resembling closer to the mesa InGaAs p-i-n test device.

for each device is constant (50 μm). As a result, each device contains different number of nanowires. F7, F8, F5 and F2 devices contain 2400, 2398, 2388 and 2387 nanowires, respectively. We can assume that the junction cross section is the top facet area of each nanowire. If that's true, we can calculate the total junction area of the diodes by multiplying the area ofthe individual nanowires by the total number of nanowires. Therefore, the calculated area of each configuration is 549.65 μm^2, 633.57 μm^2, 816.98 μm^2 and 918.63 μm^2, respectively. In comparison, a typical mesa type diode with 50 μm diameter has a larger junction area of 1963.50 μm^2. However, defining a junction area is not trivial for nanowire array based devices. Instead it makes sense to use the top facet surface area of the nanowire as the junction area. However, the unique nature of the nanowire array photodiodes in this study makes defining the contact area difficult. The truncated cone shape of the nanowire, 3 dimensional interface between the InGaAs nanowire tip and ITO, and, most importantly, the architecture of the device (base of the nanowires being part of the intrinsic absorption layer that may generate surface recombination generation current as well as surface conduction current) all increase the complexity of the definition of a proper junction area. Furthermore, the depletion region does not extend linearly with increasing

voltage because the nanowires and bulk InGaAs collectively forms the total active region. Typically, an effective device area is defined by the total area of the device including the empty space between the nanowires for nanowire array based diodes. Therefore, we have included the calculated current density (assuming the device diameter is 48 μm) in the following plots. Similar discussion for nanowire array photodiodes is found in the literature [142].

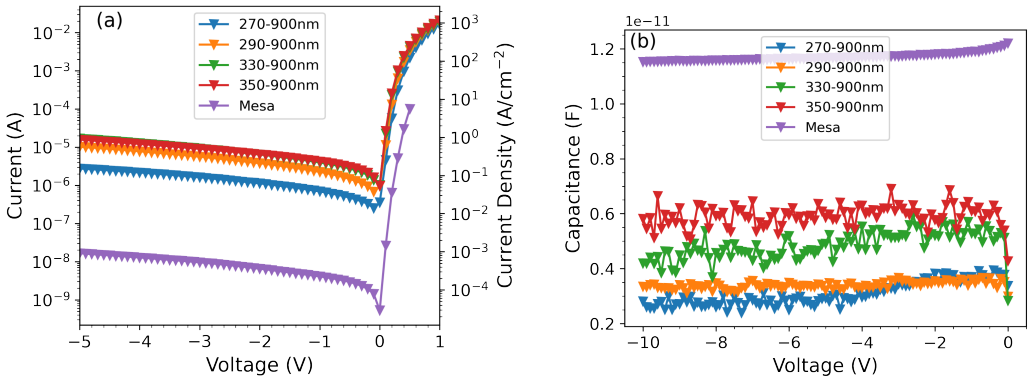


Figure 5.6: Comparison of diode dark current and capacitance curves of devices with different nanowire geometry. The effect of nanowire diameter on the a) dark current and b) device capacitance. The devices with smaller nanowire diameter exhibited a lower dark current and lower capacitance.

Figure 5.6a shows the dark current sweeps of the chosen configurations above. The magnitude of the current is found to decrease with smaller nanowire diameter. Understandably, the smaller nanowire core allows less current to flow. Moreover, the surface area of the nanowires decrease with smaller diameter further contributing to the reduced current that is observed. It should also be mentioned that the total device area should also include the base plane of the nanowire arrays since the base plane is still the intrinsic region, which is part of the active volume of the device. The nanowires having a smaller diameter leads to an increased area of the base plane; however, the total device area is still dominated by the nanowire surface area. Moreover, we can assume that the total number of defects reduces as compared to bulk devices when the fill factor decreases. Therefore, the overall diode current decreases as expected with smaller nanowire diameter. We can also deduce from the trend of the current that the bulk conduction is still more dominant than the surface conduction. This is because the device volume decreases faster than the surface area increases. It should be noted; however, that the surface conduction cannot be neglected completely since InGaAs is known to suffer from surface defects and dangling

bonds due to its small bandgap [70, 89], and our InGaAs nanowire devices did not go through an optimized surface passivation strategy. There are techniques to improve the surface quality up to a bulk level [89], which needs to be explored to improve the device quality.

Figure 5.6b shows the capacitance measurements of InGaAs p-i-n devices with different nanowire diameters and the mesa InGaAs p-i-n device for comparison. Nanowire devices had at least two times (at most 4 times) lower capacitance as compared to the mesa device when measured with a 30 mV AC signal with a frequency of 1 MHz. Even though we expect the nanowire devices to have a much smaller capacitance than the mesa devices, they are relatively close since the contact pads of the nanowire devices are large (250 μm squares) as compared to the mesa devices (150 μm squares). The nanowire device capacitance can be reduced significantly in the future by smaller contact pads and is expected to be much smaller than the mesa devices.

5.3 Photocurrent of InGaAs nanowire photodiodes

After the dark current characteristics, we investigated the photodetection properties of the fabricated InGaAs nanowire array p-i-n photodiodes at room temperature. Firstly, a tunable Ti:Sapphire (Ti:Sa) laser is used for an excitation source to measure the photocurrent between 700 nm and 1000 nm. The output laser beam is focused onto the 50 μm diameter device area. The current voltage sweeps were repeated with and without light excitation at 900 nm (and 895 nm) to characterize the photoresponse. The corresponding dark and photocurrent are plotted up to -8V reverse bias in Figure 5.7 for devices with a nanowire geometry of 350 nm in diameter and 900 nm pitch (E2, Figure 5.7a) and 310 nm in diameter and 900 nm pitch (H9, Figure 5.7b). E2 was chosen since it had the best optical absorption profile (see Chapter 3) and H9 was chosen since it had good diode characteristics with an ON/OFF ratio of 1.37×10^5 and low dark current saturation under reverse bias (-34.29 nA at -5V). At -8V bias, the photocurrent of E2 is 2.46 times the dark current with 2.45 μW average excitation at 900 nm, whereas the photocurrent is 6.78 times larger than the dark current for H9 with 1.15 μW optical power at 900 nm. The sensitivity of the photocurrent is higher in H9 due to the lower dark current. However, the generated photocurrent is 5.56×10^{-7} A in H9, which is equal to an EQE of 56.7% as compared to 2.77×10^{-6} A for E2, corresponding to an EQE of 92.5%. The lower EQE of H9 as compared to E2 is attributed to improper removal of SiO_2 and smaller device contact area at the nanowire tip before the ITO contacts were deposited. It was also found that the BCB thickness is typically higher close to the edges of the samples as compared to the

center. As a result, H9 devices have a much dark lower current as compared to the center devices with the same nanowire geometry. Furthermore, the devices showed no saturation in current behavior up to -8V bias.

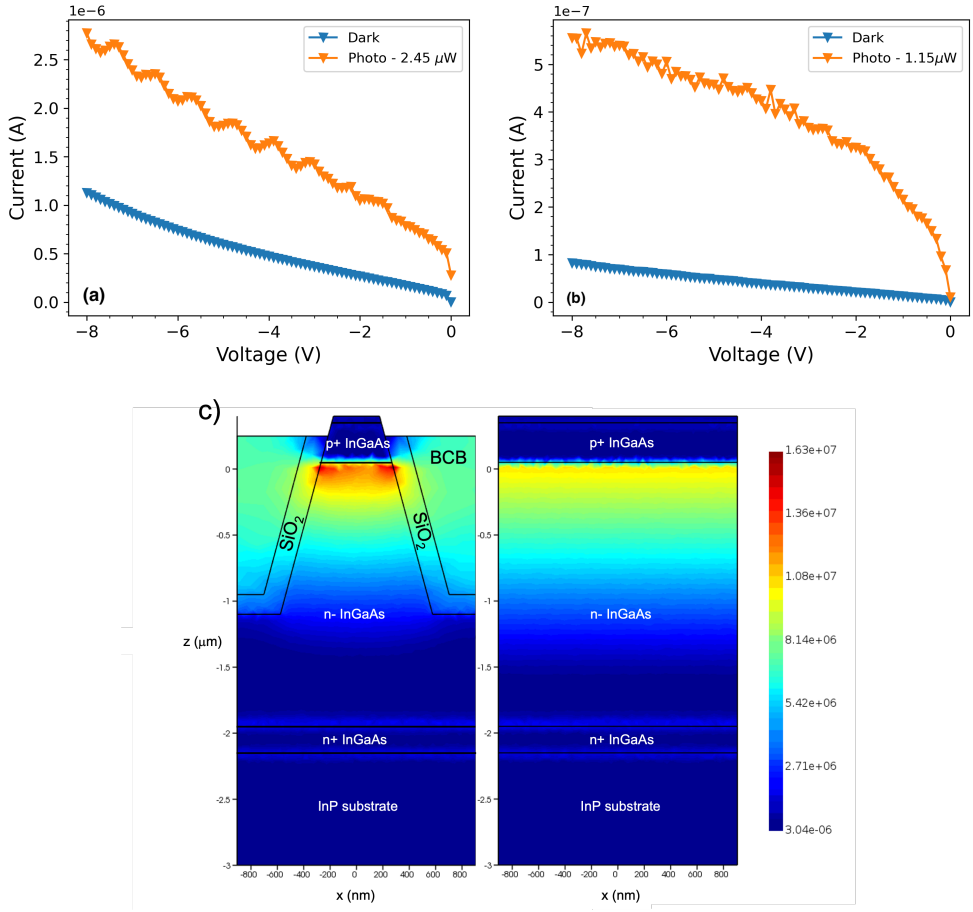


Figure 5.7: Photo and dark current measurements of InGaAs p-i-n photodiodes. a) Device E2 (350-900nm) located at the center of the chip. E2 has the best optical absorption profile, which is discussed in Chapter 3 b) Device H9 (310-900nm) located close to the edge of the chip. H9 has the best diode dark current-voltage characteristics with an ON/OFF ratio of 1.37×10^5 and low dark saturation current of -34.29 nA at -5V. c) Electric field simulations of a nanowire p-i-n photodiode (left panel) and planar p-i-n photodiode (right panel). The nanowire p-i-n photodiode has a distinct electric field profile as compared to the planar device even though the stack layer for both devices are the same.

Figure 5.7c displays the simulated electric field profile of the tapered InGaAs p-i-n nanowire array (left panel) and a planar device (right panel) with the same device layers and thickness both biased at -8V. In both the nanowire and planar devices, punch-through is not yet observed at -8V, which supports the experimental observations. However, the electric field profile has distinctive features in the nanowire device as compared to the planar device. The electric field at the p+/n- junction in the nanowire device has a much higher electric field intensity (1.63×10^5 V/cm) as compared to the planar device (1.08×10^5 V/cm). Also, the electric field distribution is much wider in the planar device than the nanowire device. It was also observed from the simulations that the nanowire device punch-through is reached at -18.5V (Figure 5.8), whereas the punch-through is observed at -11V in the planar device. Electric field intensities obtained in the nanowire devices at -18.5V may also give rise to avalanche gain and tunneling current.

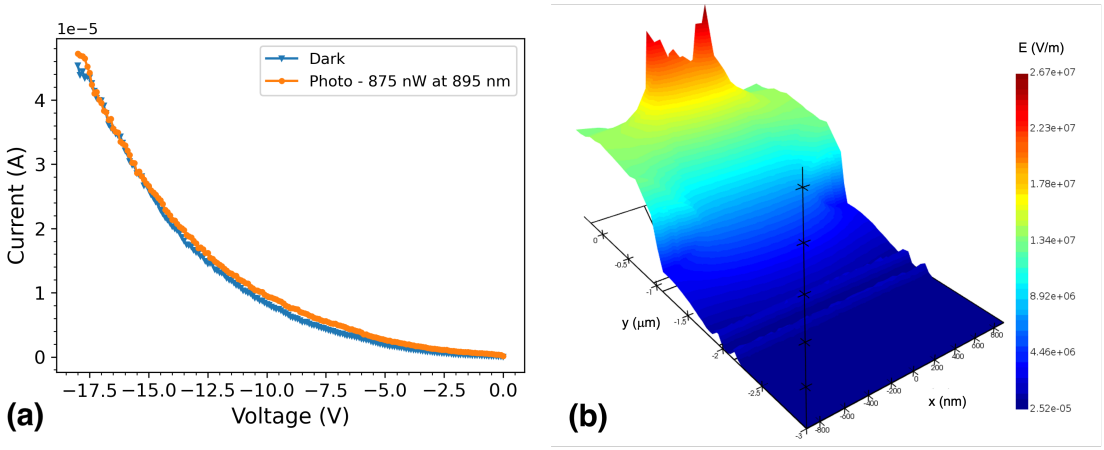


Figure 5.8: Gain mechanism in InGaAs p-i-n photodiodes. a) Dark and photo current (illuminated with 875 nW Ti:Sapphire laser at 895 nm wavelength) measurement of 330-900 nm device from cell E (E5) up to -18V. The calculated quantum efficiency at -18V is found to be 287%, clearly indicating the existence of avalanche gain. b) Simulated three dimensional surface plot of the electric field profile inside of the InGaAs nanowire p-i-n photodiodes. The electric field intensity at -18.5V reaches above the breakdown field of 2×10^5 V/cm [84, 61] at the p+/n- junction at the top of the nanowire. The device went under catastrophic breakdown at -19 V. The devices were measured at room temperature.

The extracted external quantum efficiencies at -8V are found to be very high for an InGaAs photodiode at an optical excitation of 900 nm. Also, nanowire devices did not exhibit any saturation behavior up to -8V. We have measured the dark and photo current

of device E5 up to -18V bias to further inspect the gain mechanism as shown in Figure 5.8a. The current behavior is found to have a breakdown-like characteristics where both dark current and photo current is increasing with a non-linear trend. The calculated external quantum efficiency is found to be 287% at -18V exhibiting record high values when illuminated with a wavelength 895 nm. The high value of EQE suggest the existence of a gain mechanism that gives a boost to the quantum efficiency value. Electric field simulations were performed to find the electric field intensities at -18V as displayed in Figure 5.8b. According to the simulation, the electric field intensity at the p+/n- junction is 2.67×10^5 V/cm which is significantly higher than InGaAs critical field value of 2×10^5 [84].

5.4 Spectral responsivity of InGaAs nanowire photodiodes

The spectral responsivity of the InGaAs nanowire photodiodes were also measured using a Ti:Sapphire laser between 700 nm to 1000 nm, then FTIR was used to obtain the entire detection spectrum. For the measurement of the spectral responsivity, the optical beam was mechanically chopped at 433 Hz to perform phase sensitive measurements in order to eliminate external noise. The average power hitting the device and the photocurrent values amplified by a lock-in amplifier were simultaneously recorded. We recorded the average optical power and the photocurrent for 7s in order to filter out instantaneous fluctuations of the continuous wave (CW) mode Ti:Sapphire laser. The peak power is calculated by multiplying the average optical power measured by a Thorlabs S120C power sensor due to the 50% duty cycle. The photocurrent was recorded at each wavelength for various biases by connecting a 900 Ω resistor in series with the photodiode, then measuring the photovoltage across that resistor. The RMS photovoltage displayed on the lock-in amplifier is first divided by 900 to extract the photocurrent, then multiplied with $\sqrt{2}$ in order to find the peak photocurrent. Next, the responsivity is calculated by dividing the peak photocurrent by the peak optical power. The responsivity and the corresponding EQE values were measured and calculated at various voltage biases as shown in Figure 5.9. As expected, the responsivity kept rising as the bias is increased. The depletion region extends rather unconventionally in nanowire devices as the depletion region has to spread horizontally as well as vertically due to its unique nanowire shape and base. Therefore, the electric field profile scales differently as compared to bulk devices. This, in return, changes the typical saturation of the devices. Therefore, we can see that the responsivity does not fully saturate up to -8V. We achieved remarkable responsivity values between 700 nm to

1000 nm. At 900 nm, the responsivity is 0.7 A/W, corresponding to an EQE of 91.9% with -8V bias. A maximum responsivity was achieved at 950 nm with a value of 0.73 A/W, corresponding to an EQE of 92%. In typical bulk InGaAs photodiodes, the EQE values are very low in the valley of death around 800 nm due to the fact that the photons are absorbed close to the surface. In such cases, the majority of the photogenerated electron hole pairs recombine due to surface trap centers. In contrast, in nanowire devices, the optimized shape and the ITO dome for contacting [143] enable efficient absorption in the depletion region, thus minimizing surface recombination. As a result, very high EQE values were achieved.

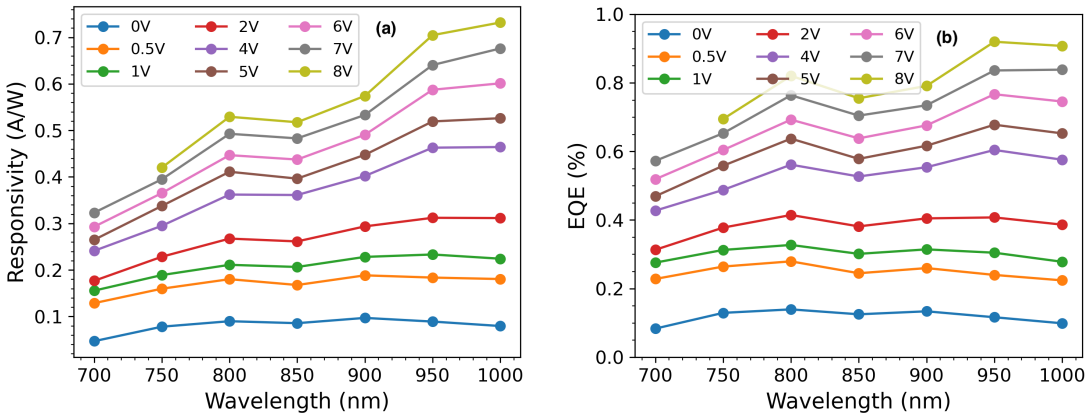


Figure 5.9: Measured a) spectral responsivity and b) external quantum efficiency of the InGaAs nanowire p-i-n photodiodes with nanowire top diameter of 350 nm and pitch of 900 nm (71-E2). The measurement was performed using a Ti:Sapphire laser from 700 nm to 1000 nm with 50 nm steps for biases from 0 to -8V. The optical excitation is mechanically chopped at 433 Hz and the photocurrent is measured with a phase sensitive lock-in amplifier. The devices were measured at room temperature.

We extracted the full responsivity spectrum by measuring the photocurrent with FTIR system. The recorded responsivity values with the Ti:Sapphire was used to calibrate the FTIR results, which provided data points to calibrate the spectrum from arbitrary units in the FTIR output. Figure 5.10 shows the resulting spectral current for the three different devices. We plotted the normalized spectra of E2, E5 and H9 to be able to compare the photocurrent profiles. For normalization, we divided the photocurrent at each wavelength value by the maximum photocurrent value in the whole spectrum. At -5V bias, the long wavelength response of H9 drops earlier than E2 and E5, while device E2 extends more to the longer wavelengths. The result is consistent with the optical absorption efficiencies of

the nanowire diameter as discussed in Chapter 3. The larger nanowire diameter results in better optical coupling for longer wavelengths, therefore, the responsivity/EQE increases while shorter wavelength absorption efficiencies appear to be the same.

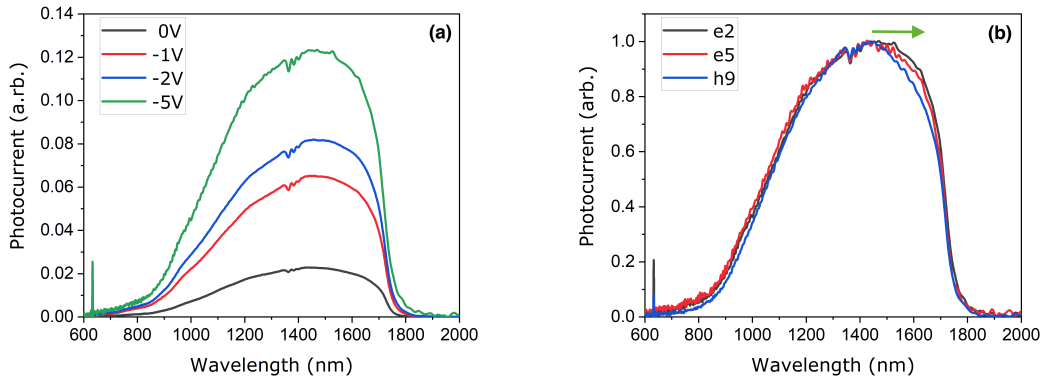


Figure 5.10: Photocurrent measurements with the Fourier-transform infrared spectroscopy (FTIR) system. a) Spectral photocurrent measurements of device 71E2 at 0V, -1V, -2V and -5V biases. b) Spectral photocurrent curves of devices E2, E5 and H9 normalized to their maximum current point and displayed together. The photocurrent cut-off is shifting to the longer wavelengths with a larger nanowire diameter device. The devices were measured at room temperature.

The responsivity extracted from the FTIR measurement data calibrated with the Ti:Sapphire laser measurement are displayed in Figure 5.11. The responsivity of the device rises sharply starting at 700 nm and reaches a plateau around 900 nm, then remains relatively constant until it drops at 1800 nm. The calculated responsivity measurements agree very well with the FTIR based responsivity. The device is even responsive at zero bias and exhibits decent responsivity values showing great potential for unbiased photodiodes. The calculated EQE from the responsivity shows a decaying performance as the wavelength increases, which is also observed in many InGaAs based bulk photodiodes. The efficiency goes down since the absorption coefficient decreases at longer wavelengths. Also, the absorption profile in nanowires at longer wavelengths suggests that the absorption location is more spread as compared to shorter wavelengths and there is more weakly guided modes at the surface. The absorption close to the surface possibly lowers the efficiency due to surface recombination. The FTIR measurement response around 800nm is noisy and behaves dissimilar to the laser measurements. This is believed to arise from the low responsivity of reference photodiode used for the measurements (See Appendix). The minuscule deviation

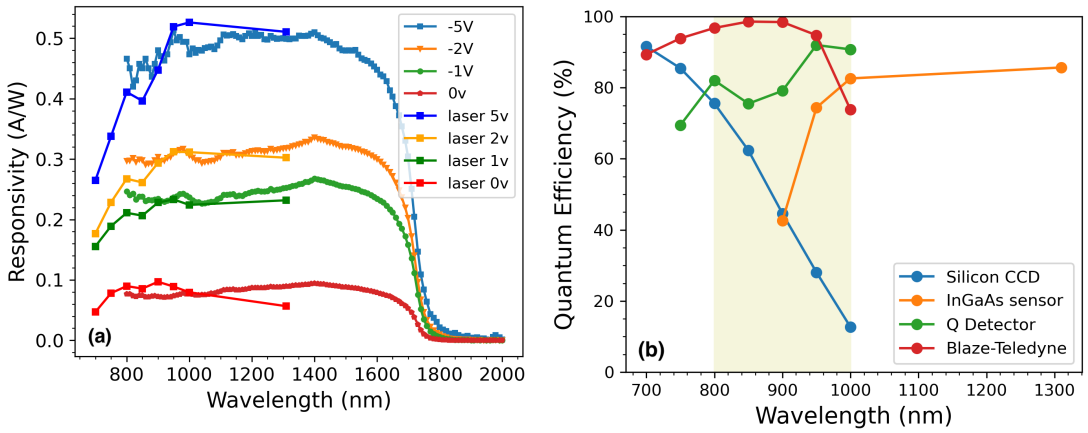


Figure 5.11: Calibrated InGaAs nanowire array p-i-n photodiode spectral responsivity using Ti:Sapphire laser and Fourier-transform infrared spectroscopy system and comparison of external quantum efficiency with commercially available sensors. a) Spectral responsivity calculated by the Ti:Sapphire laser was used to calibrate the photocurrent spectra with Fourier-transform infrared spectroscopy. b) Quantum efficiency of our InGaAs nanowire p-i-n photodiodes (Q Detector) as compared to the existing technologies in the near infrared wavelength range. The devices were measured at room temperature.

of the results may arise from the 7% and 5% uncertainties of S120C (Si) and S122C (Ge) Thorlabs photodiode power sensors when measuring the power of the optical excitation.

In many commercially available InGaAs photodiodes, the substrate side is used for optical excitation. The Beer-Lambert law suggests that the absorption coefficient is higher at shorter wavelengths. As a result, the materials have higher absorption coefficients at lower wavelengths. Therefore, the light is absorbed close to the surface, and surface recombination wipes out the majority of the generated electron-hole pairs. Moreover, the devices typically contain heavily doped buffer layers with limited depletion length penetration at the top. Since the shorter wavelength light excitation absorbed close to the surface there is no built-in electric field to sweep the electron hole pairs. Thus, the absorption coefficient of the material determines the lowest wavelength that can be detected that limits the detection range.

Our detectors overcome this limitation. The optical absorption is funneled and focused into the bulk of the nanowire at shorter wavelengths. Properly designed location of the p-n junction takes care of the electron-hole pairs by successfully separating them before they recombine. Therefore, our detectors show a remarkable result, especially between 800 nm

to 1000 nm. For comparison, the quantum efficiencies for three state-of-the-art photodiodes (Si CCD, Blaze-Teledyne and InGaAs [144]) are plotted in Figure 5.11. These detectors are cooled to achieve the high quantum efficiency, yet both systems fell short in the region what is also known as the "Valley of Death". The Si detector efficiency drops because of the indirect bandgap of Si leads to inefficient capturing of long wavelength photons. In contrast, InGaAs suffers from high surface recombination as well as Fresnel reflections from the material-air interface leading to poor absorption below 950 nm. Back illuminated InGaAs devices typically have a sharp cut-off at 930nm as they are unable to detect photons at shorter wavelengths. The quantum efficiency of the InGaAs nanowire array photodiodes exceed these limitations by employing the nanowire geometry to significantly improve the forward scattering and collective nature of the nanowire array metamaterial design to enhance the light coupling and absorption. The absorption takes place at the depletion region, which then effectively sweeps the carriers thanks to the built-in electric field.

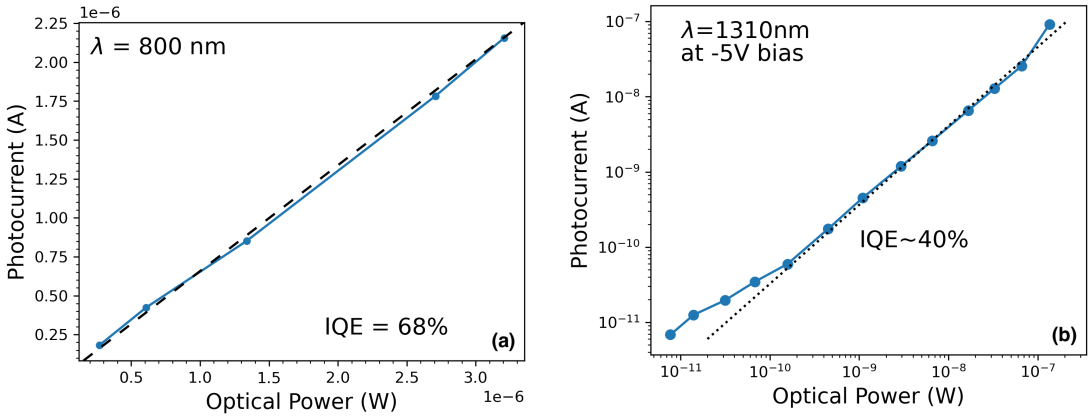


Figure 5.12: Internal quantum efficiency of InGaAs nanowire array p-i-n photodiodes. a) Measured photocurrent of the InGaAs nanwoire array p-i-n photodiode biased at -5V when illuminated with a 800 nm laser for varying optical powers. Internal quantum effficiency is extracted as 68% at 800 nm. b) Measured photocurrent of the InGaAs nanwoire array p-i-n photodiode biased at -5V when illuminated with1310nm for varying optical powers. The internal quantum efficiency is extracted as 40%. The device was still responsive to the optical power below 10^{-11} W but reaching to its noise floor as can be observed from the deviation from linearity at low optical powers below 10^{-10}. The devices were measured at room temperature.

Moreover, the internal quantum efficiency of the nanowire arrays was investigated.

The photocurrent is recorded at various optical excitation powers when biased with -5V at 800 nm (Figure 5.12a) and 1310 nm (Figure 5.12b). The photocurrent in both cases follow a linear trend demonstrating the wide dynamic range of the device. By looking at the slope of Figure 5.12a, the quantum efficiency can be successfully estimated provided that there is no gain in the device. The slope yields an IQE of 68% at 5V reverse bias. This value agrees well with the Ti:Sa laser measurements. Therefore, the result increases the confidence on the device measurements. In Figure 5.12b, the device response was investigated until the phase sensitive response reaches to the noise floor of the photodiode. At the lowest measured power, the device can detect an optical signal with power of 7.7 pW at 1310 nm with an optical chopper frequency of 433 Hz. The load resistor is 903 Ω. The corresponding NEP power is 3.7×10^{-13} A/$\sqrt{Hz}$. We have to note that this value is not necessarily the ultimate minimum detected power, rather the power where the lock-in amplifier phase lock started to fluctuate. In addition, the modulation frequency is low as compared to the nominal operation frequencies above a few hundreds of MHz to make a final conclusion.

Chapter 6

Nanowire array avalanche photodiodes

Chapter contributions: Lin Tian, Nachiket Sherlekar and Francois Sfigakis assisted with temperature based optical electrical measurements. Man C. Tam and Zbigniew Wasilewski performed thin film growth of InGaAs-InAlAs.

6.1 Device fabrication

The fabricated InGaAs/InAlAs nanowire arrays are displayed in Figure 6.1. The recipe used for ICP-RIE etching of InGaAs produces the same nanowire geometry for InGaAs-InAlAs layer stack. One difference was related to surface oxidation of InAlAs due to its Al content. During surface cleaning, before SiO_2 passivation, O_2 asher plasma resulted in crystal formation at the surface which wasn't encountered in InGaAs nanowire fabrication. The cause of that crystal formation is believed to originate from oxidization prone Al atoms at the surface. Those crystals and the residue of SiNx hard mask were cleaned after ICP-RIE etch process with BOE (10:1) dip for 8 minutes. The devices were inspected until the surface was clear from crystals and residue. The remaining steps of the device fabrication followed the same recipe developed for InGaAs pin nanowire devices.

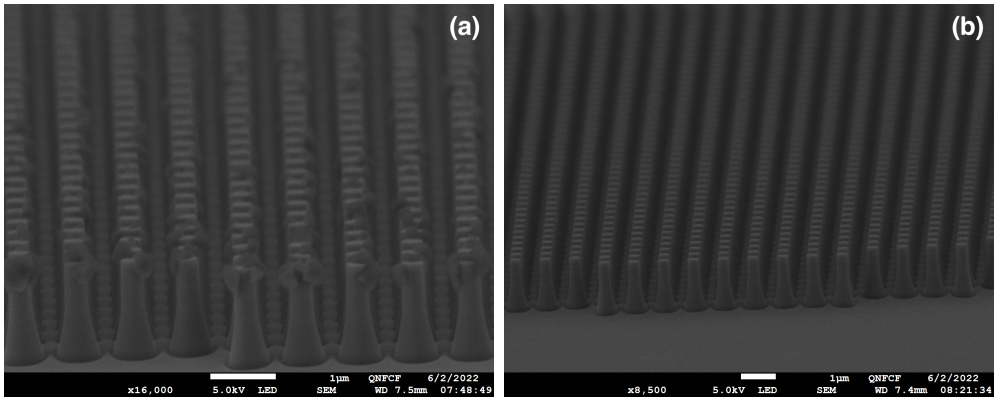


Figure 6.1: SEM images of fabricated InGaAs/InAlAs nanowire array. a) Oxidization step in digital sidewall etching led to formation of oxide crystals at the nanowire surface. b) The formed crystals were removed with BOE (10:1) dip for 8 minutes.

6.2 Optical properties of InGaAs-InAlAs nanowires

After nanowire arrays were fabricated, we measured the optical properties of the bare nanowire arrays with the same method used in Chapter 3. The resulting transmission and reflection spectra showed a similar high quality and low reflection. The absorption is estimated to be slightly lower than in bare InGaAs nanowire arrays. The InGaAs thickness in SACM configuration only is 1 μm compared to 2 μm (1.15 μm nanowire) total InGaAs layer thickness. Regardless, the remarkable near unity absorption properties ensues for the nanowires made out of InGaAs/InAlAs. It should be noted that there is 300 nm thick InAlAs buffer layer in this structure which is transparent up to wavelengths longer than 840 nm. However, the buffer layer does not seem to affect the absorption characteristics significantly. A more detailed study using FDTD simulation is needed to show the absorption profile inside the nanowire.

6.3 Device structure and dark current characteristics

The diode structure embedded in the nanowire array differs from InGaAs pin photodiode. Device architecture is separate absorption multiplication and charge layer which is the structure used in all InGaAs/InGaAsP based avalanche photodiodes. The multiplication layer is separated from the absorption layer by a heavily doped charge layer. This separation ensures high electric field in the multiplication region necessary for creating

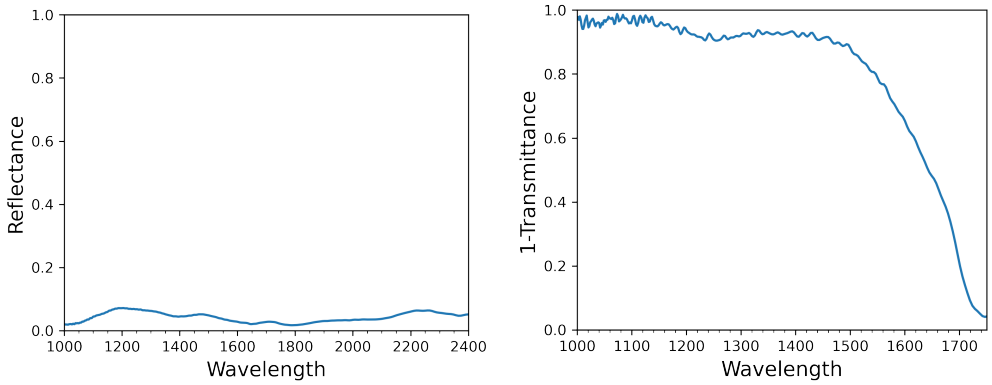


Figure 6.2: Optical properties of InGaAs-InAlAs nanowire array photodiodes. a) Optical reflection spectrum exhibiting $< 5\%$ reflection from 1000 nm to 2400nm possibly extending beyond the chosen range. b) Inverted transmission spectrum showing low transmission up to 1500nm indicating high absorption when combined with the reflection. The InGaAs height is 1000 nm in this device configuration while the total nanowire is 1500 nm long. The top diameter is 350 nm and separation is 900 nm.

strong impact ionization, as well as necessarily low (saturation velocity is still expected for optimal response time) to eliminate the possibility of band-to-band tunneling (BBT) and trap-assisted tunneling (TAT) present at high fields. Based on device simulations using Silvaco TCAD, we have optimized a single photon avalanche diode structure using InAlAs as the multiplication region material. The device architecture including the carrier concentrations in each layer as well as the corresponding electric field profile is given in Figure 6.3.

Once the wafer chip was ready, they were attached to a PCB, designed to be used in Attocube cryostat system for electrical testing at various temperatures. Measured current-voltage sweeps for three different device configurations are given in Figure 6.4. Devices showed a clear dominant avalanche breakdown characteristics up to 200K, where the Zener like breakdown took over the response. This was deduced from the breakdown voltage shift to the higher voltages when measured from 125K to 200K, then shift to the lower voltages above 200K. The breakdown voltages seem to vary among different devices (compared at the same temperatures) which is a commonly seen phenomenon in avalanche photodiodes which arises from the local defects spread non-uniformly around the wafer. The change of slope above the breakdown, although the origin is unknown could arise from surface defects.

The origin of the dark current mechanism of the avalanche photodiodes were further

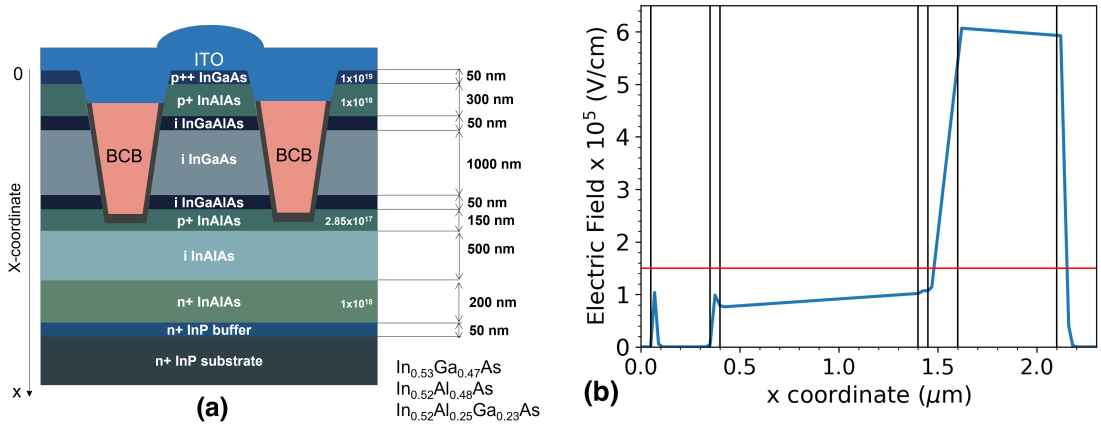


Figure 6.3: Designed separate absorption multiplication and charge layer device architecture incorporating InGaAs as the absorption region and InAlAs as the multiplication and charge layers. InAlGaAs quaternary layers are used to reduce the energy band barrier heights which would impede carrier transport. a) A schematic showing the doping density and thicknesses in each layer in the nanowire geometry. b) The corresponding electric field profile of the device at the breakdown voltage of -44V at room temperature. The electric field intensity is below the InGaAs band to band tunneling threshold which is shown with a red horizontal line.

investigated by examining the change in diode current with respect to temperature at different reverse bias voltages as shown in Figure 6.5b. The activation energy of the defect centers at a particular temperature can be extracted by the following equation:

$$I_{dark} \propto T^{3/2} exp\left(\frac{-E_A}{k_B T}\right) \tag{6.1}$$

where I_{dark} is the dark current, T is the ambient temperature, E_A is the activation energy of the trap center, k_B is Boltzmann constant. From Figure 6.5b, we fitted the Arrhenius type behavior above 225 K. The extracted activation energies from the slope of the fitted lines are found to be between 0.194 eV to 0.26 eV. These activation energy are smaller than midgap energies of both InGaAs and InAlAs, therefore, the dominant mechanism is trap-assited tunneling via trap states above 200-225 K (58-51 eV^{-1}). The same activation energy values were reported elsewhere [145]. As temperature is reduced below 200 K (above 58 eV^{-1}), the activation energy drops close to 0.1 eV, then rises back up due to avalanche gain. This figure shows a clear picture of preferred operation range of the photodiodes that the TAT current is weak. It is also apparent that the current increase rate is not linear,

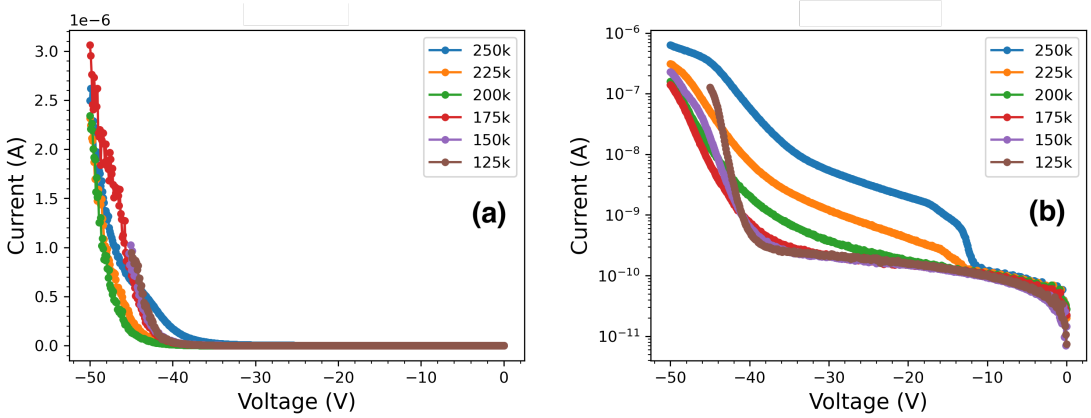


Figure 6.4: Dark current voltage characteristics of nanowire based separate absorption multiplication and charge layers avalanche photodiodes at different temperatures a) Device D2 with linear y-axis (current), b) Device F2 with logarithmic y-axis (current). The avalanche breakdown voltage shifts to higher voltages as temperature increases when the avalanche mechanism is effective, whereas, breakdown voltage shifts to smaller voltages when tunneling breakdown is dominant. The devices show clear avalanche breakdown characteristics up to 200K before the trap-assisted tunneling starts to dominate the dark current.

further indicating that the avalanche gain is present.

6.4 Avalanche gain

Next, the devices were tested under light excitation to measure the avalanche gain. For that purpose, laser diodes operating at 1310 nm and 1550 nm were used to excite the nanowire array avalanche photodiodes. In separate absorption multiplication and charge layer design, the depletion initially forms in the InAlAs multiplication region. As the bias is increased, the depletion regions extends into the InGaAs region where photogenerated carrier injection into the multiplication region starts. Figure 6.6a shows E7 that the device does not respond to light until around -18V. The voltage where depletion reaches to the InGaAs, then fully depletes the region is called punch-through voltage (V_p). In E7 device, the location of V_p is estimated to be at -20V. Then, the photocurrent starts to rise at a much rapid rate than dark current indicating the gain mechanism multiplies the photon created carriers. The corresponding gain (M) is calculated by McIntyre's formula using

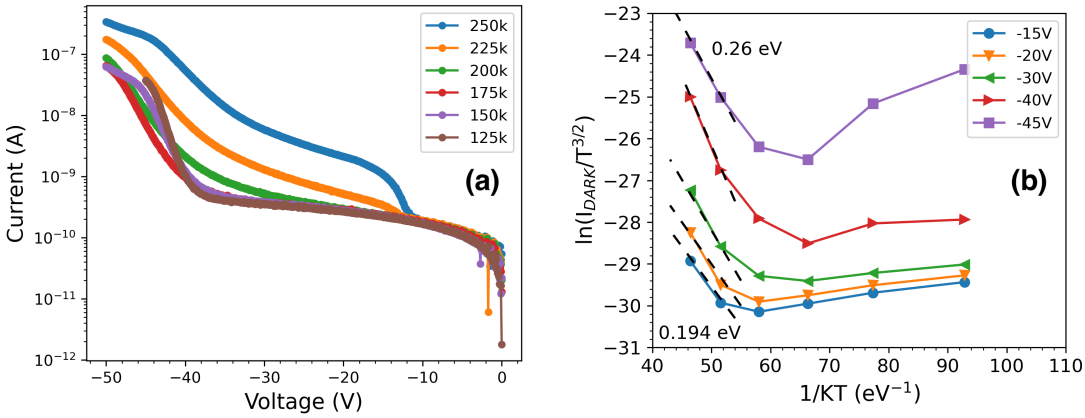


Figure 6.5: Dark current characteristics of separate absorption multiplication and change layers device architecture nanowire array device 72B-F4 with 275 nm top diameter and 800 nm pitch nanowire geometry. a) The dominant breakdown mechanism is avalanche breakdown up to 200K. b) Arrhenius plot showing extracted activation energies that highlight the dominant dark current mechanisms at various temperatures.

dark and photocurrent as follows:

$$M = \frac{I_{photo} - I_{dark}}{I_{(0)photo} - I_{(0)dark}} \tag{6.2}$$

where I is the multiplied photo current, I_{dark} is the multiplied dark current, $I_{0,photo}$ is the primary unmultiplied photocurrent and $I_{0,dark}$ is the primary unmultiplied dark current. The calculated gain up to -40V reverse bias was shown as the red curve in Figure 6.6a. The gain values are comparable to commercially avaible avalanche photodiodes working in the linear region, which is below the breakdown. We also measured the dark and photocurrent of device F4. The photocurrent is measured with 1550 nm laser source. The corresponding dark and photocurrent as well as the calculated gain is plotted in 6.6b. The punch-through voltage is reached at -23V. This time, the measurements were performed up to -45V. The gain is clearly increasing exponentially above the breakdown reaching to 40 at -45V. Both devices were measured at 100 K.

Device F2 was tested similarly under 1550 nm laser excitation for four values of average power as shown in Figure 6.7. The different power excited measurements all gave the same breakdown voltage of -45 V. Unlike the previous devices, the dark breakdown voltage in this device shifts depending on the previous measurements. After the first measurement,

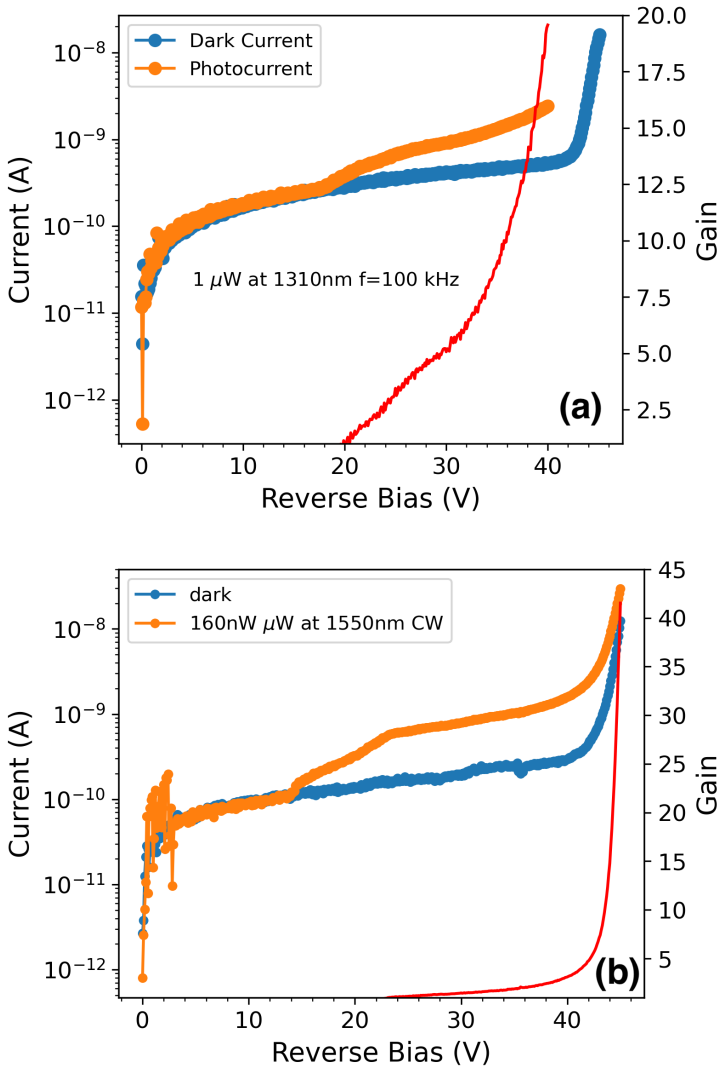


Figure 6.6: Dark and photo current characteristics of nanowire array separate absorption multiplication and charge layers avalanche photodiodes of a) Device E7 (270-900nm) illuminated with 1310 nm pulsed laser and b) F2 (350nm-900nm) illuminated with 1550 nm continuous wave laser. Gain values were extracted from the measurement results using Equation 6.2 and plotted as red curves with values displayed on the right vertical axes. The measurements were done at 100 K.

the dark current recovers and approaches to the breakdown voltage that was observed with the photocurrent measurements. In addition, the first measurement at low temperatures shows and early current rise generally starting after -25V, followed by a current saturation, then a negative resistance region. After that current rises again possibly due to gain created by the high electric field in the multiplication region. The behavior disappears after the first measurement and only returns when the device is warmed-up to room temperature. The most likely cause to that phenomenon is the surface traps between nanowire and SiO_2 interface. At room temperature, the majority of the trap levels are filled due to the thermal energy. When cooled, they are reintroduced to the semiconductor and participate in the current conduction. After the first pass, the current value goes down since the traps are filled again depleting the core of the nanowire. The original mechanism behind this strange behavior needs further investigation and is not investigated in this study.

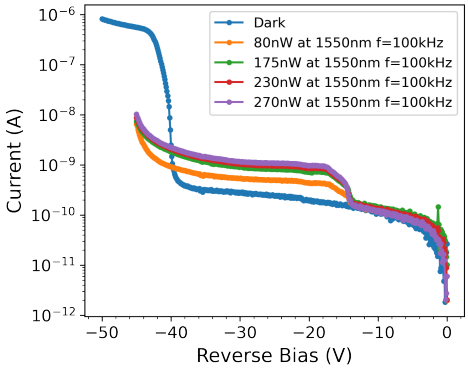


Figure 6.7: Dark and photocurrent voltage characteristics of an nanowire array separate absorption multiplication and charge layers avalanche photodiode (72-F2:350 nm - 900 nm) at 100 K excited with increasing optical powers.

6.5 Zener breakdown and microplasmas

MBE based InGaAs-InAlAs were grown to realize single photon avalanche diodes. Similar to the InGaAs devices, a set of planar large area and nanowire array devices were fabricated. Dark current voltage measurements at different temperatures resulted in a clear tunneling behavior. The data analysis on the current voltage measurements showed that the tunneling arises from the defects (trap-assisted tunneling) and is a function of growth quality. The fact that the breakdown voltage shifts to lower voltages as the temperature

increases is a clear indication of that tunneling behavior. As a result, the focus of the project shifted to obtaining low trap density wafers externally rather than optimizing the growth structure with the existing university MBE system.

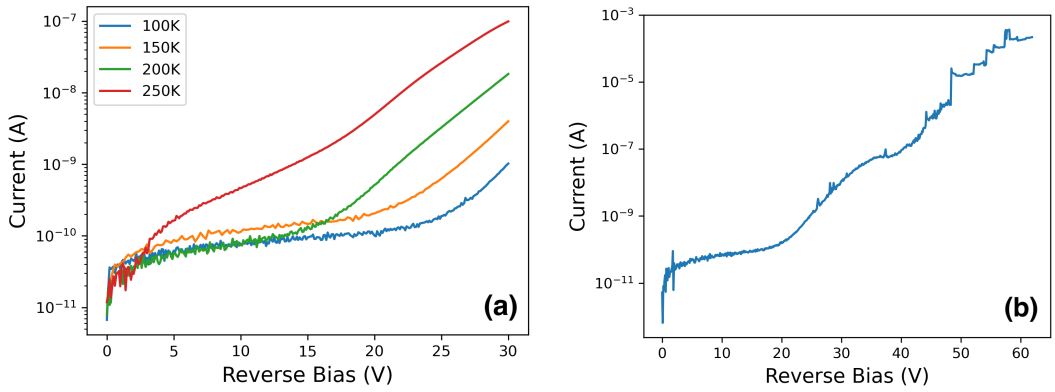


Figure 6.8: Dark current voltage sweeps faulty devices. a) A device exhibiting Zener breakdown with negative temperature coefficient. b) Microplasma behavior in a diode showing step like multiple breakdowns at room temperature.

Another observation drawn from the current voltage measurements was the existence of microplasmas, a defect related phenomenon that shows itself under high electric field. The room temperature current voltage curve exhibited that behavior distinctly as shown in Figure 6.8. The curves lacked smoothness at low voltages as can be seen from noisy behavior and rather show step like oscillations at high voltages. This property was previously observed in devices with high defect density where the defect focuses the electric field locally leading to premature breakdowns [146]. Several fabricated devices exhibited that similar behavior and many of them underwent catastrophic failure.

Chapter 7

Conclusion and future outlook

7.1 Summary of the results

In this work, we presented an approach to improve light absorption using III-V semiconductor nanowire arrays towards achieving low light detection. We specially designed a nanowire array that absorbs light in the NIR and SWIR bands two times better than bulk InGaAs with the same thickness. Devices made from nanowire arrays showed impressive quality in terms of quantum efficiency.

First, we have designed a metamaterial structure that maximizes the light absorption in the NIR and SWIR range. The metamaterial structure suppresses Fresnel reflections by efficiently scattering light dominantly in the forward direction and coupling light effectively into the waveguide modes with tapering. We optimized a nanowire geometry composed of tapered InGaAs nanowires using FDTD simulations that can funnel and absorb the light within a wavelength range from 400 nm to 1650 nm. We show that the collective resonances between nanowires as well as weakly guided modes are the reasons behind the high absorptance.

Next, a nanofabrication procedure was developed for the realization of near-unity absorptance using InGaAs nanowires. We developed and optimized a nanofabrication recipe that can create III-V nanowire arrays as close as possible to the designed structures in the simulations. The nanofabrication recipe also allows precise control over the nanowire geometry, therefore, it enables tunability of the optical response. The optimized process outputs a highly ordered, low surface roughness and high quality InGaAs nanowire arrays. Optical measurements on the optimized fabricated InGaAs nanowire arrays resulted in an average absorptance of 93% from 900 nm to 1500 nm.

Using the highly absorptive InGaAs nanowires, p-i-n based photodiodes were fabricated. The devices exhibited remarkable detection capabilities, especially in the NIR region between 800 nm to 1000 nm, also referred to as "valley of death". Fabricated devices showed an unprecedented external quantum efficiency of 79% at 900 nm under a bias of -8V and 287% at 895nm with a bias of -18V, while the commercially available Si CCDs and InGaAs sensors can only achieve 40%. The best quantum efficiency detector that works at 900 nm has 98% to the best of our knowledge (Teledyne Blaze); however, its quantum efficiency drops to 73.8% at 1000 nm, whereas, our detector has 90.8% at -8V. High quantum efficiency of the detectors and electric field simulations suggested that an avalanche gain mechanism is present in the devices. Moreover, the devices were investigated electronically in detail. A rectification ratio larger than 10^4 was achieved for the photodiodes although existence of high leakage current was observed. The dark current and capacitance of nanowire arrays with different geometry were examined.

Furthermore, the promising optical and electrical properties of the nanowires were applied to separate absorption, multiplication and charge layers based avalanche photodiodes. A SACM avalanche photodiode structure was designed employing heterojunctions consisting of InGaAs as the absorption layer and InAlAs as the multiplication and charge layer region. InAlGaAs layers were used as the grading layer to reduce band gap offsets. Next, nanowire arrays in InGaAs/InAlAs were fabricated with similar dimensions to the InGaAs nanowires. The devices exhibited avalanche breakdown with an optical gain of 40 above the breakdown voltage at -45V. The avalanche gain behavior was investigated with temperature dependent dark current measurements. The dominant dark current mechanism were extracted from Arrhenius type plot from temperature dependent dark current. The extracted activation energies pointed at the existence of trap-assisted tunneling at temperature above 200K.

7.2 Future outlook

The work covered in this thesis offers a potential improvement path towards achieving a photodetector technology exceeding the performance of commercially available devices that works in the NIR and SWIR range. Using the remarkable optical and electrical properties of tapered nanowires, the device quantum efficiency can be enhanced without losing the high speed operation. The sensitivity of the devices can be further improved by introducing the gain mechanism inside of the nanowires. The devices developed in this work could be a stepping stone towards achieving single photon sensitivity with high detection efficiency and low noise. Once the technology matures, III-V semiconductor nanowire based single

photon avalanche diodes can be a significant alternative to superconducting nanowire based detection technology without the need for cryogenic cooling. This could accelerate the development of quantum computing technology, LIDAR technology used in autonomous cars as well as satellite communication systems.

Even though nanowire arrays show great promise, there are two main challenges towards achieving high quality semiconductor nanowire array photodiodes. First, the surface quality of the InGaAs nanowires needs to be improved. The inductive coupled plasma - reactive ion etching process is known to induce defects on the nanowire sidewalls; however, reduction of induced damage is demonstrated by increasing the process temperature [132]. A similar approach could be useful. Moreover, a study on post-annealing of nanowire arrays would significantly help the current performance of the devices [147]. Second, an optimized surface passivation technique has not yet been developed in this study. For instance, there is a remarkable example of improved surface quality of InGaAs nanowires using ammonium sulfide for passivation reducing the surface recombination velocity close to bulk levels [89]. Also, atomic layer deposition (ALD) would be a great alternative system to PECVD SiO_2 to passivate the nanowire since ALD systems can achieve conformal coating with atomic layer precision for high aspect ratio nanostructures. Once the surface related defects can be suppressed, the proposed devices in this study are believed to make significant impact in the semiconductor based avalanche photodiodes market and help improvement of technologies such as quantum systems and biomedical devices.

After the device characterization, the leakage current was found to be a critical issue and it was partially eliminated by cleaving the edges of the fabricated chips. Even though the origin of that leakage current is unknown, it is clear that there is a leakage current path from the nanowires to the sidewalls. The total thickness of the intrinsic (n- InGaAs) region in InGaAs nanowire p-i-n photodiodes is 2 μm whereas the nanowire height is 1.5 μm. Therefore, it is possible that generation of carriers at the chip sidewall can find their way to the nanowire array active region under the built-in electric field. To alleviate this problem, two strategies can be applied. First, the device layer stack can be modified so that the bottom plane of the nanowire arrays becomes a highly doped current buffer region. Therefore, no built-in electric field is present at the chip sidewalls. Second, the layer stacks can be grown on semi-insulating InP wafers that will minimize the crosstalk between neighboring devices and chip sidewalls. Devices can be fully isolated by removing the layers between neighboring devices.

Another improvement that could help with high frequency measurements of the devices such as single-photon detection could be made by placing co-planar waveguides (ground-signal-ground) as the device contacts. Therefore, a 50 Ω matched transmission line would minimize the losses of high frequency signal detection.

References

[1] Masahiro Aoki, Makoto Suzuki, Hirohisa Sano, Toshihiro Kawano, Tatemi Ido, Tsuyoshi Taniwatari, Kazuhisa Uomi, and Atsushi Takai. InGaAs/InGaAsP MQW electroabsorption modulator integrated with a DFB laser fabricated by band-gap energy control selective area MOCVD. *IEEE Journal of Quantum Electronics*, 29(6):2088–2096, 1993.

[2] Saddam Banyoudeh, Alireza Abdollahinia, Ori Eyal, Florian Schnabel, Vitalii Sichkovskyi, Gadi Eisenstein, and Johann Peter Reithmaier. Temperature-insensitive high-speed directly modulated 1.55 μm quantum dot lasers. *IEEE Photonics Technology Letters*, 28(21):2451–2454, 2016.

[3] HY Liu, DT Childs, TJ Badcock, KM Groom, IR Sellers, M Hopkinson, RA Hogg, DJ Robbins, DJ Mowbray, and MS Skolnick. High-performance three-layer 1.3-μm InAs-GaAs quantum-dot lasers with very low continuous-wave room-temperature threshold currents. *IEEE Photonics Technology Letters*, 17(6):1139–1141, 2005.

[4] Shuji Nakamura, Takashi Mukai, and Masayuki Senoh. Candela-class high-brightness InGaN/AlGaN double-heterostructure blue-light-emitting diodes. *Applied Physics Letters*, 64(13):1687–1689, 1994.

[5] M Hansen, P Fini, L Zhao, AC Abare, LA Coldren, JS Speck, and SP DenBaars. Improved characteristics of InGaN multiple-quantum-well laser diodes grown on laterally epitaxially overgrown GaN on sapphire. *Applied Physics Letters*, 76(5):529–531, 2000.

[6] Frank Dimroth, Matthias Grave, Paul Beutel, Ulrich Fiedeler, Christian Karcher, Thomas ND Tibbits, Eduard Oliva, Gerald Siefer, Michael Schachtner, Alexander Wekkeli, et al. Wafer bonded four-junction gainp/gaas//gainasp/gainas concentrator solar cells with 44.7% efficiency. *Progress in Photovoltaics: Research and Applications*, 22(3):277–282, 2014.

[7] CR Doerr, L Zhang, PJ Winzer, JH Sinsky, AL Adamiecki, NJ Sauer, and G Raybon. Compact high-speed inp dqpsk modulator. *IEEE Photonics Technology Letters*, 19(15):1184–1186, 2007.

[8] Niloy K Dutta and Qiang Wang. *Semiconductor optical amplifiers*. World scientific, 2013.

[9] Xiaowei Li, Ning Li, Xiaoguang Zheng, Stephane Demiguel, Joe C Campbell, David A Tulchinsky, and Keith J Williams. High-saturation-current inp-ingaas photodiode with partially depleted absorber. *IEEE Photonics Technology Letters*, 15(9):1276–1278, 2003.

[10] SY Wang and DM Bloom. 100 ghz bandwidth planar gaas schottky photodiode. *Electronics letters*, 19:554, 1983.

[11] Xudong Jiang, Mark A Itzler, Rafael Ben-Michael, and Krystyna Slomkowski. Ingaasp–inp avalanche photodiodes for single photon detection. *IEEE Journal of selected topics in quantum electronics*, 13(4):895–905, 2007.

[12] Cisco visual networking index: Forecast and trends, 2017–2022. Technical report, Cisco Systems Inc., 2019.

[13] Paul Jouguet, Sébastien Kunz-Jacques, Anthony Leverrier, Philippe Grangier, and Eleni Diamanti. Experimental demonstration of long-distance continuous-variable quantum key distribution. *Nature photonics*, 7(5):378–381, 2013.

[14] Sheng-Kai Liao, Wen-Qi Cai, Wei-Yue Liu, Liang Zhang, Yang Li, Ji-Gang Ren, Juan Yin, Qi Shen, Yuan Cao, Zheng-Ping Li, et al. Satellite-to-ground quantum key distribution. *Nature*, 549(7670):43–47, 2017.

[15] Mark Itzler. Automotive LiDAR based on Geiger-mode sensors (Conference Presentation). In Monte D. Turner and Gary W. Kamerman, editors, *Laser Radar Technology and Applications XXIII*, volume 10636, page 106360D. International Society for Optics and Photonics, SPIE, 2018.

[16] Peter R Ogilby. Singlet oxygen: there is indeed something new under the sun. *Chemical Society Reviews*, 39(8):3181–3209, 2010.

[17] Nathan R Gemmell, Aongus McCarthy, Baochang Liu, Michael G Tanner, Sander D Dorenbos, Valery Zwiller, Michael S Patterson, Gerald S Buller, Brian C Wilson, and Robert H Hadfield. Singlet oxygen luminescence detection with a fiber-coupled

superconducting nanowire single-photon detector. *Optics express*, 21(4):5005–5013, 2013.

[18] Adolf F Fercher, Wolfgang Drexler, Christoph K Hitzenberger, and Theo Lasser. Optical coherence tomography-principles and applications. *Reports on progress in physics*, 66(2):239, 2003.

[19] NIR (NEAR INFRARED:1.4 µm/1.7 µm) PHOTOMULTIPLIER TUBES R5509-43/R5509-73. https://www.hamamatsu.com/content/dam/hamamatsu-photonics/sites/documents/99_SALES_LIBRARY/etd/R5509-43_-73_TPMH1360E.pdf. Accessed: 2022-11-02.

[20] Robert H Hadfield. Single-photon detectors for optical quantum information applications. *Nature Photonics*, 3(12):696, 2009.

[21] Timing resolution optimized single photon counting module. https://www.excelitas.com/product/spcm-aqrh-tr#:~:text=Excelitas%20SPCM%2DAQRH%2DTR%20Family%20datasheet.

[22] ID Qube series: NIR. https://marketing.idquantique.com/acton/attachment/11868/f-80a02dd4-31f4-45d6-b096-bcd296ccc908/1/-/-/-/-/ID%20Qube_Brochure.pdf.

[23] F Marsili, Varun B Verma, Jeffrey A Stern, S Harrington, Adriana E Lita, Thomas Gerrits, Igor Vayshenker, Burm Baek, Matthew D Shaw, Richard P Mirin, et al. Detecting single infrared photons with 93% system efficiency. *Nature Photonics*, 7(3):210, 2013.

[24] HW Li, BE Kardynał, DJP Ellis, AJ Shields, I Farrer, and DA Ritchie. Quantum dot resonant tunneling diode single photon detector with aluminum oxide aperture defined tunneling area. *Applied Physics Letters*, 93(15):153503, 2008.

[25] Mary A Rowe, EJ Gansen, Marion Greene, RH Hadfield, TE Harvey, MY Su, Sae Woo Nam, RP Mirin, and D Rosenberg. Single-photon detection using a quantum dot optically gated field-effect transistor with high internal quantum efficiency. *Applied physics letters*, 89(25):253505, 2006.

[26] Fengnian Xia, Thomas Mueller, Yu-ming Lin, Alberto Valdes-Garcia, and Phaedon Avouris. Ultrafast graphene photodetector. *Nature nanotechnology*, 4(12):839, 2009.

[27] Gerasimos Konstantatos, Michela Badioli, Louis Gaudreau, Johann Osmond, Maria Bernechea, F Pelayo Garcia De Arquer, Fabio Gatti, and Frank HL Koppens. Hybrid graphene–quantum dot phototransistors with ultrahigh gain. *Nature nanotechnology*, 7(6):363, 2012.

[28] Evan D Walsh, Dmitri K Efetov, Gil-Ho Lee, Mikkel Heuck, Jesse Crossno, Thomas A Ohki, Philip Kim, Dirk Englund, and Kin Chung Fong. Graphene-based josephson-junction single-photon detector. *Physical Review Applied*, 8(2):024022, 2017.

[29] R Agarwal and CM Lieber. Semiconductor nanowires: optics and optoelectronics. *Applied physics A*, 85(3):209–215, 2006.

[30] Ruoxue Yan, Daniel Gargas, and Peidong Yang. Nanowire photonics. *Nature photonics*, 3(10):569–576, 2009.

[31] Li Na Quan, Joohoon Kang, Cun-Zheng Ning, and Peidong Yang. Nanowires for photonics. *Chemical reviews*, 119(15):9153–9169, 2019.

[32] Fernando Patolsky and Charles M Lieber. Nanowire nanosensors. *Materials today*, 8(4):20–28, 2005.

[33] Michael E Reimer, Gabriele Bulgarini, Nika Akopian, Moïra Hocevar, Maaike Bouwes Bavinck, Marcel A Verheijen, Erik PAM Bakkers, Leo P Kouwenhoven, and Val Zwiller. Bright single-photon sources in bottom-up tailored nanowires. *Nature communications*, 3(1):1–6, 2012.

[34] Carl J Barrelet, Jiming Bao, Marko Loncar, Hong-Gyu Park, Federico Capasso, and Charles M Lieber. Hybrid single-nanowire photonic crystal and microresonator structures. *Nano letters*, 6(1):11–15, 2006.

[35] Jesper Wallentin, Nicklas Anttu, Damir Asoli, Maria Huffman, Ingvar Åberg, Martin H Magnusson, Gerald Siefer, Peter Fuss-Kailuweit, Frank Dimroth, Bernd Witzigmann, et al. Inp nanowire array solar cells achieving 13.8% efficiency by exceeding the ray optics limit. *Science*, 339(6123):1057–1060, 2013.

[36] Sandra J Gibson, Brad van Kasteren, Burak Tekcan, Yingchao Cui, Dick van Dam, Jos EM Haverkort, Erik PAM Bakkers, and Michael E Reimer. Tapered inp nanowire arrays for efficient broadband high-speed single-photon detection. *nature nanotechnology*, 14(5):473–479, 2019.

[37] Richard G Hobbs, Nikolay Petkov, and Justin D Holmes. Semiconductor nanowire fabrication by bottom-up and top-down paradigms. *Chemistry of Materials*, 24(11):1975–1991, 2012.

[38] Jennifer Wong-Leung, Inseok Yang, Ziyuan Li, Siva Krishna Karuturi, Lan Fu, Hark Hoe Tan, and Chennupati Jagadish. Engineering iii–v semiconductor nanowires for device applications. *Advanced Materials*, 32(18):1904359, 2020.

[39] David Tsivion, Mark Schvartzman, Ronit Popovitz-Biro, Palle Von Huth, and Ernesto Joselevich. Guided growth of millimeter-long horizontal nanowires with controlled orientations. *Science*, 333(6045):1003–1007, 2011.

[40] Saman Jahani and Zubin Jacob. All-dielectric metamaterials. *Nature nanotechnology*, 11(1):23–36, 2016.

[41] Sebastian W Schmitt, George Sarau, and Silke Christiansen. Observation of strongly enhanced photoluminescence from inverted cone-shaped silicon nanostructures. *Scientific reports*, 5(1):1–12, 2015.

[42] Gil Shalev, Sebastian W Schmitt, Heidemarie Embrechts, Gerald Brönstrup, and Silke Christiansen. Enhanced photovoltaics inspired by the fovea centralis. *Scientific reports*, 5(1):1–7, 2015.

[43] Kihyun Kim, Sol Yoon, Myunghae Seo, Seungho Lee, Hyeonsu Cho, M Meyyappan, and Chang-Ki Baek. Whispering gallery modes enhance the near-infrared photoresponse of hourglass-shaped silicon nanowire photodiodes. *Nature Electronics*, 2(12):572–579, 2019.

[44] Jie Xiang, Wei Lu, Yongjie Hu, Yue Wu, Hao Yan, and Charles M Lieber. Ge/si nanowire heterostructures as high-performance field-effect transistors. *nature*, 441(7092):489–493, 2006.

[45] Katsuhiro Tomioka, Masatoshi Yoshimura, and Takashi Fukui. A iii–v nanowire channel on silicon for high-performance vertical transistors. *Nature*, 488(7410):189–192, 2012.

[46] RR LaPierre, M Robson, KM Azizur-Rahman, and P Kuyanov. A review of iii–v nanowire infrared photodetectors and sensors. *Journal of Physics D: Applied Physics*, 50(12):123001, 2017.

[47] Tevye Kuykendall, Philipp Ulrich, Shaul Aloni, and Peidong Yang. Complete composition tunability of ingan nanowires using a combinatorial approach. *Nature materials*, 6(12):951–956, 2007.

[48] Renjie Wang, Hieu PT Nguyen, Ashfiqua T Connie, J Lee, Ishiang Shih, and Zetian Mi. Color-tunable, phosphor-free ingan nanowire light-emitting diode arrays monolithically integrated on silicon. *Optics express*, 22(107):A1768–A1775, 2014.

[49] Johannes Svensson, Nicklas Anttu, Neimantas Vainorius, B Mattias Borg, and Lars-Erik Wernersson. Diameter-dependent photocurrent in inassb nanowire infrared photodetectors. *Nano letters*, 13(4):1380–1385, 2013.

[50] Martin T Hill and Malte C Gather. Advances in small lasers. *Nature Photonics*, 8(12):908–918, 2014.

[51] Gabriele Bulgarini, Michael E Reimer, Maaike Bouwes Bavinck, Klaus D Jons, Dan Dalacu, Philip J Poole, Erik PAM Bakkers, and Val Zwiller. Nanowire waveguides launching single photons in a gaussian mode for ideal fiber coupling. *Nano letters*, 14(7):4102–4106, 2014.

[52] Erik C Garnett, Mark L Brongersma, Yi Cui, and Michael D McGehee. Nanowire solar cells. *Annual review of materials research*, 41(1):269–295, 2011.

[53] Diego R Abujetas, Ramón Paniagua-Domínguez, and José A Sánchez-Gil. Unraveling the janus role of mie resonances and leaky/guided modes in semiconductor nanowire absorption for enhanced light harvesting. *Acs Photonics*, 2(7):921–929, 2015.

[54] Katherine T Fountaine, Christian G Kendall, and Harry A Atwater. Near-unity broadband absorption designs for semiconducting nanowire arrays via localized radial mode excitation. *Optics express*, 22(103):A930–A940, 2014.

[55] Katherine T Fountaine, Wen-Hui Cheng, Colton R Bukowsky, and Harry A Atwater. Near-unity unselective absorption in sparse inp nanowire arrays. *ACS Photonics*, 3(10):1826–1832, 2016.

[56] Gabriele Bulgarini, Michael E Reimer, Moïra Hocevar, Erik PAM Bakkers, Leo P Kouwenhoven, and Val Zwiller. Avalanche amplification of a single exciton in a semiconductor nanowire. *Nature Photonics*, 6(7):455–458, 2012.

[57] Wenjin Luo, Qianchun Weng, Mingsheng Long, Peng Wang, Fan Gong, Hehai Fang, Man Luo, Wenjuan Wang, Zhen Wang, Dingshan Zheng, et al. Room-temperature single-photon detector based on single nanowire. *Nano letters*, 18(9):5439–5445, 2018.

[58] Cheol-Joo Kim, Hyun-Seung Lee, Yong-Jun Cho, Kibum Kang, and Moon-Ho Jo. Diameter-dependent internal gain in ohmic ge nanowire photodetectors. *Nano letters*, 10(6):2043–2048, 2010.

[59] Hongsik Park, Jin Ho Kim, Roderic Beresford, and Jimmy Xu. Effects of electrical contacts on the photoconductive gain of nanowire photodetectors. *Applied Physics Letters*, 99(14):143110, 2011.

[60] Oliver Hayden, Ritesh Agarwal, and Charles M Lieber. Nanoscale avalanche photodiodes for highly sensitive and spatially resolved photon detection. *Nature materials*, 5(5):352–356, 2006.

[61] Alan C Farrell, Pradeep Senanayake, Chung-Hong Hung, Georges El-Howayek, Abhejit Rajagopal, Marc Currie, Majeed M Hayat, and Diana L Huffaker. Plasmonic field confinement for separate absorption-multiplication in ingaas nanopillar avalanche photodiodes. *Scientific reports*, 5(1):1–6, 2015.

[62] Alan C Farrell, Xiao Meng, Dingkun Ren, Hyunseok Kim, Pradeep Senanayake, Nick Y Hsieh, Zixuan Rong, Ting-Yuan Chang, Khalifa M Azizur-Rahman, and Diana L Huffaker. Ingaas–gaas nanowire avalanche photodiodes toward single-photon detection in free-running mode. *Nano letters*, 19(1):582–590, 2018.

[63] Rongqing Hui. *Introduction to fiber-optic communications*. Academic Press, 2019.

[64] Simon M Sze and Kwok K Ng. *Physics of semiconductor devices*. John wiley & sons, 2006.

[65] Verena Mackowiak, Jens Peupelmann, Yi Ma, and Anthony Gorges. NEP–noise equivalent power. *Thorlabs, Inc*, 56, 2015.

[66] Yux Xu, Ping Xiang, and Xiaopeng Xie. Comprehensive understanding of dark count mechanisms of single-photon avalanche diodes fabricated in deep sub-micron cmos technologies. *Solid-State Electronics*, 129:168–174, 2017.

[67] S Forrest. Performance of in x ga 1-x as y p 1-y photodiodes with dark current limited by diffusion, generation recombination, and tunneling. *IEEE Journal of quantum Electronics*, 17(2):217–226, 1981.

[68] SR Forrest, RF Leheny, RE Nahory, and MA Pollack. In0. 53ga0. 47as photodiodes with dark current limited by generation-recombination and tunneling. *Applied Physics Letters*, 37(3):322–325, 1980.

[69] SR Forrest, M DiDomenico Jr, RG Smith, and HJ Stocker. Evidence for tunneling in reverse-biased iii-v photodetector diodes. *Applied Physics Letters*, 36(7):580–582, 1980.

[70] Ock Kim, B Dutt, R McCoy, and J Zuber. A low dark-current, planar ingaas pin photodiode with a quaternary ingaasp cap layer. *IEEE journal of quantum electronics*, 21(2):138–143, 1985.

[71] Oliver Schultz, Ansgar Mette, Martin Hermle, and Stefan W Glunz. Thermal oxidation for crystalline silicon solar cells exceeding 19% efficiency applying industrially feasible process technology. *Progress in Photovoltaics: Research and Applications*, 16(4):317–324, 2008.

[72] A Ouacha, M Willander, B Hammarlund, and RA Logan. Effect of surface passivation with SiN on the electrical properties of InP/InGaAs heterojunction bipolar transistors. *Journal of applied physics*, 74(9):5602–5605, 1993.

[73] Joe C Campbell. Recent advances in telecommunications avalanche photodiodes. *Journal of Lightwave Technology*, 25(1):109–121, 2007.

[74] Brian F Aull, Andrew H Loomis, Douglas J Young, Richard M Heinrichs, Bradley J Felton, Peter J Daniels, and Deborah J Landers. Geiger-mode avalanche photodiodes for three-dimensional imaging. *Lincoln laboratory journal*, 13(2):335–349, 2002.

[75] Michael E Reimer, Maarten P Van Kouwen, Maria Barkelid, Moïra Hocevar, Maarten HM Van Weert, Rienk E Algra, Erik PAM Bakkers, Mikael T Björk, Heinz Schmid, Heike Riel, et al. Single photon emission and detection at the nanoscale utilizing semiconductor nanowires. *Journal of Nanophotonics*, 5(1):053502, 2011.

[76] RJ McIntyre. Multiplication noise in uniform avalanche diodes. *IEEE Transactions on Electron Devices*, (1):164–168, 1966.

[77] Robert J McIntyre. The distribution of gains in uniformly multiplying avalanche photodiodes: Theory. *IEEE Transactions on Electron Devices*, 19(6):703–713, 1972.

[78] Katsuhiko Nishida, Kenko Taguchi, and Yoshishige Matsumoto. Ingaasp heterostructure avalanche photodiodes with high avalanche gain. *Applied Physics Letters*, 35(3):251–253, 1979.

[79] Hiroaki Ando, Hiroshi Kanbe, Masanori Ito, and Takao Kaneda. Tunneling current in ingaas and optimum design for ingaas/inp avalanche photodiode. *Japanese Journal of Applied Physics*, 19(6):L277, 1980.

[80] F Capasso, AY Cho, and PW Foy. Low-dark-current low-voltage 1.3–1.6 μm avalanche photodiode with high-low electric field profile and separate absorption and multiplication regions by molecular beam epitaxy. *Electronics Letters*, 20(15):635–637, 1984.

[81] F Capasso, HM Cox, AL Hutchinson, NA Olsson, and SG Hummel. Pseudo-quaternary gainasp semiconductors: A new ga0. 47in0. 53as/inp graded gap superlattice and its applications to avalanche photodiodes. *Applied physics letters*, 45(11):1193–1195, 1984.

[82] Shuling Wang, Feng Ma, Xiaowei Li, Gauri Karve, Xiaoguang Zheng, and Joe C Campbell. Analysis of breakdown probabilities in avalanche photodiodes using a history-dependent analytical model. *Applied Physics Letters*, 82(12):1971–1973, 2003.

[83] Sadao Adachi. Optical dispersion relations for gap, gaas, gasb, inp, inas, insb, al x ga1- x as, and in1- x ga x as y p1- y. *Journal of Applied Physics*, 66(12):6030–6040, 1989.

[84] Ioffe, electrical properties of inp, ingaas, inalas, si, ge, gasb, gaas, etc. https://www.ioffe.ru/SVA/NSM/Semicond/.

[85] R Quay, C Moglestue, Vassil Palankovski, and Siegfried Selberherr. A temperature dependent model for the saturation velocity in semiconductor materials. *Materials Science in Semiconductor Processing*, 3(1-2):149–155, 2000.

[86] Silke L Diedenhofen, Olaf TA Janssen, Grzegorz Grzela, Erik PAM Bakkers, and Jaime Gomez Rivas. Strong geometrical dependence of the absorption of light in arrays of semiconductor nanowires. *ACS nano*, 5(3):2316–2323, 2011.

[87] Kwanyong Seo, Munib Wober, Paul Steinvurzel, Ethan Schonbrun, Yaping Dan, Tal Ellenbogen, and Kenneth B Crozier. Multicolored vertical silicon nanowires. *Nano letters*, 11(4):1851–1856, 2011.

[88] ZY Wang, RJ Zhang, SY Wang, M Lu, X Chen, YX Zheng, LY Chen, Z Ye, CZ Wang, and KM Ho. Broadband optical absorption by tunable mie resonances in silicon nanocone arrays. *Scientific reports*, 5(1):1–6, 2015.

[89] A Higuera-Rodriguez, B Romeira, S Birindelli, LE Black, E Smalbrugge, PJ Van Veldhoven, WMM Kessels, MK Smit, and A Fiore. Ultralow surface recombination velocity in passivated ingaas/inp nanopillars. *Nano letters*, 17(4):2627–2633, 2017.

[90] Xin Wang, Ning Duan, Hao Chen, and JC Campbell. Ingaas–inp photodiodes with high responsivity and high saturation power. *IEEE Photonics Technology Letters*, 19(16):1272–1274, 2007.

[91] Y Muramoto and T Ishibashi. Inp/ingaas pin photodiode structure maximising bandwidth and efficiency. *Electronics Letters*, 39(24):1, 2003.

[92] Hiroshi Ito, Satoshi Kodama, Yoshifumi Muramoto, Tomofumi Furuta, Tadao Nagatsuma, and Tadao Ishibashi. High-speed and high-output inp-ingaas unitraveling-carrier photodiodes. *IEEE Journal of selected topics in quantum electronics*, 10(4):709–727, 2004.

[93] Fabio Acerbi, Michele Anti, Alberto Tosi, and Franco Zappa. Design criteria for ingaas/inp single-photon avalanche diode. *IEEE Photonics Journal*, 5(2):6800209–6800209, 2013.

[94] Alessandro Spinelli and Andrea L Lacaita. Physics and numerical simulation of single photon avalanche diodes. *IEEE Transactions on Electron Devices*, 44(11):1931–1943, 1997.

[95] Andrew CE Chia and Ray R LaPierre. Analytical model of surface depletion in gaas nanowires. *Journal of Applied Physics*, 112(6):063705, 2012.

[96] Sara Pellegrini, Ryan E Warburton, Lionel JJ Tan, Jo Shien Ng, Andrey B Krysa, Kristian Groom, John PR David, Sergio Cova, Michael J Robertson, and Gerald S Buller. Design and performance of an ingaas-inp single-photon avalanche diode detector. *IEEE journal of quantum electronics*, 42(4):397–403, 2006.

[97] Mark A Itzler, Xudong Jiang, Mark Entwistle, Krystyna Slomkowski, Alberto Tosi, Fabio Acerbi, Franco Zappa, and Sergio Cova. Advances in ingaasp-based avalanche diode single photon detectors. *Journal of Modern Optics*, 58(3-4):174–200, 2011.

[98] Gauri Karve, Xiaoguang Zheng, Xiaofeng Zhang, Xiaowei Li, Ning Li, Shuling Wang, Feng Ma, A Holmes, Joe C Campbell, GS Kinsey, et al. Geiger mode operation of an in/sub 0.53/ga/sub 0.47/as-in/sub 0.52/al/sub 0.48/as avalanche photodiode. *IEEE journal of quantum electronics*, 39(10):1281–1286, 2003.

[99] Joseph P Donnelly, Erik K Duerr, K Alex McIntosh, Eric A Dauler, Douglas C Oakley, Steven H Groves, Christopher J Vineis, Leonard J Mahoney, Karen M Molvar, Pablo I Hopman, et al. Design considerations for 1.06-*mu* m ingaasp–inp geiger-mode avalanche photodiodes. *IEEE Journal of Quantum Electronics*, 42(8):797–809, 2006.

[100] Souye Cheong Liew Tat Mun, Chee Hing Tan, Simon J Dimler, Lionel JJ Tan, Jo Shien Ng, Yu Ling Goh, and John PR David. A theoretical comparison of the breakdown behavior of $in_{0.52}al_{0.48}as$ and inp near-infrared single-photon avalanche photodiodes. *IEEE journal of quantum electronics*, 45(5):566–571, 2009.

[101] Lionel Juen Jin Tan, Daniel Swee Guan Ong, Jo Shien Ng, Chee Hing Tan, Stephen K Jones, Yahong Qian, and John Paul Raj David. Temperature dependence of avalanche breakdown in inp and inalas. *IEEE Journal of Quantum Electronics*, 46(8):1153–1157, 2010.

[102] Saman Jahani and Zubin Jacob. All-dielectric metamaterials. *Nature nanotechnology*, 11(1):23–36, 2016.

[103] Seyedeh Mahsa Kamali, Ehsan Arbabi, Amir Arbabi, and Andrei Faraon. A review of dielectric optical metasurfaces for wavefront control. *Nanophotonics*, 7(6):1041–1068, 2018.

[104] Isabelle Staude, Andrey E Miroshnichenko, Manuel Decker, Nche T Fofang, Sheng Liu, Edward Gonzales, Jason Dominguez, Ting Shan Luk, Dragomir N Neshev, Igal Brener, et al. Tailoring directional scattering through magnetic and electric resonances in subwavelength silicon nanodisks. *ACS nano*, 7(9):7824–7832, 2013.

[105] Yu Yao, Zhefu Liao, Zhengqi Liu, Xiaoshan Liu, Jin Zhou, Guiqiang Liu, Zao Yi, and Junqiao Wang. Recent progresses on metamaterials for optical absorption and sensing: a review. *Journal of Physics D: Applied Physics*, 54(11):113002, 2021.

[106] Joonkyo Jung, Hyeonjin Park, Junhyung Park, Taeyong Chang, and Jonghwa Shin. Broadband metamaterials and metasurfaces: A review from the perspectives of materials and devices. *Nanophotonics*, 9(10):3165–3196, 2020.

[107] Wenshan Cai and Vladimir M Shalaev. *Optical metamaterials*, volume 10. Springer, 2010.

[108] Costas M Soukoulis and Martin Wegener. Past achievements and future challenges in the development of three-dimensional photonic metamaterials. *Nature photonics*, 5(9):523–530, 2011.

[109] Xianshun Ming, Xinyu Liu, Liqun Sun, and Willie J Padilla. Degenerate critical coupling in all-dielectric metasurface absorbers. *Optics express*, 25(20):24658–24669, 2017.

[110] Oleg Mitrofanov, Lucy L Hale, Polina P Vabishchevich, Ting Shan Luk, Sadhvikas J Addamane, John L Reno, and Igal Brener. Perfectly absorbing dielectric metasurfaces for photodetection. *Apl Photonics*, 5(10):101304, 2020.

[111] Nanfang Yu, Patrice Genevet, Mikhail A Kats, Francesco Aieta, Jean-Philippe Tetienne, Federico Capasso, and Zeno Gaburro. Light propagation with phase discontinuities: generalized laws of reflection and refraction. *science*, 334(6054):333–337, 2011.

[112] Francesco Monticone and Andrea Alu. Metamaterial, plasmonic and nanophotonic devices. *Reports on Progress in Physics*, 80(3):036401, 2017.

[113] Kan Yao and Yongmin Liu. Plasmonic metamaterials. *Nanotechnology Reviews*, 3(2):177–210, 2014.

[114] Asad A Tahir, Sebastian A Schulz, Israel De Leon, and Robert W Boyd. Design principles for wave plate metasurfaces using plasmonic l-shaped nanoantennas. *Journal of Optics*, 19(3):035001, 2017.

[115] M Saad Bin-Alam, Orad Reshef, Yaryna Mamchur, M Zahirul Alam, Graham Carlow, Jeremy Upham, Brian T Sullivan, Jean-Michel Ménard, Mikko J Huttunen, Robert W Boyd, et al. Ultra-high-q resonances in plasmonic metasurfaces. *Nature communications*, 12(1):1–8, 2021.

[116] Manuel Decker, Isabelle Staude, Matthias Falkner, Jason Dominguez, Dragomir N Neshev, Igal Brener, Thomas Pertsch, and Yuri S Kivshar. High-efficiency dielectric huygens' surfaces. *Advanced Optical Materials*, 3(6):813–820, 2015.

[117] J Van de Groep and A Polman. Designing dielectric resonators on substrates: Combining magnetic and electric resonances. *Optics express*, 21(22):26285–26302, 2013.

[118] Qian Zhao, Ji Zhou, Fuli Zhang, and Didier Lippens. Mie resonance-based dielectric metamaterials. *Materials today*, 12(12):60–69, 2009.

[119] Katie E Chong, Lei Wang, Isabelle Staude, Anthony R James, Jason Dominguez, Sheng Liu, Ganapathi S Subramania, Manuel Decker, Dragomir N Neshev, Igal Brener, et al. Efficient polarization-insensitive complex wavefront control using huygens' metasurfaces based on dielectric resonant meta-atoms. *Acs Photonics*, 3(4):514–519, 2016.

[120] Kebin Fan, Jonathan Y Suen, Xinyu Liu, and Willie J Padilla. All-dielectric metasurface absorbers for uncooled terahertz imaging. *Optica*, 4(6):601–604, 2017.

[121] Yingran He, Huixu Deng, Xiangyang Jiao, Sailing He, Jie Gao, and Xiaodong Yang. Infrared perfect absorber based on nanowire metamaterial cavities. *Optics letters*, 38(7):1179–1181, 2013.

[122] Michael A Cole, David A Powell, and Ilya V Shadrivov. Strong terahertz absorption in all-dielectric huygens' metasurfaces. *Nanotechnology*, 27(42):424003, 2016.

[123] Xinyu Liu, Kebin Fan, Ilya V Shadrivov, and Willie J Padilla. Experimental realization of a terahertz all-dielectric metasurface absorber. *Optics express*, 25(1):191–201, 2017.

[124] Linyou Cao, Justin S White, Joon-Shik Park, Jon A Schuller, Bruce M Clemens, and Mark L Brongersma. Engineering light absorption in semiconductor nanowire devices. *Nature materials*, 8(8):643–647, 2009.

[125] Chi-Yin Yang, Jhen-Hong Yang, Zih-Ying Yang, Zhong-Xing Zhou, Mao-Guo Sun, Viktoriia E Babicheva, and Kuo-Ping Chen. Nonradiating silicon nanoantenna metasurfaces as narrowband absorbers. *Acs Photonics*, 5(7):2596–2601, 2018.

[126] Baomin Wang and Paul W Leu. Tunable and selective resonant absorption in vertical nanowires. *Optics letters*, 37(18):3756–3758, 2012.

[127] Allan W Snyder and John Love. *Optical waveguide theory*. Springer Science & Business Media, 2012.

[128] Baomin Wang and Paul W Leu. Enhanced absorption in silicon nanocone arrays for photovoltaics. *Nanotechnology*, 23(19):194003, 2012.

[129] Navneet Dhindsa, Andrew Chia, Jonathan Boulanger, Iman Khodadad, Ray LaPierre, and Simarjeet S Saini. Highly ordered vertical gaas nanowire arrays with dry etching and their optical properties. *Nanotechnology*, 25(30):305303, 2014.

[130] Kirt R Williams, Kishan Gupta, and Matthew Wasilik. Etch rates for micromachining processing-part ii. *Journal of microelectromechanical systems*, 12(6):761–778, 2003.

[131] SJ Pearton, F Ren, TR Fullowan, A Katz, WS Hobson, UK Chakrabarti, and CR Abernathy. Plasma etching of iii–v semiconductor thin films. *Materials chemistry and physics*, 32(3):215–234, 1992.

[132] Uthayasankaran Peralagu, Xu Li, Olesya Ignatova, Yen-Chun Fu, David Alan John Millar, Matthew J Steer, Ian M Povey, Khalid Hossain, Manish Jain, Terry G Golding, et al. Towards a vertical and damage free post-etch ingaas fin profile: Dry etch processing, sidewall damage assessment and mitigation options. *ECS Transactions*, 69(5):15, 2015.

[133] Xin Zhao and Jesús A del Alamo. Nanometer-scale vertical-sidewall reactive ion etching of InGaAs for 3-D III-V MOSFETs. *IEEE Electron Device Letters*, 35(5):521–523, 2014.

[134] Jie Lin, Andreas Leven, NG Weimann, Y Yang, RF Kopf, R Reyes, YK Chen, and Fow-sen Choa. Smooth and vertical-sidewall InP etching using Cl_2/N_2 inductively coupled plasma. *Journal of Vacuum Science & Technology B: Microelectronics and Nanometer Structures Processing, Measurement, and Phenomena*, 22(2):510–512, 2004.

[135] Jae Su Yu and Yong Tak Lee. Parametric reactive ion etching of inp using cl2 and ch4 gases: effects of h2 and ar addition. *Semiconductor science and technology*, 17(3):230, 2002.

[136] S_C McNevin. Chemical etching of gaas and inp by chlorine: The thermodynamically predicted dependence on cl2 pressure and temperature. *Journal of Vacuum Science & Technology B: Microelectronics Processing and Phenomena*, 4(5):1216–1226, 1986.

[137] C Constantine, C Barratt, SJ Pearton, F Ren, and JR Lothian. Smooth, low-bias plasma etching of inp in microwave cl2/ch4/h2 mixtures. *Applied physics letters*, 61(24):2899–2901, 1992.

[138] Y Cui, D Van Dam, SA Mann, NJJ Van Hoof, PJ Van Veldhoven, Erik C Garnett, EPAM Bakkers, and JEM Haverkort. Boosting solar cell photovoltage via nanophotonic engineering. *Nano letters*, 16(10):6467–6471, 2016.

[139] Gregory C DeSalvo, Christopher A Bozada, John L Ebel, David C Look, John P Barrette, Charles LA Cerny, Ross W Dettmer, James K Gillespie, Charles K Havasy, Thomas J Jenkins, et al. Wet chemical digital etching of gaas at room temperature. *Journal of The Electrochemical Society*, 143(11):3652, 1996.

[140] RJ Hussey, GI Sproule, JP McCaffrey, and MJ Graham. Characterization of oxides formed on inp, ingaas, inalas, and ingaas/inalas heterostructures at 300–500 c. *Oxidation of metals*, 57(5):427–447, 2002.

[141] Cyclotene 3000 series. https://kayakuam.com/wp-content/uploads/2019/09/cyclotene_3000_dry_etch.pdf.

[142] Alan C Farrell, Pradeep Senanayake, Xiao Meng, Nick Y Hsieh, and Diana L Huffaker. Diode characteristics approaching bulk limits in gaas nanowire array photodetectors. *Nano letters*, 17(4):2420–2425, 2017.

[143] Dick Van Dam, Niels JJ Van Hoof, Yingchao Cui, Peter J Van Veldhoven, Erik PAM Bakkers, Jaime Gomez Rivas, and Jos EM Haverkort. High-efficiency nanowire solar cells with omnidirectionally enhanced absorption due to self-aligned indium–tin–oxide mie scatterers. *ACS nano*, 10(12):11414–11419, 2016.

[144] A new dawn for NIR spectroscopy: Technical notes. https://www.princetoninstruments.com/learn/fluorescent-decay/a-new-dawn-for-nir-spectroscopy.

[145] Yingjie Ma, Yonggang Zhang, Yi Gu, Xingyou Chen, Yanhui Shi, Wanyan Ji, Suping Xi, Ben Du, Xiaoliang Li, Hengjing Tang, et al. Impact of etching on the surface leakage generation in mesa-type ingaas/inalas avalanche photodetectors. *Optics Express*, 24(7):7823–7834, 2016.

[146] AG Chynoweth. Charge multiplication phenomena. In *Semiconductors and Semimetals*, volume 4, pages 263–325. Elsevier, 1968.

[147] Vishal Jain, Magnus Heurlin, Enrique Barrigon, Lorenzo Bosco, Ali Nowzari, Shishir Shroff, Virginia Boix, Mohammad Karimi, Reza J Jam, Alexander Berg, et al. InP/InAsP nanowire-based spatially separate absorption and multiplication avalanche photodetectors. *ACS Photonics*, 4(11):2693–2698, 2017.

[148] Jheng-Jie Liu, Wen-Jeng Ho, June-Yan Chen, Jian-Nan Lin, Chi-Jen Teng, Chia-Chun Yu, Yen-Chu Li, and Ming-Jui Chang. The fabrication and characterization of InAlAs/InGaAs APDs based on a mesa-structure with polyimide passivation. *Sensors*, 19(15):3399, 2019.

[149] Burak Tekcan, Brad van Kasteren, Sasan V Grayli, Daozhi Shen, Man Chun Tam, Dayan Ban, Zbigniew Wasilewski, Adam W Tsen, and Michael E Reimer. Semiconductor nanowire metamaterial for broadband near-unity absorption. *arXiv preprint arXiv:2202.13515*, 2022.

[150] Mark A Itzler, R Ben-Michael, C-F Hsu, Krystyna Slomkowski, Alberto Tosi, Sergio Cova, Franco Zappa, and Radu Ispasoiu. Single photon avalanche diodes (spads) for

1.5 μ m photon counting applications. *Journal of modern optics*, 54(2-3):283–304, 2007.

[151] Sergio Cova, M Ghioni, A Lacaita, Carlo Samori, and Franco Zappa. Avalanche photodiodes and quenching circuits for single-photon detection. *Applied optics*, 35(12):1956–1976, 1996.

[152] Hele Savin, Päivikki Repo, Guillaume Von Gastrow, Pablo Ortega, Eric Calle, Moises Garín, and Ramon Alcubilla. Black silicon solar cells with interdigitated back-contacts achieve 22.1% efficiency. *Nature nanotechnology*, 10(7):624–628, 2015.

APPENDICES

Appendix A

Matlab Code

A.1 Band-to-band current calculation of InGaAs and InAlAs

All figure properties can also be manipulated from the command line. Here's an example:

```
% Band to band tunneling calculation
clear all;
me = 9.1e-31;       % Mass of electron [kg]
q = 1.6e-19;        % Elementary charge [Coulombs]
h = 6.582e-16;      % Reduced Planck constant [eV.s]
m_star = 0.03*me;   % Effective reduced mass [kg],
                    % assumed 0.03 for InGaAs and 0.07 for InAlAs
Eg = 0.73;          % Band gap of InGaAs [eV]
theta = 0.3;

BB_A = (2*m_star/(Eg*q))^0.5*(q^2/((2*pi)^2*(h*q)^2))/100;  % in [1/(cm*V^2*s)]
BB_B = (theta*(me*(Eg*q)^3)^0.5)/(q*(h*q))/100;        % in [V/cm]

%% Alternative calculation based on Silvaco manual
h = 6.62e-34;
bb_a = q^2*sqrt(2*m_star)/(h^2*sqrt(Eg*q))/100;
bb_b = pi^2*(Eg*q)^1.5*sqrt(m_star/2)/(q*h)/100;
```

```
BB_A_InGaAs = BB_A;
BB_B_InGaAs = BB_B;

E=0:1000:2.71e5;
G_btb = BB_A.*E.^2.*exp(-BB_B./E);
I_tunnel = G_btb.*q.*1e-4*(50e-4)^2;
figure;plot(E,I_tunnel);hold on;

% clear all;
me = 9.1e-31;       % Mass of electron [kg]
q = 1.6e-19;        % Elementary charge [Coulombs]
h = 6.582e-16;      % Reduced Planck constant [eV.s]
m_star = 0.07*me;   % Effective reduced mass [kg],
                    % assumed 0.03 for InGaAs and 0.07 for InAlAs
Eg = 1.45;          % Band gap of InGaAs [eV]

BB_A = (2*m_star/(Eg*q))^0.5*(q^2/((2*pi)^2*(h*q)^2))/100;  % in [1/(cm*V^2*s)]
BB_B = (pi*(2*m_star*(Eg*q)^3)^0.5)/(4*q*(h*q))/100;        % in [V/cm]

BB_A_InAlAs = BB_A;
BB_B_InAlAs = BB_B;

%% Alternative calculation based on Silvaco manual
h = 6.62e-34;
bb_a_2 = q^2*sqrt(2*m_star)/(h^2*sqrt(Eg*q))/100;
bb_b_2 = pi^2*(Eg*q)^1.5*sqrt(m_star/2)/(q*h)/100;

E=0:1000:6.9e5;
G_btb = BB_A.*E.^2.*exp(-BB_B./E);
I_tunnel = G_btb.*q.*1e-4*(50e-4)^2;
plot(E,I_tunnel);
legend('InGaAs','InAlAs');
xlabel('Electric Field (V/cm)');
ylabel('Current (A)');
```

Appendix B

Nanowire metamaterials supporting information

B.1 Improved Model Accuracy of the Metamaterial with Tapered Nanowire Metaatoms

In order to verify the agreement between the experimentally measured absorption spectra and the calculated results from simulation, the optical absorption characteristics were obtained by measuring the absorption spectra of InGaAs nanowires fabricated on InGaAs/InP substrate. The incoming light passes through a Schwarzschild reflective objective with a numerical aperture of 0.5, introducing incident angles from -30° to 30° of the focused beam. This was accounted for in the numerical calculations by sweeping the source angle of incidence over a matching range and averaging the absorptance. Next, we fabricate the nanowire metamaterial absorber with dimensions as close as possible to the optimized structure using an InGaAs film (2250 nm thickness) grown by molecular beam epitaxy on an (100) InP substrate. We utilized a multistep nanofabrication process to realize a 100 μm x 100 μm metamaterial comprised of a tapered InGaAs nanowire array. See Supplementary Note 6 for details on the nanowire fabrication process.

B.2 Effect of Tapered Nanowire Height on the Metamaterial Absorption Efficiency

We investigated the effect of the metaatom nanowire height on the absorption efficiency by systematically reducing the nanowire height from 1.6 μm to 200 nm (Figure B.1). The lattice structure was constructed from the tapered nanowires infinitely repeating with periodicity of 900 nm without a substrate. The top and bottom diameters match the fabricated metamaterial absorbers, i.e., the top diameter is 350 nm and bottom diameter is 880 nm. It was observed that the high-performance broadband absorption efficiency over the target spectrum (0.9 μm to 1.7 μm) remains relatively unchanged for nanowire heights of 1.2 μm to 1.6 μm. As the height of the nanowires are reduced below 1.2 μm, the absorption efficiency performance is shown to noticeably decrease. Next, the effect of the nanowire height was studied after including a substrate in the numerical calculation to reflect a more realistic comparison between simulations and the fabricated nanowire arrays. The substrate consisted of an InP wafer and a thin film of InGaAs to match the parameters of the fabricated metamaterials. The absorption response of the updated metamaterial was then found as a function of nanowire height over the high broadband performance height range found for the suspended nanowires (1 μm to 1.6 μm). The thickness of the total InGaAs (including the nanowire and substrate thickness) film remained constant, i.e., the substrate thickness was increased to maintain a total thickness of 2250 nm of the InGaAs film when the height of the nanowire was decreased. As seen in Figure B.1b, the absorption efficiency showed little dependence on the changing nanowire height when the substrate is included, highlighting the impact of the substrate on the overall metamaterial absorption efficiency characteristics.

B.3 Growth and Characterization of the Indium Gallium Arsenide Film

The InGaAs film that was used to fabricate the metamaterial array was grown by a Veecco GEN10 molecular beam epitaxy system, located at the Quantum Nano Centre Molecular Beam Epitaxy Lab (University of Waterloo), on a (100) InP single crystal wafer. Ellipsometry was used to extract the complex refractive index of the InGaAs film and is plotted in Figure B.2. This optical data was imported into the Lumerical FDTD software and it was further used in all of the InGaAs nanowire metamaterial modeling.

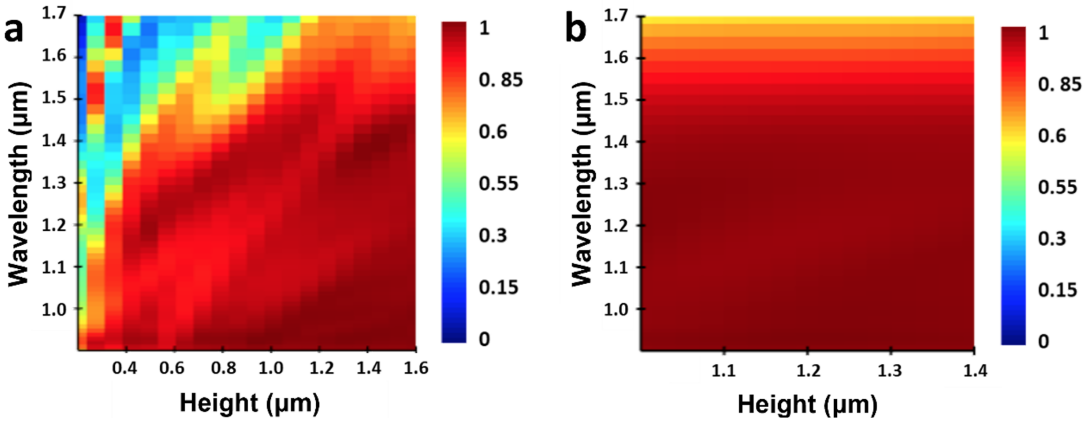


Figure B.1: The effect of height on the absorption response of the InGaAs tapered nanowire metamaterial. The height absorption response is shown without a substrate in a) and with a substrate in b). Without the substrate, the impact of the changing metaatom height becomes apparent in the absorption efficiency of the metamaterial. Once the nanowire height is reduced below 1 μm, the high broadband absorption performance of the metamaterial begins to diminish. b) With the substrate, the broadband absorption efficiency of the metamaterial does not undergo a noticeable change with the varying nanowire height and when compared to a).

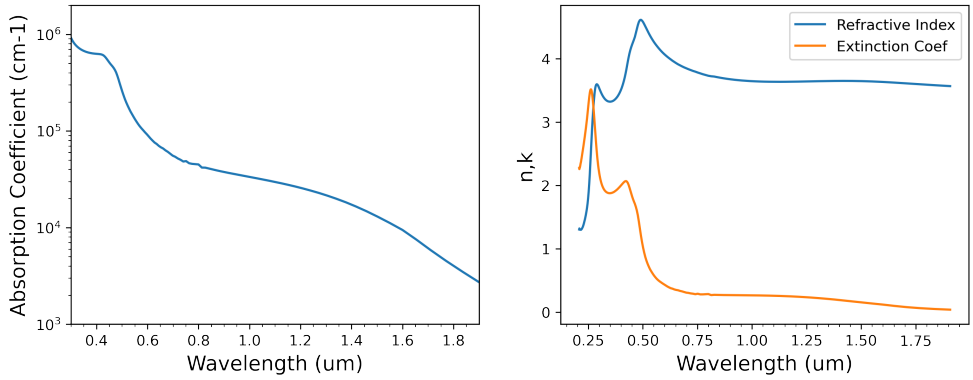


Figure B.2: Complex refractive index and calculated absorption coefficient of MBE grown InGaAs. The spectroscopic ellipsometry measured complex refractive index of the epitaxially grown InGaAs film on a (100) InP single crystal wafer.

B.4 FTIR Measurement

The transmission and reflection spectra of the samples were measured using a Bruker IFS 66v/S Fourier-transform infrared (FTIR) spectrometer. A tungsten halogen source (OSRAM, 275W) was focused onto the sample under test by a 36× reflective objective (Ealing, NA = 0.5), following the FTIR beam splitter. For the transmission spectrum measurement, the transmitted light from sample and background was collected by another reflective objective (behind the sample) and directed to a liquid-nitrogen-cooled mercury cadmium telluride (MCT) detector (EG&G JUDSON J16D-M204-R05M-60). For the reflection measurement, a D-shaped mirror (Thorlabs PFD10-03-P01) was placed before the Schwarzschild reflective objective. The reflected light from sample was collected into the MCT detector by the D shape mirror. The D-shaped mirror used in this reflection measurement was a silver mirror (Thorlabs PF10-03-P01) with a reflectivity > 97%, this was used as the reference spectrum for the wavelength range of interest.

B.5 FTIR Data Processing

The measured reflection/transmission spectra were used to extract the absorption characteristics of the fabricated metamaterial samples. Reference data was collected for the source, absent of any absorber samples. This reference data was used to normalize the FTIR data collected from the sample measurements to the source. The sample absorption efficiency was then calculated from the normalized FTIR sample data, knowing A = 1 – T – R. Where A is the absorptance, T is the transmittance, and R is the reflectance. The resulting absorption data was then adjusted to account for the artificial absorption observed below the InGaAs bandgap energy, which resulted from the thin film interference in the transmission data that was introduced from the reflective objective. To account for this interference, the data was scaled to be considerate of the InGaAs bandgap where the lowest absorption is expected to be near zero. The background correction method used scaled the absorption data according to the formula (xi – xmin)/(1-xmin). The results from scaling each data point by this formula bounded the lower absorptance to near zero and underestimates the absorption efficiency of the nanowire metamaterial. Despite the conservative approach, the resulting metamaterial absorption data presented an average of 93% absorption efficiency between 900 nm-1500 nm range. The absorption measurement was plotted before and after the correction in Figure B.3. Here, the arrow indicates the region below bandgap where the scaled absorptance was lower bounded to near zero.

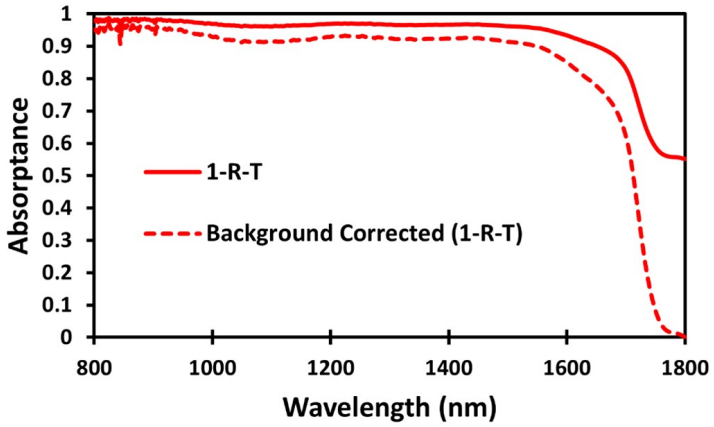


Figure B.3: The calculated absorption efficiency of the fabricated nanowire metamaterial before and after the thin film interference background correction. This plot was obtained from subtracting the source normalized sample reflection and transmission data from unity. The arrow indicates the region below the InGaAs bandgap which was expected to exhibit a near zero absorption.

B.6 Optical Properties of the Tapered Nanowire Metamaterials with Varying Metaatom Unit Cells

To study the success of the optimization process and simulation model, additional nanowire metamaterial designs were numerically and experimentally analyzed. This process also acted to further improve understanding for how the physical properties of the metaatoms can impact the metamaterial broadband absorption behaviour. Specifically, a series of tapered nanowire metamaterials with varying pitch and radii were investigated. The scanning electron micrographs of the various nanowire metamaterials, corresponding to NW1-NW4, are included in Figure B.4. The broadband absorption responses of these various metamaterials were also experimentally assessed with FTIR, according to the "FTIR Measurement" and "FTIR Data Processing" sections. Figure B.5 shows the corresponding modeled and experimentally obtained broadband absorption response of the fabricated nanowire metamaterials NW1 – NW4. We note that the metaatom nanowire height for NW1-NW4 was approximately 1.3 μm.

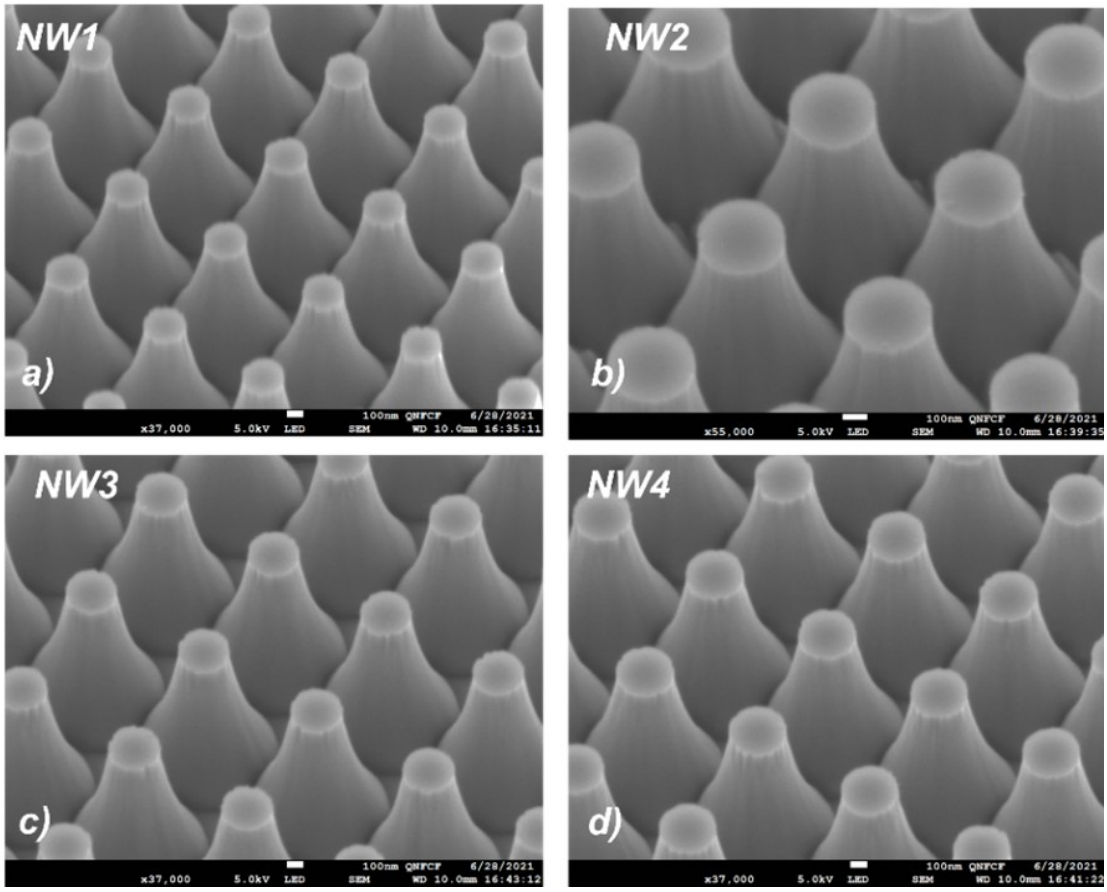


Figure B.4: The tilted angle scanning electron micrographs of the fabricated metamaterials NW1-NW4. a) Sample NW1 was measured to have: d_{top} = 250 nm, d_{bottom} = 682 nm, periodicity = 700 nm. b) Sample NW2: d_{top} = 350 nm, d_{bottom} = 682 nm, periodicity = 700nm. c) Sample NW3: d_{top} = 300nm, d_{bottom} = 782nm, periodicity = 800nm. d) Sample NW4: d_{top} = 350 nm, d_{bottom} = 782 nm, periodicity = 800 nm. The height of the nanowires in all of the fabricated metamaterials was measured to be approximately 1.3 μm.

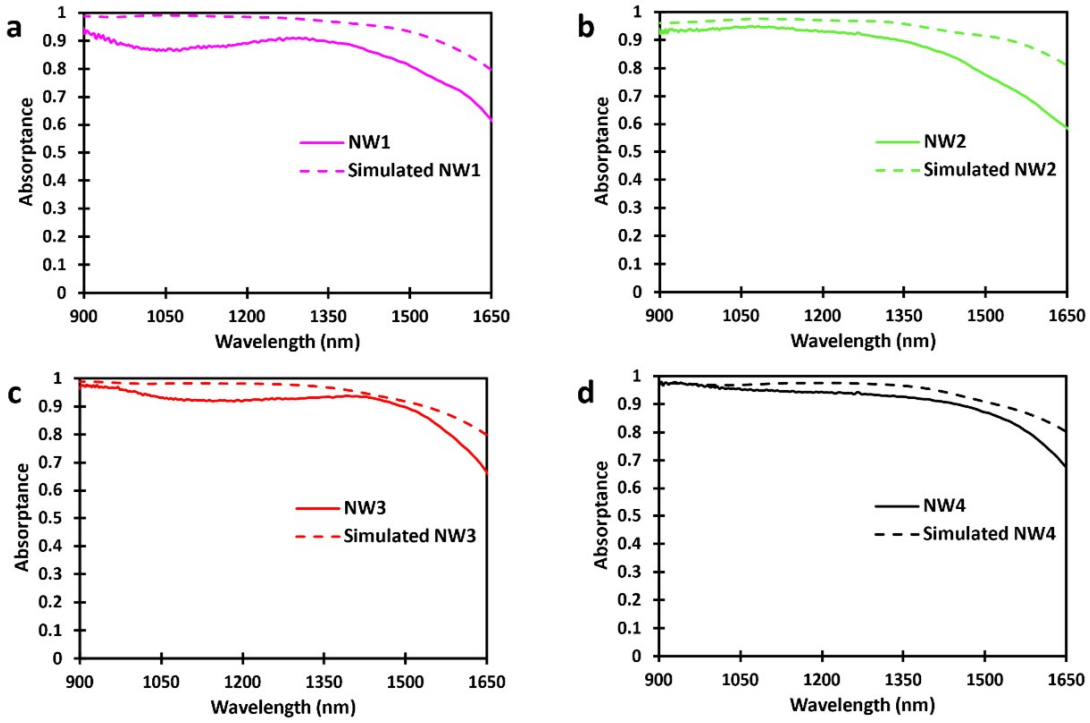


Figure B.5: The numerical and FTIR experimental absorption efficiency of four different broadband nanowire metamaterial absorbers, NW1-NW4. a)-d) show the measured and modeled absorption efficiencies of the respective metamaterials outlined in Figure B.4.